Quantifying and Enhancing Puncture Resistance in Railroad Tank Cars Carrying Hazardous Materials

Phase II: Development and Validation of a Puncture Resistance Evaluation Methodology

Prepared for

Transportation Issues Team
The Chlorine Institute
Arlington, VA

Prepared by

Ted L. Anderson, Ph.D., P.E.
Brian Rose, Ph.D., P.E.
Quest Reliability, LLC

Peter C. McKeighan. Ph.D.
Southwest Research Institute

Steven W. Kirkpatrick, Ph.D.
Applied Research Associates, Inc.

December 20, 2007

2465 Central Ave., Suite 110
Boulder, CO 80301
(303) 415-1475
(303) 415-1847 (fax)
www.questreliability.com

EXECUTIVE SUMMARY

This report summarizes Phase II of a project to study puncture resistance in tank cars that carry hazardous cargo. This project consists of both material testing and extensive finite element simulation. The former includes a newly-developed impact test on unnotched samples, which appears to be a suitable compromise between conventional Charpy tests, which do not give a direct measure of puncture resistance, and full-scale collision experiments, which are very expensive.

Finite element simulations were performed on both laboratory tests and full-scale tank cars. The former were used to calibrate the material fracture model used in this study. A large number of tank car impact simulations were performed. Several key variables were considered, including internal pressure, the size of the striker, friction, lading mass, and material toughness. A series of collision simulations on cars made from traditional tank car steel were used in conjunction with the accident database maintained by the RSI-AAR Railroad Tank Car Safety Research and Test Project to benchmark the statistical distribution of the intensity of collision/puncture events. This calibration exercise enabled the authors to evaluate the effect of material properties and design features on the probability of lading loss in an accident. The finite element puncture simulation procedure developed in this study was benchmarked against a recent full-scale test conducted at the Transportation Technology Center, Inc. (TTCI). The simulation predicted the puncture energy in the full-scale test to within a few percent.

A series of tank car collision simulations compared the behavior of traditional tank car steel with modern, high-toughness alternatives. These analyses indicated that roughly a 2-fold increase in puncture energy is possible with improved steels. This translates to a 60-fold decrease in lading loss probability for shell impacts and a 6-fold decrease in lading loss probability for head impacts.

The material model for simulating ductile fracture that was used in this study was compared qualitatively with an alternative model that has been adopted by the Volpe National Transportation Systems Center. Further work is necessary to compare these models quantitatively to determine if one model is more suitable for tank car collision simulation.

CONTENTS

1 BACKGROUND

When a derailment or other rail accident occurs, the resulting collision forces can lead to a loss of lading from tank cars. While such an event is always undesirable, it is particularly damaging when the cars contain a hazardous material. There is a strong desire in the rail industry to develop a new generation of tank cars that are more resistant to puncture in the event of an accident.

A Phase I study of factors affecting puncture resistance was recently completed [1]. Key conclusions and recommendations from this study include the following:

- While low-temperature toughness properties are desirable in tank car steels, it is primarily the upper shelf toughness that governs puncture resistance.
- In previous accidents, the probability of lading loss through head or shell punctures was influenced by section thickness, as well as the presence or absence of head shields and/or jackets.
- Based on trends in the accident database, puncture resistance can be improved by various design modifications, including increasing section thickness and incorporating head shields. However, incorporation of more puncture resistant steels may also be an effective means to reduce the likelihood of lading loss in future accidents.
- Although it is likely that improved steels will enhance puncture resistance, the potential benefit of such materials has not been quantified.
- Computer simulation, benchmarked by suitable experiments, is an effective means to assess the effect of tank car design and material properties on puncture resistance.

This report describes the results of Phase II of this project, which consisted of both materials testing and finite element computer simulation. Material testing included tensile testing at various strain rates, which was necessary to feed into the finite element models. In addition a new material test, which entails impact loading of unnotched specimens, was developed in this project to characterize puncture resistance of steels. A literature search was also performed, the results of which are summarized in Appendix A.

Finite element simulations were performed on both laboratory specimens and full-scale tank cars. The former was used to calibrate the material fracture model that was applied to the latter. A large number of simulations of tank car impact/puncture events have been performed. The effect of a number of variables were studied, including tank car dimensions, internal pressure, striker size, friction, lading mass, and material properties. Simulation results were calibrated to the accident database maintained by the RSI-AAR Railroad Tank Car Safety Research and Test Project. The simulation procedure was also benchmarked against a recent full-scale experiment performed at Transportation Technology Center, Inc. (TTCI) in Pueblo, Colorado.

One of the main purposes of the extensive computer simulations and material testing was to quantify the effect of design parameters and material toughness on puncture resistance in tank cars. The procedures developed herein can be used to assess a proposed tank car design against a suitable performance standard.

2 MATERIAL TESTING

Two types of mechanical tests were performed in this study:

1. Tensile tests at various strain rates.
2. Impact tests on unnotched specimens.

The former was used to define the stress-strain behavior for the finite element simulations. The latter was used to benchmark and validate the ductile fracture material model.

2.1 Tensile Testing

Tensile testing was performed on several steels over a range of strain rates. True stress-strain curves were fitted to these data and were input into the various finite element simulations.

Two samples of traditional tank car steel, TC 128B, were tested. As indicated in Table 2.1 below, these samples are normalized shell plates from two tank cars built in 1994.

Tensile testing was performed on three high strength-low alloy (HSLA) steels. These materials are listed in Table 2.2

TABLE 2.1
Samples of TC 128B steel used for tensile testing.

Sample ID	Car ID	Year Built	Sample Location	Heat Treatment	Specimen Orientation
A	PROX 31153	1994	Shell	Normalized	Transverse
B	PROX 31218	1994	Shell	Normalized	Transverse

TABLE 2.2
High strength-low alloy (HSLA) steels tested in the present study.

Material	Reported Thickness, in	Notes
A 710	0.75	Fabricated by Mittal Steel ISG Plate Inc, Melt U4749, Used for a bridge in Lake Villas, IL (Fine/Vanadium-Nb)
HPS 70	0.75	Fabricated by IPSCO
HPS 100	1.125	Fabricated by Mittal Steel ISG Plate Inc (supplied by M. Manohar)

2.1.1 TC 128B Steel

Figure 2.1 shows typical true stress-strain curves for TC 128B steel at various strain rates. The stress axis is indexed by the 0.2% offset yield strength. The strain hardening behavior is insensitive to strain rate but the Luder's strain (i.e., the extent of the yield plateau region) does appear to be rate dependent.

Figure 2.2 is a plot of yield strength versus strain rate. The data for the two plates, A and B, are indistinguishable from one another, so a single power-law fit for the combined data set was appropriate in this case. Figure 2.3 shows the correlation between the Luder's strain and the strain rate.

The power-law expressions on the plots in Figs. 2.2 and 2.3, combined with a fit of the hardening portion of a typical stress-strain curve (Fig. 2.1), were used to develop the plastic constitutive relationship for TC 128B steel. The result of this exercise is plotted in Fig. 2.4. Note that the upper yield point was neglected in the fitting process. The curves in Fig. 2.4 were input into the various finite element simulations. The stress-strain behavior illustrated in Fig. 2.4 was assumed to apply to all heats of TC 128B steel. This is a reasonable assumption, since tensile requirements for TC 128B steel have not changed over the years. Improvements in alloy cleanliness (i.e., reductions in sulfur content) that have occurred over time will not have an appreciable effect on tensile properties. Therefore, the stress-strain curves in Fig. 2.4 should be reasonably representative of the existing tank car fleet.

2.1.2 HSLA Steels

Figure 2.5 is a plot of the lower yield stress (i.e., the stress on the yield plateau) versus strain rate for A 710 steel. As was the case for TC 128B steel, a power-law expression adequately describes the strain rate dependence of yield strength. The stress-strain data, indexed by lower yield stress, is plotted in Fig. 2.6. Neither the Luder's strain nor the hardening behavior appears to be a strong function of strain rate. The modest variability in stress-strain curves in Fig. 2.6 is not a systematic function of strain rate. Figure 2.7 shows the idealized fit of the stress-strain behavior for A 710 steel.

Figure 2.8 is a plot of yield strength versus strain rate for HPS 70 steel. This material exhibits different strain rate dependence that the other steels considered in this study. It appears to fit the Cowper-Symonds model, which is given by

$$\sigma_{YS} = \sigma_o \left[1 + \left(\frac{\dot{\varepsilon}}{C} \right)^{1/p} \right] \tag{2.1}$$

where σ_o, C and p are material constants. For the HPS 70 plate, the following constants were inferred:

σ_o = 84 ksi
C = 122.2987 s-1

$p = 1.08478$

Note that the Cowper-Symonds fit predicts a rapid increase in yield strength at strain rates above 1 s^{-1}. Experimental data are not available at strain rates above approximately 8 s^{-1}, so this extrapolated trend may or may not be real. Some of the subsequent simulations with HPS 70 steel assumed that the stress-strain curve remains constant above 10 s^{-1}. That is, Eq. (2.1) was truncated at a $\dot{\varepsilon} = 10\ s^{-1}$. Other simulations with this material extrapolated the stress-strain behavior to a strain rate of 100 s^{-1}.

Figure 2.9 shows measured stress-strain behavior for HPS 70 steel. The idealized fitted curves are plotted in Fig. 2.10.

Figure 2.11 is a plot of 0.2% yield strength and flow stress at 1% plastic strain versus strain rate for HPS 100 steel. There is no discernable, systematic relationship between strength and strain rate for this material. The authors are not aware of a credible metallurgical explanation for the apparent lack of a strain rate dependence of HPS 100 steel.

Figure 2.12 is a plot of measured stress strain curves for HPS 100 steel. In this case, the curves were indexed by the flow stress at 1% plastic strain. This family of curves exhibited considerable variability when indexed by the 0.2% yield strength, but collapse onto a common trend when indexed by the 1% flow stress. Note that this material does not have a yield plateau. Indexing to the 0.2% yield strength is not effective reducing the curves to a common trend in this case because the stress versus plastic strain curves are very steep at low strains.

Since the both the yield strength and hardening behavior of HPS 100 steel are insensitive to strain rate, a single stress-strain curve was used for all strain rates. The fitted stress strain curve for HPS 100 is shown in Fig. 2.13.

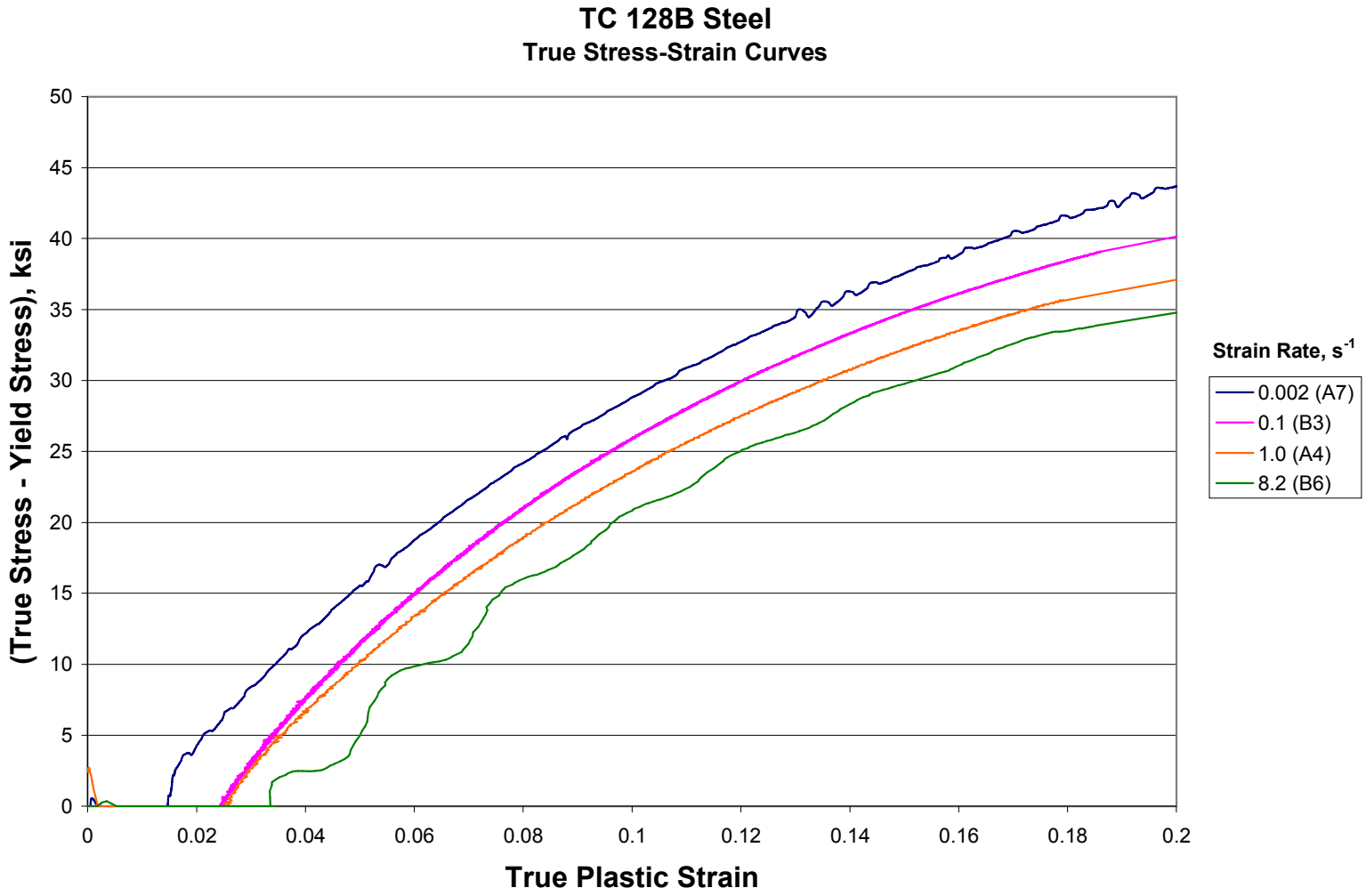

FIGURE 2.1 Typical stress-strain behavior for TC 128B steel at various train rates.

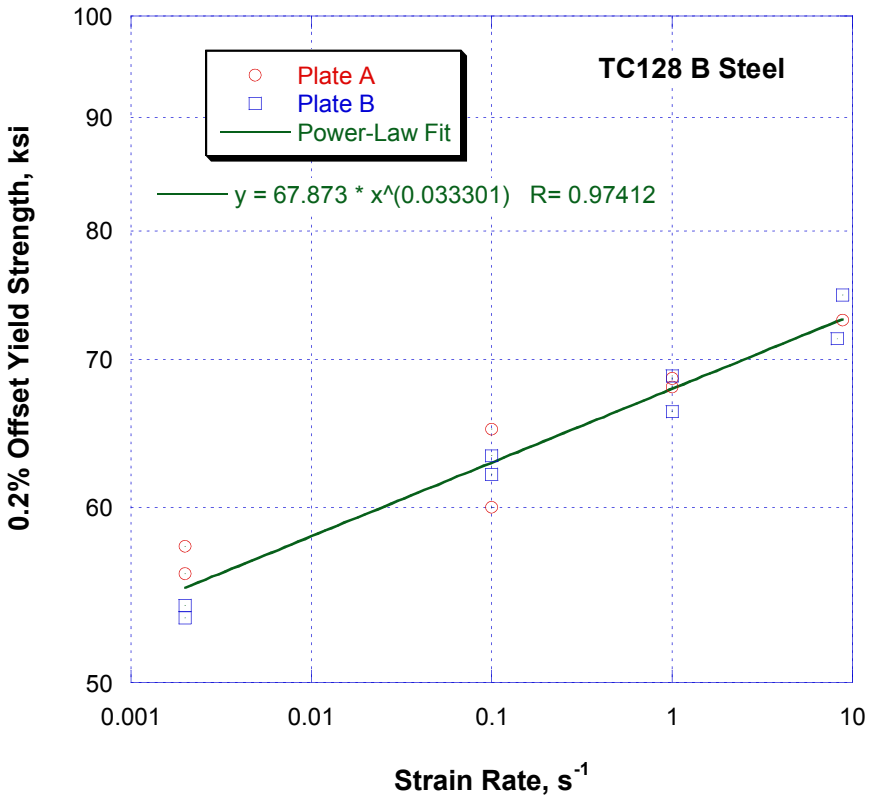

FIGURE 2.2 Effect of strain rate on yield strength of TC 128B steel.

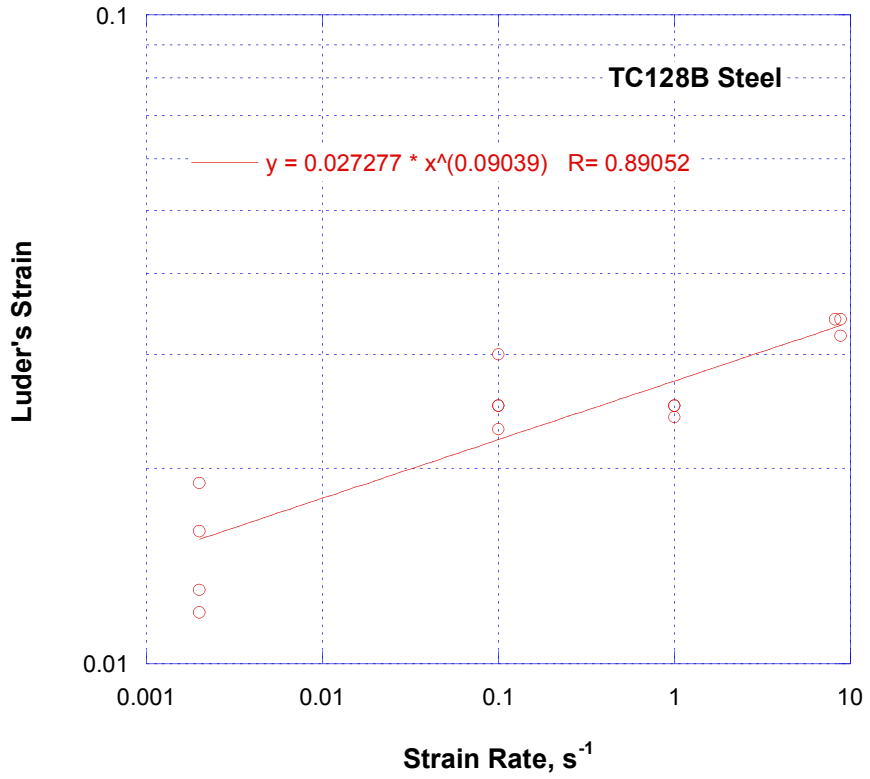

FIGURE 2.3 Effect of strain rate on Luder's (yield plateau) strain in TC 128B steel.

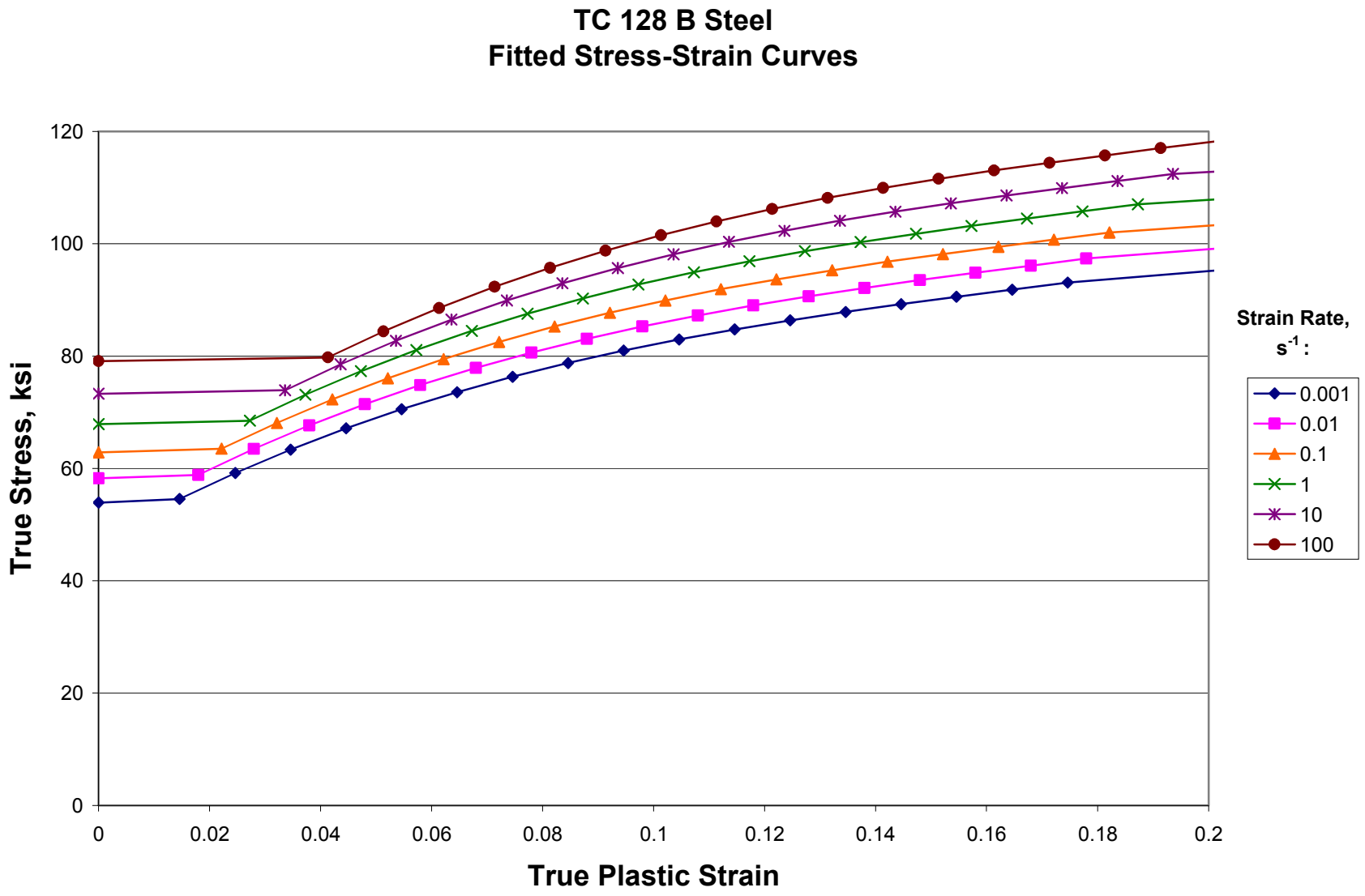

FIGURE 2.4 Fitted stress-strain curves for TC 128B steel, which were used in the finite element simulations.

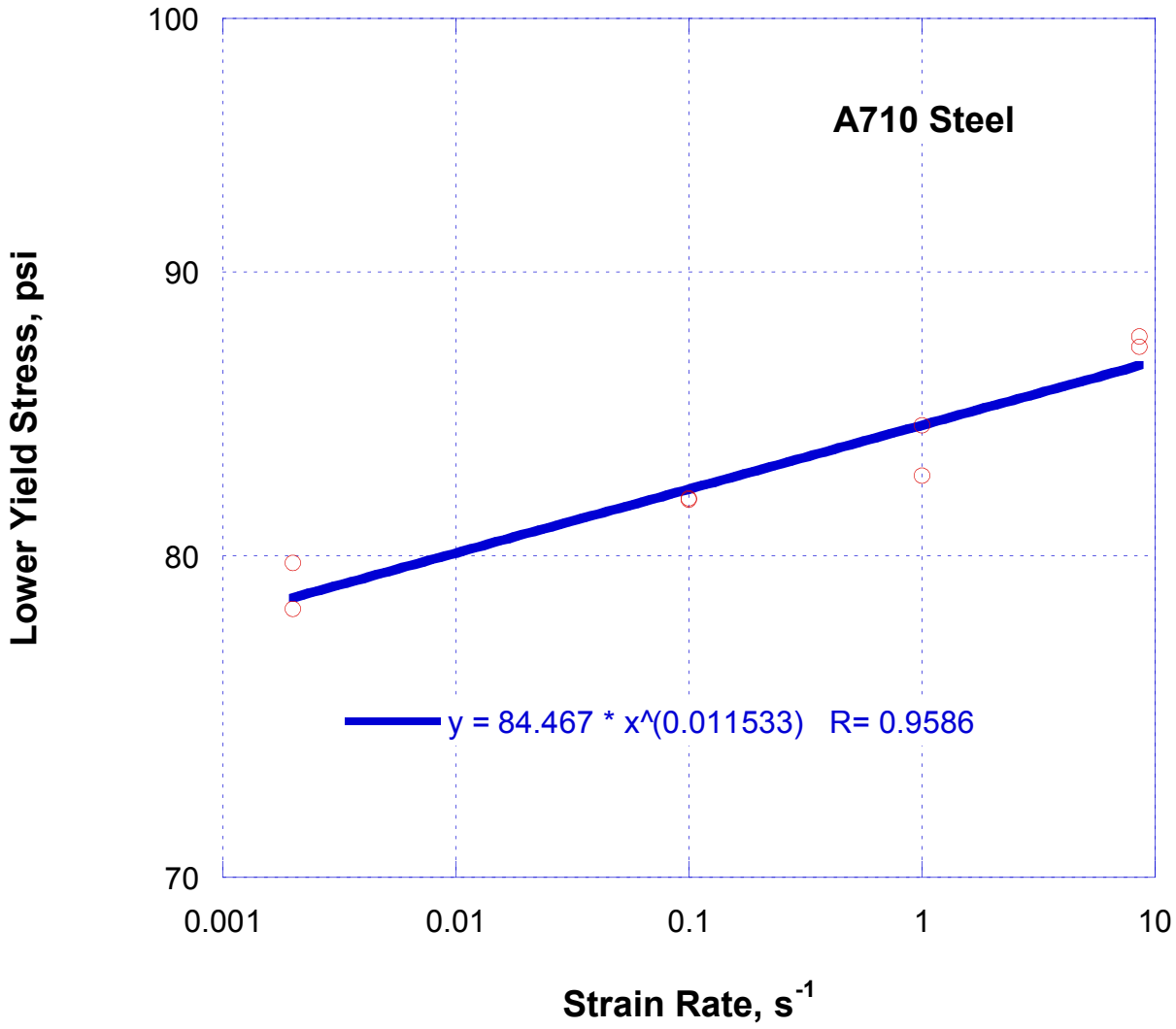

FIGURE 2.5 Effect of strain rate on yield strength in A 710 steel.

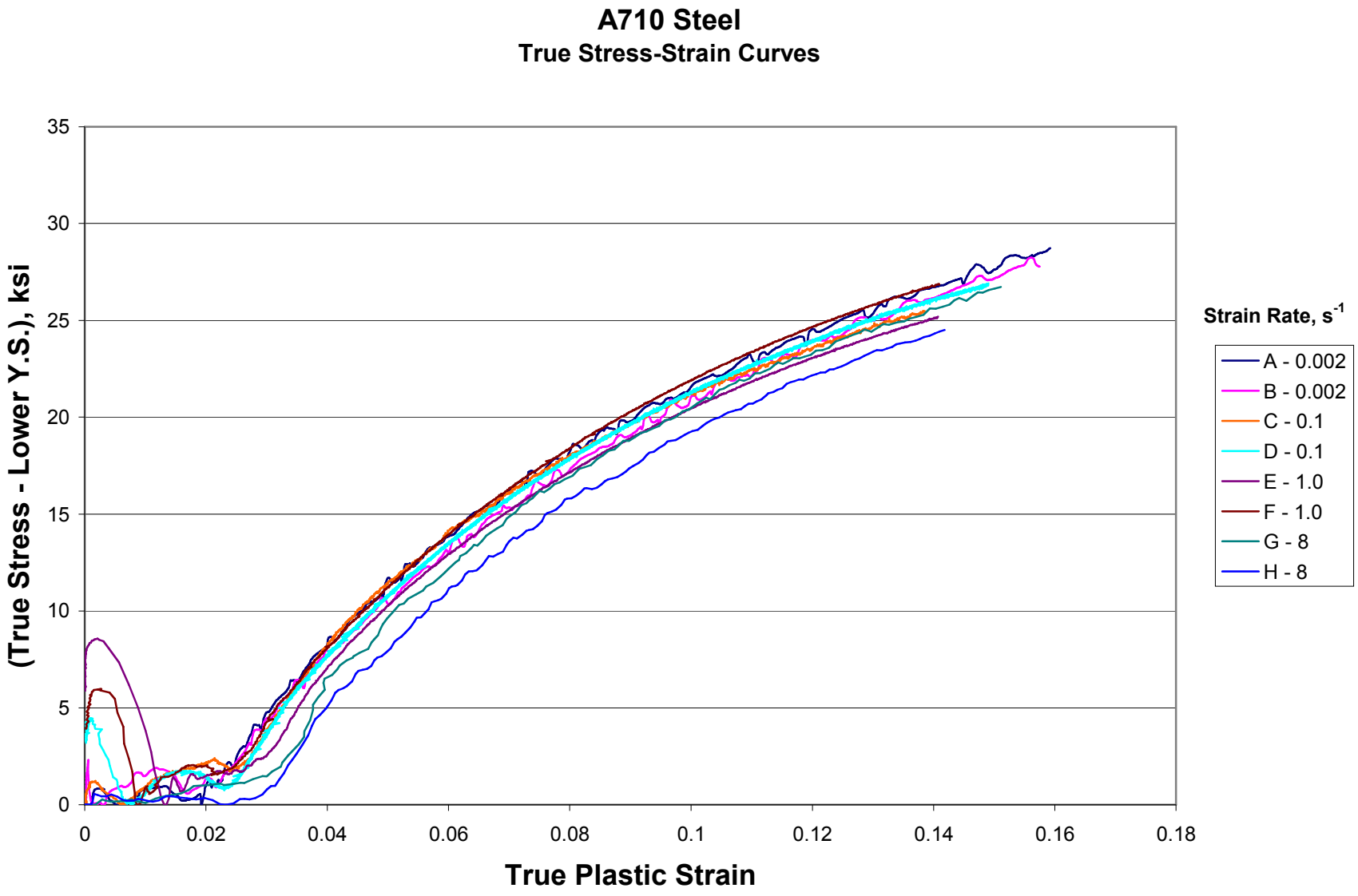

FIGURE 2.6 Stress strain behavior of A 710 steel at various strain rates.

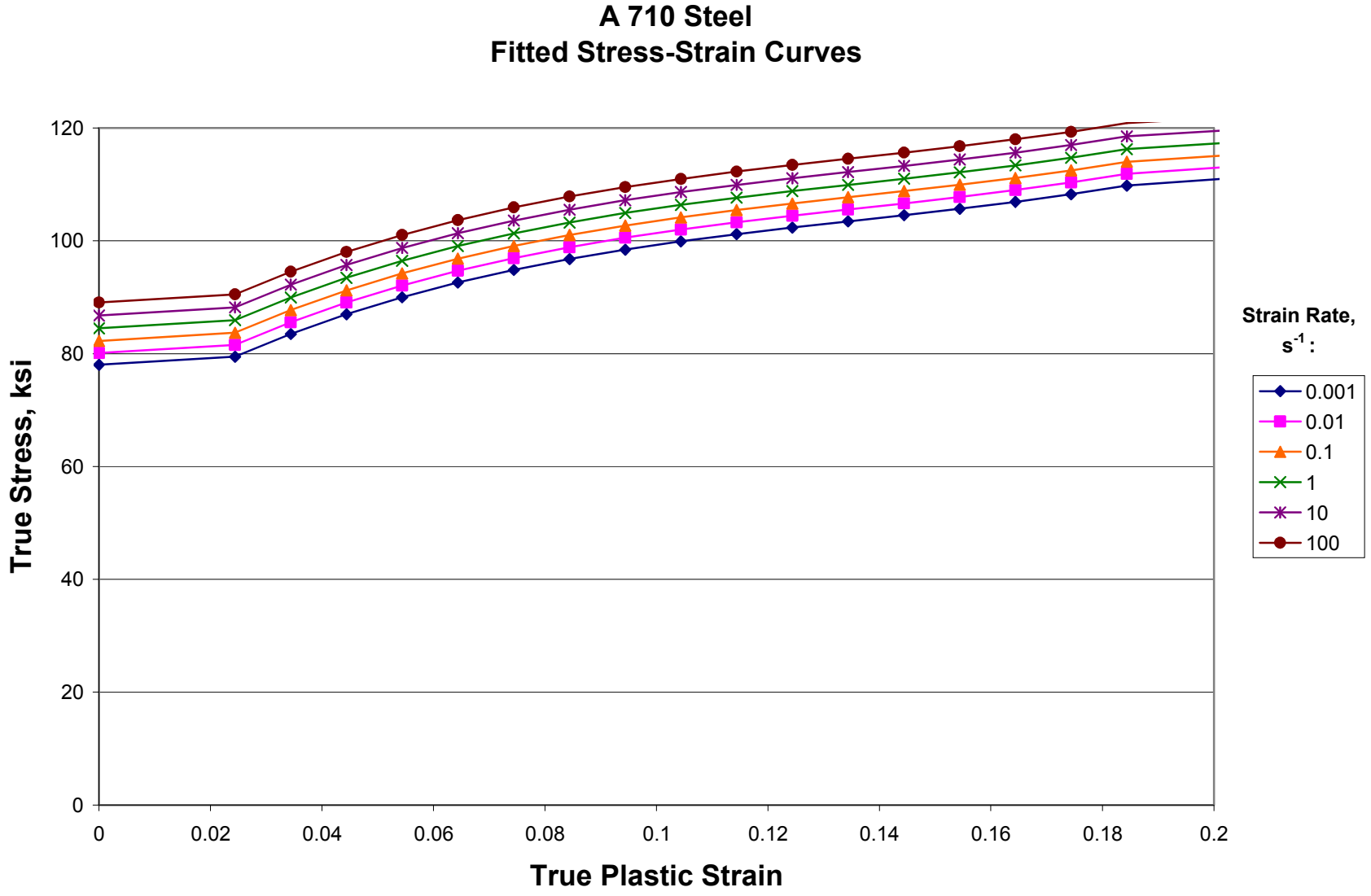

FIGURE 2.7 Fitted stress-strain curves for A 710 steel, which were used in the finite element simulations.

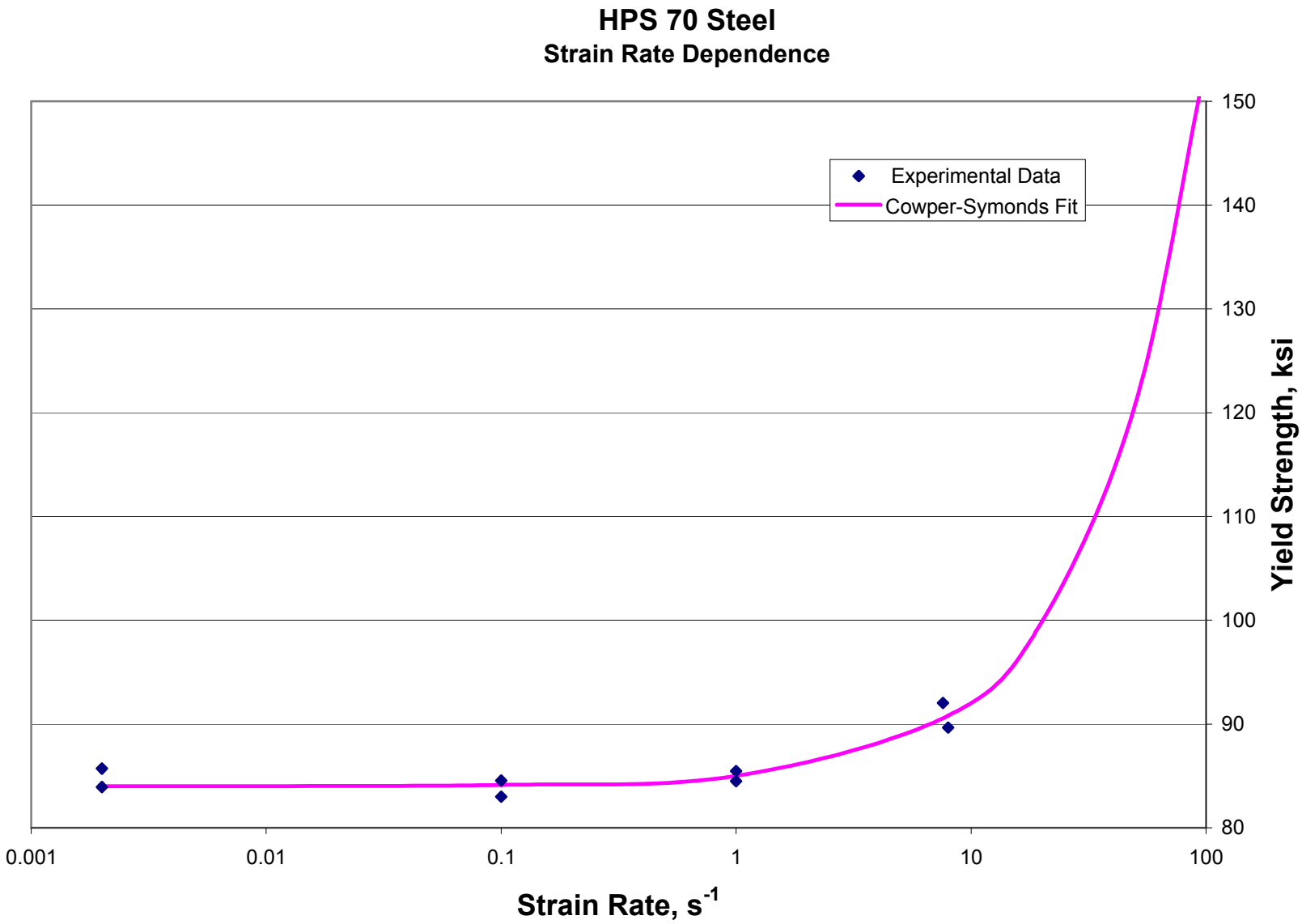

FIGURE 2.8 Effect of strain rate on yield strength in HPS 70 steel.

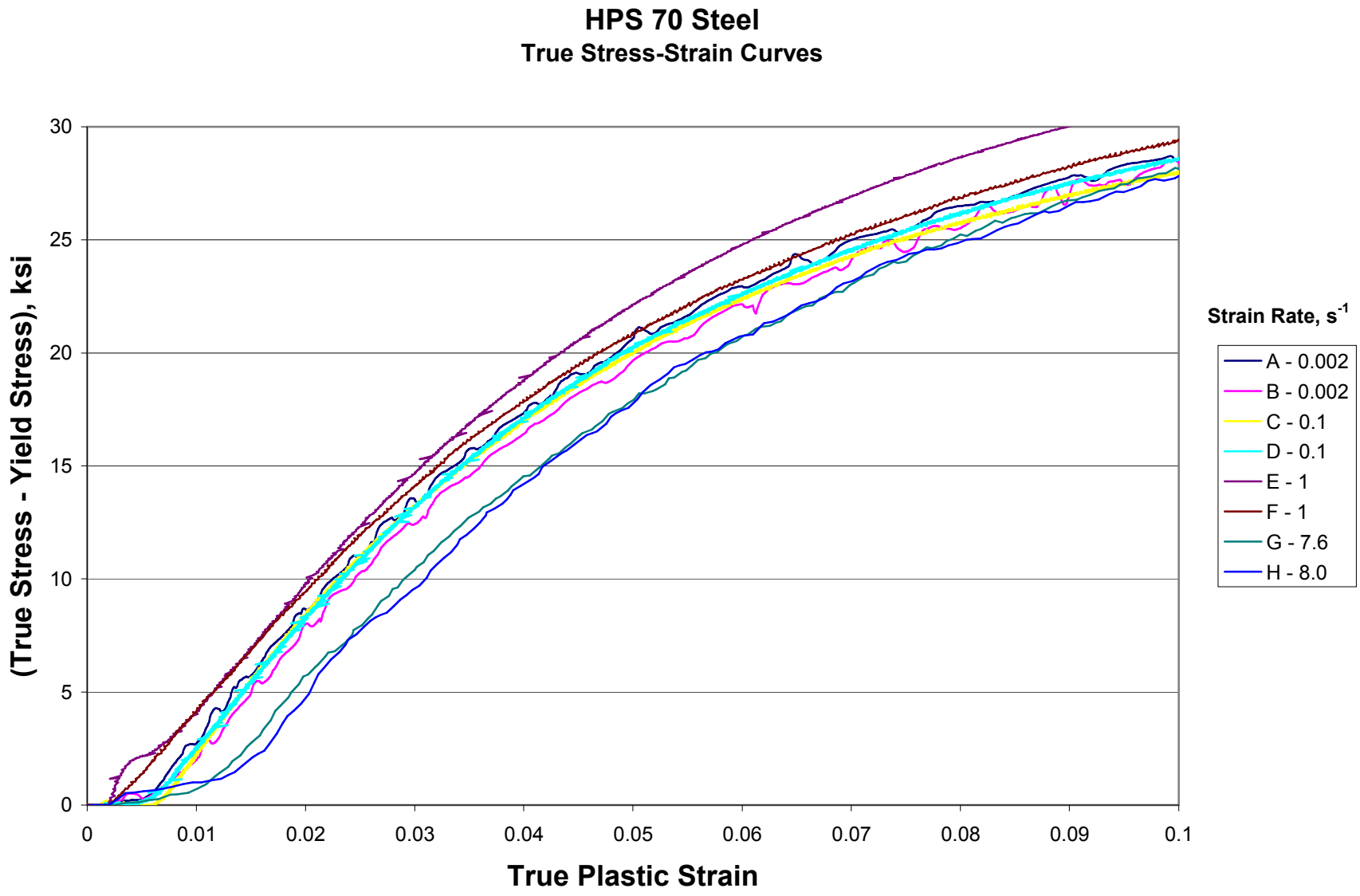

FIGURE 2.9 Stress strain behavior of HPS 70 steel at various strain rates.

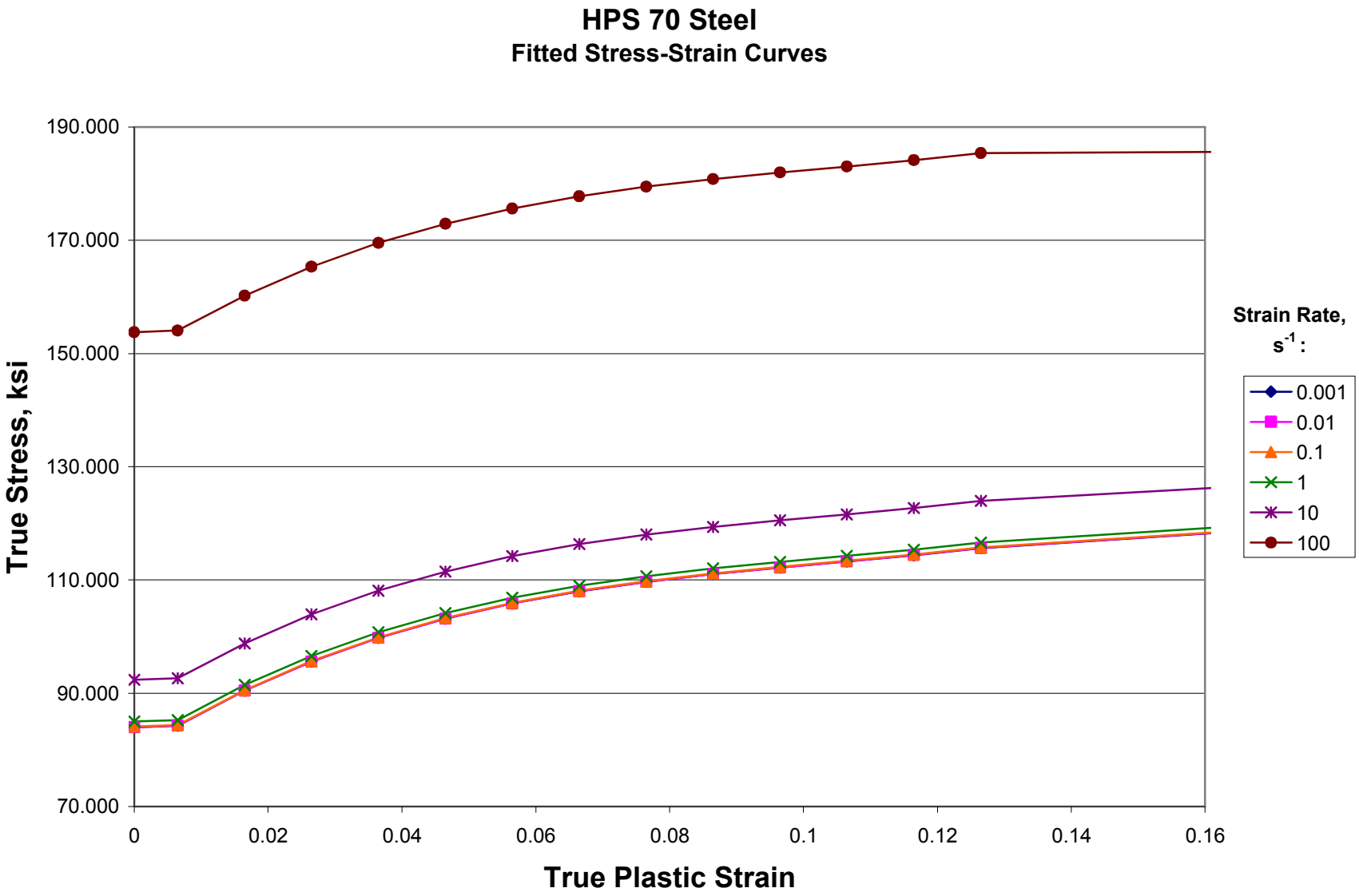

FIGURE 2.10 Fitted stress-strain curves for HPS 70 steel, which were used in the finite element simulation.

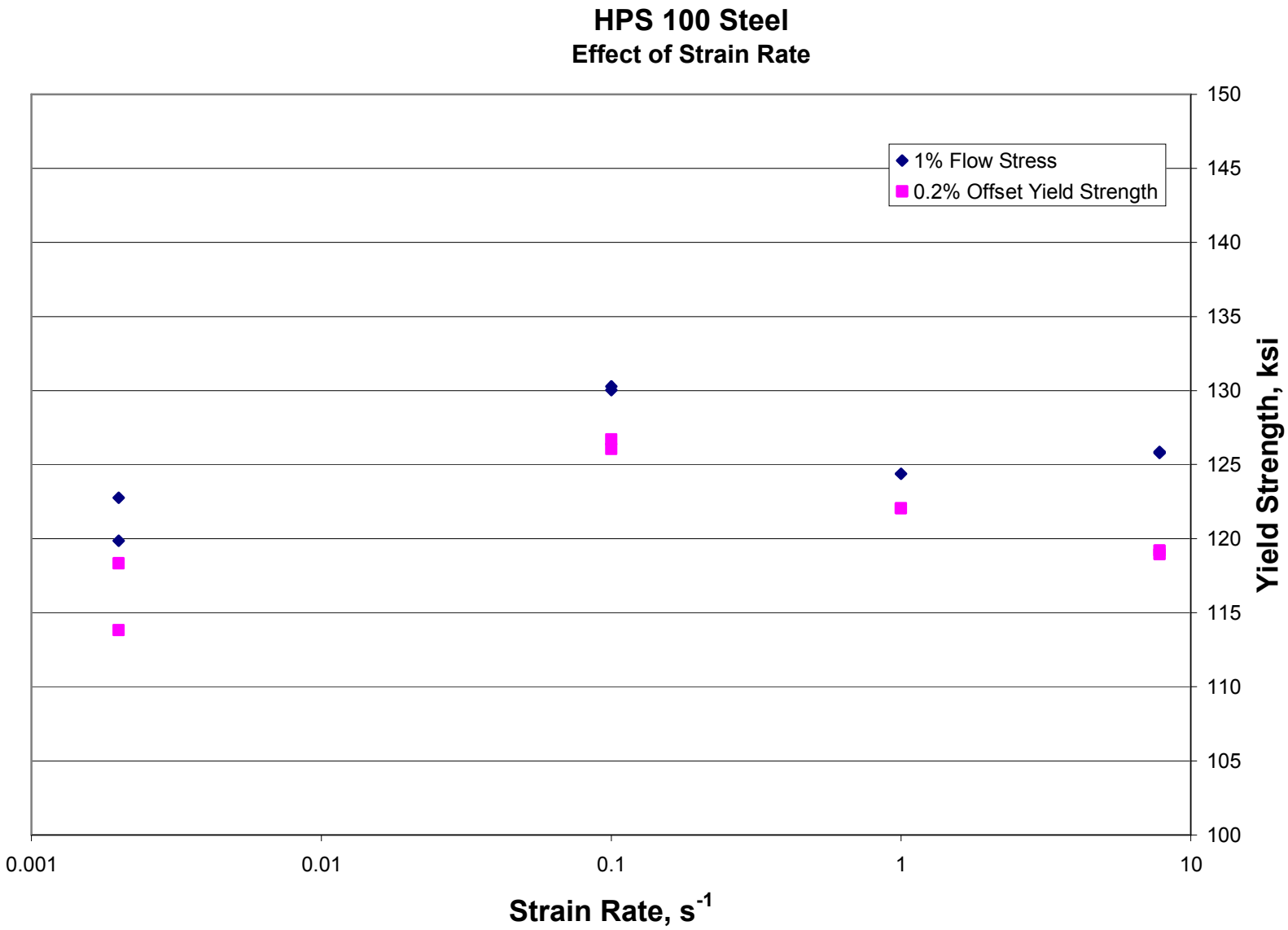

FIGURE 2.11 Yield strength and 1% flow stress versus strain rate for HPS 100 steel.

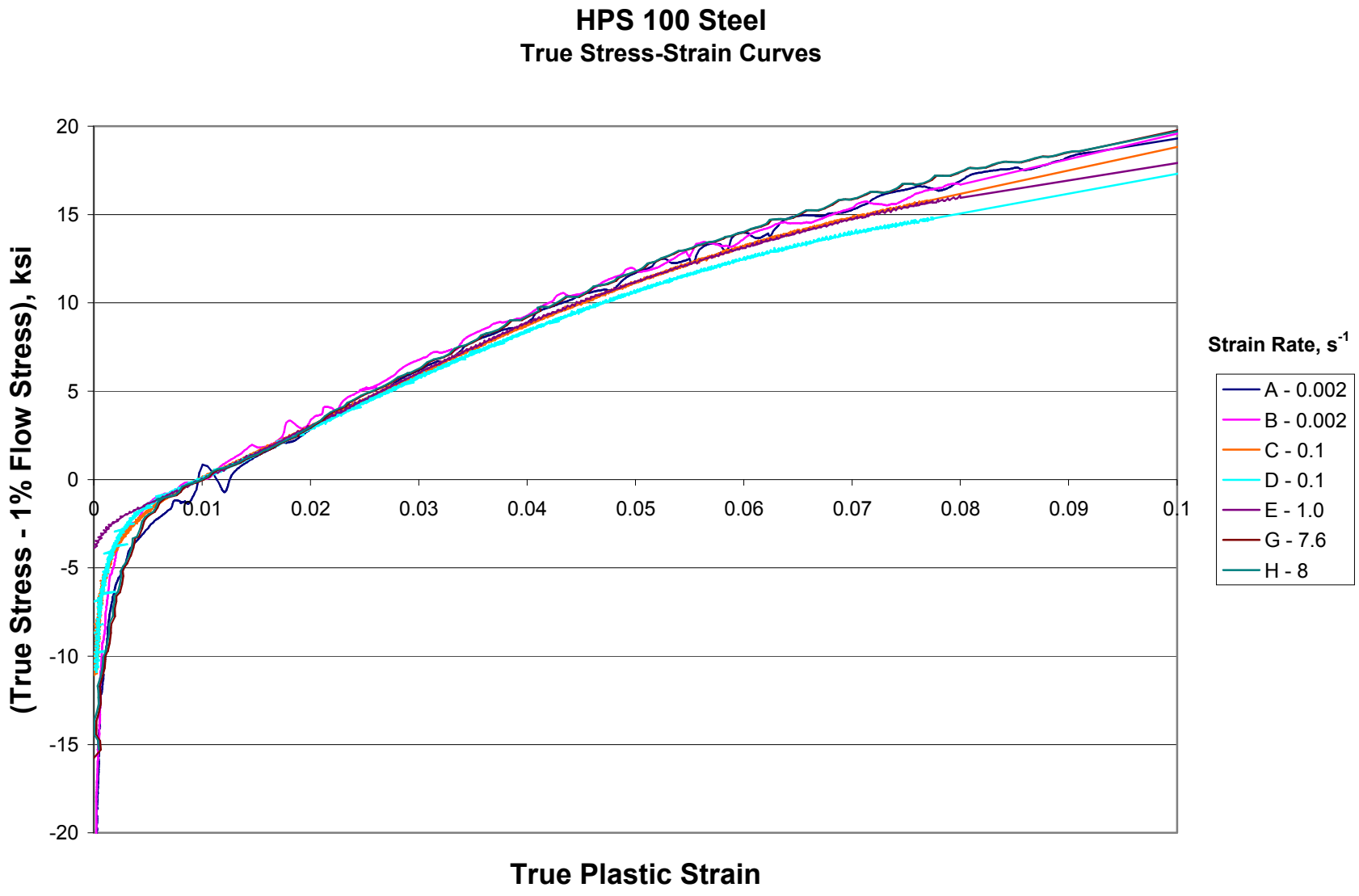

FIGURE 2.12 Stress-strain behavior of HPS 100 steel at various strain rates.

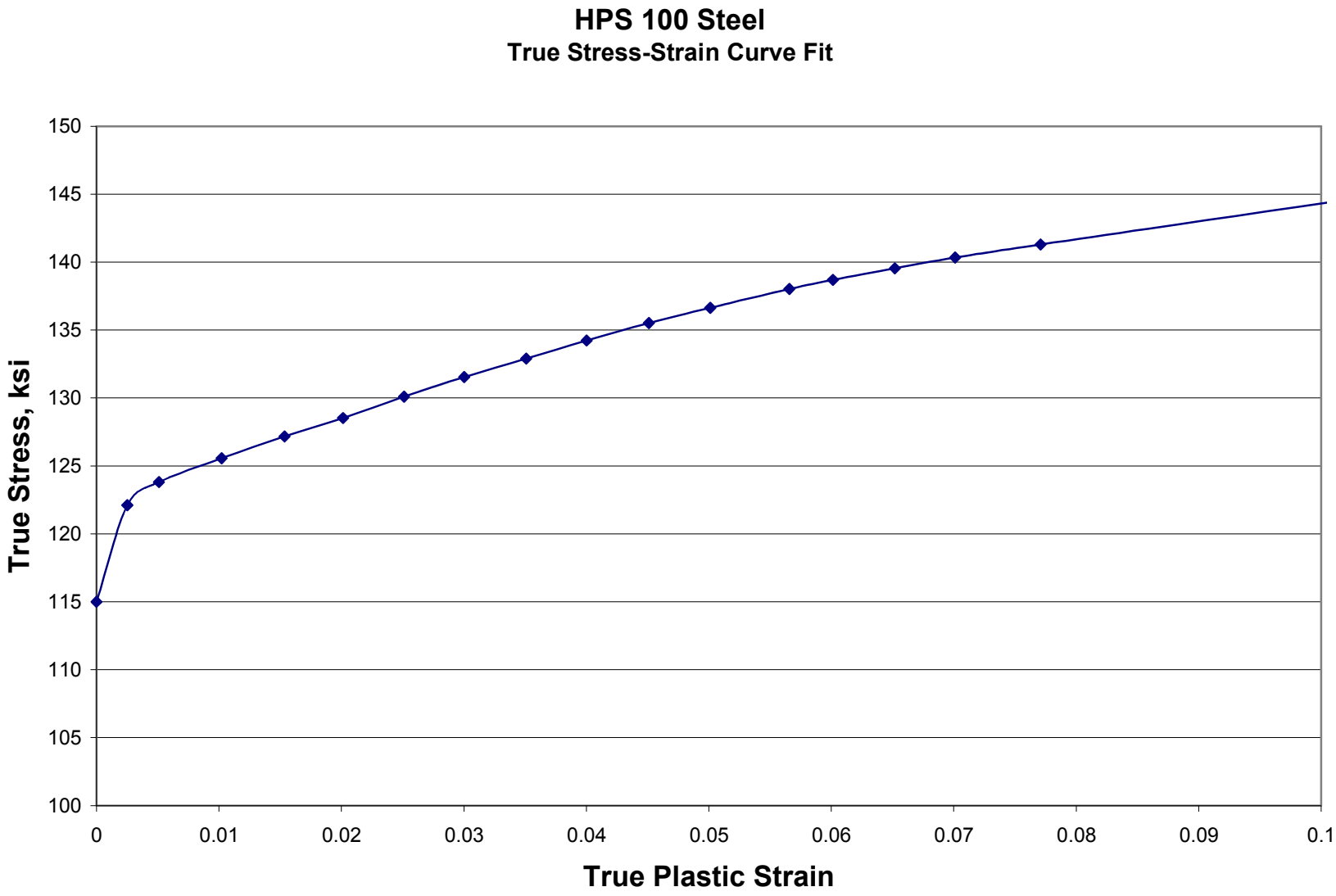

FIGURE 2.13 Fitted stress-strain curve for HPS 100 steel, which was used for finite element simulations.

2.2 Impact Tests on Unnotched Specimens

In the Phase I report [1], the authors hypothesized that puncture resistance is related to the upper-shelf toughness of the tank car material. Material toughness is typically characterized by Charpy tests, where specimens are notched, or fracture mechanics tests, where specimens contain sharp cracks. A typical puncture event, however, involves ductile fracture in the absence of a pre-existing flaw or notch-like feature.

Performing a true puncture test on steel is problematic. The test specimen must be sufficiently large to be representative of a puncture event in a tank car. Such large-scale tests necessarily involve enormous impact energies, which are beyond the capabilities of most laboratories and test facilities.

As a compromise between small-scale notched Charpy tests, which are inexpensive but do not give a direct measure of puncture resistance, and full-scale puncture tests, which are very expensive and can be performed only at a few facilities (e.g. the Transportation Technology Center in Pueblo, Colorado), we developed an unnotched impact material test specifically for this Phase II study. Unnotched specimens absorb considerably more energy than notched specimens, so the energy requirements are substantial even for relatively small specimens. Southwest Research Institute (SwRI) has a large impact test machine that was built for a previous project. This test rig delivers an impact load with a pendulum mechanism, and resembles a giant Charpy machine. The SwRI pendulum test rig was modified and re-purposed for the present project. It has been designated as the Bulk Fracture Charpy Machine (BFCM).

Figure 2.14 is a drawing of the unnotched specimen used in the BFCM test. The plan dimensions are fixed, but the specimen thickness can vary. These specimens are impacted with a Charpy-like striker tup, which is shown in Fig. 2.15. Note that this striker is considerably blunter than a standard Charpy tup. Early BFCM tests with a sharper striker did not produce the desired results. A sharp striker essentially "plows" through the specimen rather than initiating ductile fracture. High speed video of BCFM tests with the striker shown in Fig. 2.15 indicate that fracture initiates on the side of the specimen that is opposite to the surface in contact with the striker.

Figure 2.16 shows two photographs that give an overall view of the BFCM. Close-up photographs of the specimen and fixture are provided in Fig. 2.17. Figure 2.18 shows photographs of fractured specimens.

The weight of the pendulum is 2378 lbs, and the arm is 52.45 inches long. For the tests reported in this study, a drop angle of 120 degrees was used, which results in an impact velocity of approximately 14 mph. A series of benchmark experiments verified that the fracture energy is insensitive to the drop angle, which is proportional to the available kinetic energy at impact.

Table 2.3 lists the room-temperature Charpy data for the materials on which BFCM testing was performed in this study. Two samples of modern normalized TC 128B steel plate, designated as C and D, were tested. Both samples, which were provided by Union Tank Car, were corner cut-outs from the fabrication of pressure car heads. Plate C was approximately 0.82-inch thick and

Plate C was 0.69-inch thick. According to information provided by Union Tank Car, both plates had low sulfur contents.

Plates C and D have essentially identical Charpy properties in the longitudinal orientation. Moreover, the longitudinal and transverse properties of Plate D are virtually identical, indicating that this plate was manufactured with sulfide shape control. In Plate C, however, there is a significant difference between transverse and longitudinal Charpy toughness, which indicates that the sulfide shape control process was less effective, assuming it was performed at all.

Of the HSLA steels tested in this study, the HPS 100 material has the best Charpy toughness. Both the HPS 100 and A 710 materials show little anisotropy between the longitudinal and transverse directions. The HPS 70 Charpy data indicate better toughness in the longitudinal direction, which is the opposite of the expected behavior. It is possible that the rolling direction on this plate sample was mis-labled.

Table 2.4 lists the results of the BFCM testing. The thickness was varied in the Plate C samples in order to establish the energy versus thickness trend. The other materials were tested at a single thickness. These data are compared with finite element predictions in Section 3.3.

TABLE 2.3
Room temperature Charpy data for materials on which BFCM testing was performed.

Material	Room Temperature Charpy Data, ft-lb					
	Longitudinal Orientation			Transverse Orientation		
	Values	Mean	Std. Dev.	Values	Mean	Std. Dev.
TC 128B Sample C	84 87 100	90	8.5	49 53 54	52	2.6
TC 128B Sample D	79 99 83	87	10.6	98 95 82	92	8.5
A 710	192 167 167	175	14.4	180 156 157	164	13.6
HPS 70	96 107 112	105	8.2	65 65 57	62	4.6
HPS 100	154 169 167	163	8.1	194 182 179	185	7.9

TABLE 2.4
BFCM Test results.

Material	Specimen Thickness, in	Specimen Orientation	Absorbed Energy, ft-lb	Mean, ft-lb	Std Dev., ft-lb
TC 128 B Sample C	0.8205	Longitudinal	6913	7002	163
	0.8215		7181		
	0.8180		7092		
	0.8270		6824		
	0.6265	Longitudinal	4382	4277	114
	0.6250		4292		
	0.6255		4156		
	0.5005	Longitudinal	3125	3416	45
	0.5005		3170		
	0.5045		3214		
	0.3760	Longitudinal	2332	2303	25
	0.3770		2289		
	0.3755		2289		
	0.2540	Longitudinal	1472	1430	73
	0.2490		1346		
	0.2505		1472		
TC 128 B Sample D	0.6855	Longitudinal	5107	4994	114
	0.692		4835		
	0.6935		5016		
	0.6945		5016		
	0.6825	Transverse	5062	4994	59
	0.686		4925		
	0.689		5016		
	0.687		4971		
A 710	0.7835	Transverse	6104	6149	64
	0.787		6194		
	0.7945		5832*		
HPS 70	0.7665	Transverse	5968	5821	238
	0.779		5877		
	0.7705		5968		
	0.7665		5470		
HPS 100	0.773	Transverse	7270	7192	207
	0.7785		7003		
	0.776		7047		
	0.776		7448		

* Value is not used in average or standard deviation because the specimen is thinner on one end.

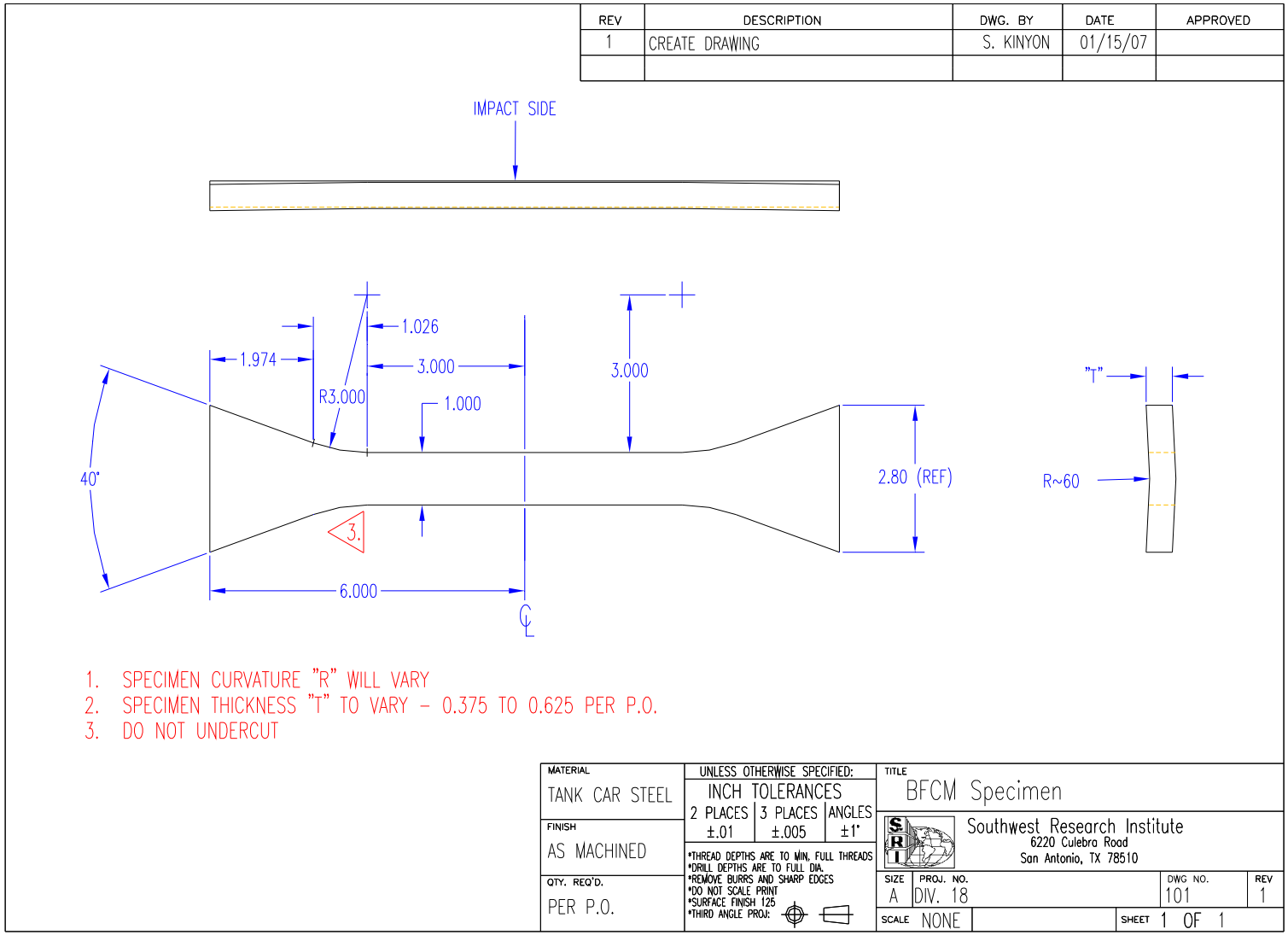

FIGURE 2.14 BCFM specimen configuration.

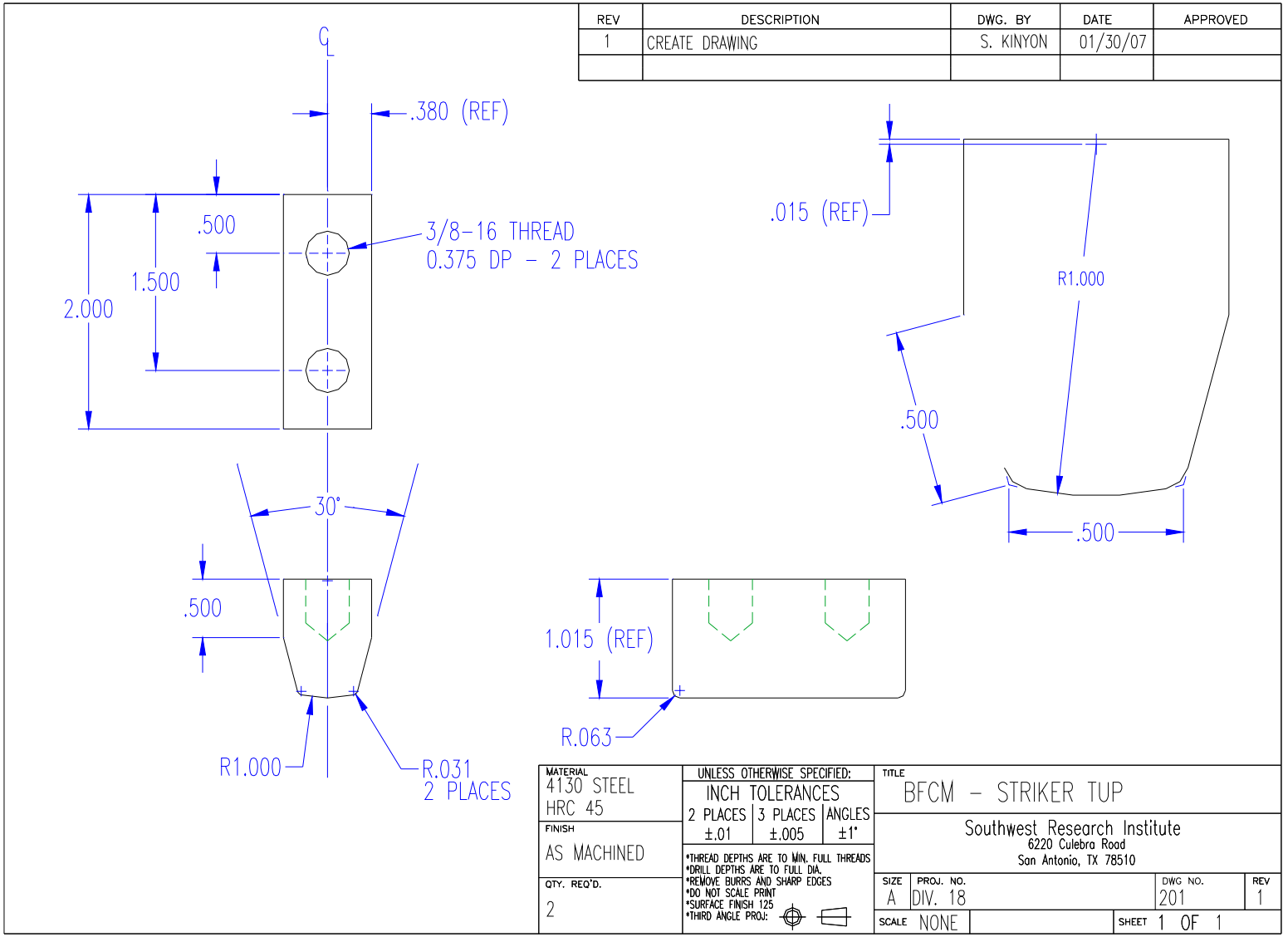

FIGURE 2.15 Striker tub used in BFCM tests.

(a)

(b)

FIGURE 2.16 Photographs of the BFCM test machine, which is located at Southwest Research Institute.

(a)

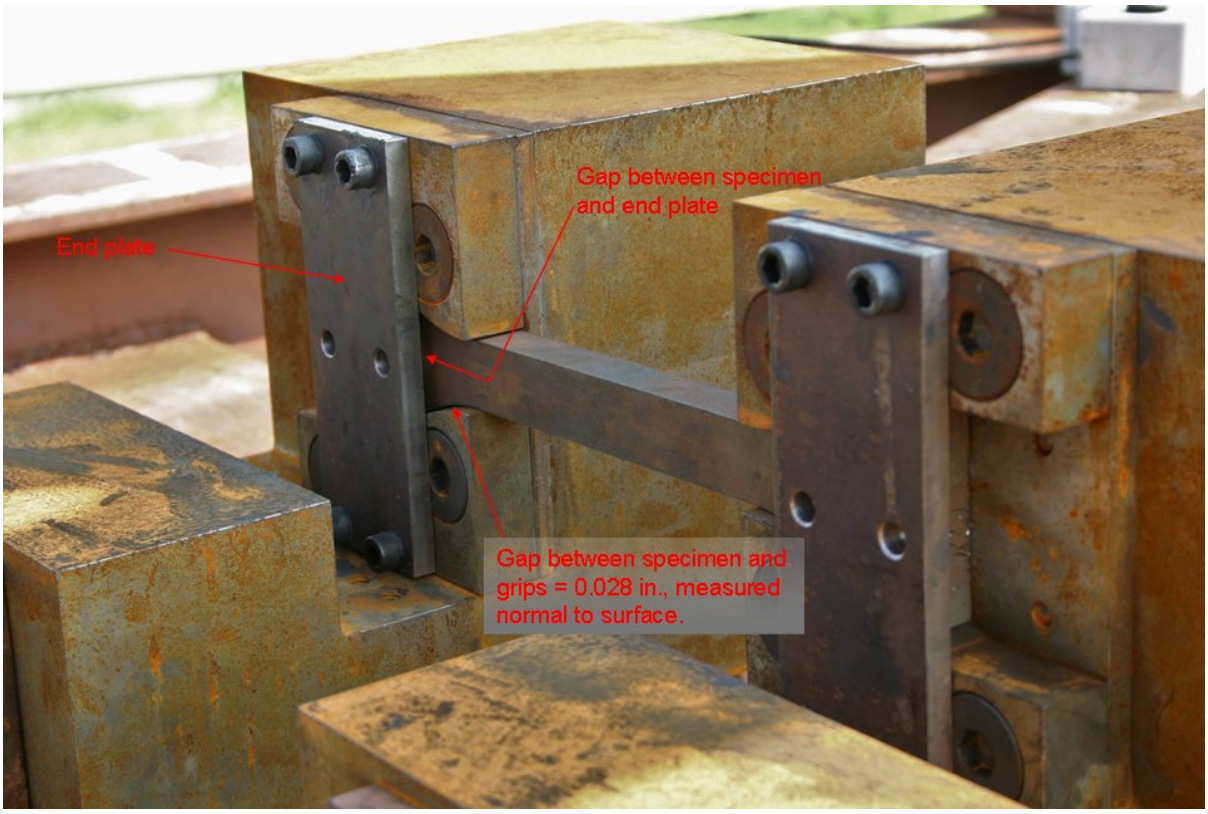

(b)

FIGURE 2.17 Close-up photos of the BCFM specimen in the test machine.

(a)

(b)

FIGURE 2.18 Fractured BFCM specimens.

3 MATERIAL MODEL CALIBRATION

The Gurson-Tvergaard material model, which was applied in the Phase I project [1], was also used in the present study to simulate laboratory fracture tests and full-scale tank car impact events.

3.1 Gurson-Tvergaard Ductile Fracture Model

The Gurson-Tvergaard model [2-6] simulates void growth and ductile fracture through a strain-softening constitutive law. Strain softening is captured through a void volume fraction, which increases with plastic flow. Fracture occurs when the void volume fraction reaches a critical value. This material model is implemented in some commercial finite element codes, including ABAQUS Explicit and LS-DYNA.

The Gurson-Tvergaard yield condition is given by:

$$\Phi = \left(\frac{q}{\sigma_y}\right)^2 + 2q_1 f \cosh\left(-q_2 \frac{3p}{2\sigma_y}\right) - \left(1 + q_3 f^2\right) = 0 \tag{3.1}$$

where q is the effective Mises stress, p is the hydrostatic pressure, σ_y is the yield stress of the fully dense material, q_1, q_2, q_3 are porosity material parameters, and f is the void fraction.

The void growth and void nucleation rate gives the total change in the void volume fraction, $\dot{f}$:

$$\dot{f} = \dot{f}_{gr} + \dot{f}_{nucl} \tag{3.2}$$

where $\dot{f}_{gr}$ is from the existing void growth, and $\dot{f}_{nucl}$ is from the nucleation of new voids. The growth of existing voids is given by:

$$\dot{f}_{gr} = \left(1 - f\right)\dot{\varepsilon}^{pl} \tag{3.3}$$

and the growth of new voids due to nucleation is given by:

$$\begin{aligned} \dot{f}_{nucl} &= A\dot{\bar{\varepsilon}}_m^{pl} \\ A &= \frac{f_N}{s_N\sqrt{2\pi}} \exp\left[-\frac{1}{2}\left(\frac{\bar{\varepsilon}_m^{pl} - \varepsilon_N}{s_N}\right)^2\right] \end{aligned} \tag{3.4}$$

The nucleation strain is assumed to follow a normal distribution with a mean value of ε_N, and a standard deviation s_N. f_N is the void volume fraction of the new voids; which are nucleated only in tension.

For a numerical analysis, the initial void volume fraction, f_0, is defined for the material. The porous failure criteria is given by the critical void volume fraction, f_c. When $f \geq f_c$ at all the material points (integration points) of a finite element, the stress carrying capacity of the material is reduced to zero and the finite element is removed from the model. The progressive failure of elements results in crack growth across the mesh.

3.2 Charpy Specimen

In order to apply the Gurson-Tvergaard model to a particular problem, the model must first be calibrated to experimental results. In this instance, we chose to calibrate the material model to Charpy impact results. A series of finite element simulation of Charpy tests were performed, and the material model was adjusted to achieve various values of absorbed energy.

Figure 3.1 shows the finite element model used for Charpy simulations, which were performed with ABAQUS Explicit. The anvil and striker were treated as contact surfaces, so the specimen is free to move relative to the test machine during fracture. The initial velocity of the striker was 235.9 in/sec (13.4 mph), which is equivalent to being dropped from a height of 6 ft. The velocity of the striker decreased as it imparted its kinetic energy to the specimen. This effect is handled automatically in the analysis through energy conservation. The weight of the striker was 49.15 lb, so the total available energy was 295 ft-lb. The fracture energy is equal to the total internal energy absorbed by the specimen. This quantity is output by ABAQUS Explicit.

The stress-strain curves used in the analyses are given in Section 2.1. Based on the work of Faleskog, et al [6], the Gurson parameters listed below are appropriate for steels with the strength and hardening properties of TC 128 B steel. These same constants were used for the other materials for the sake of simplicity.

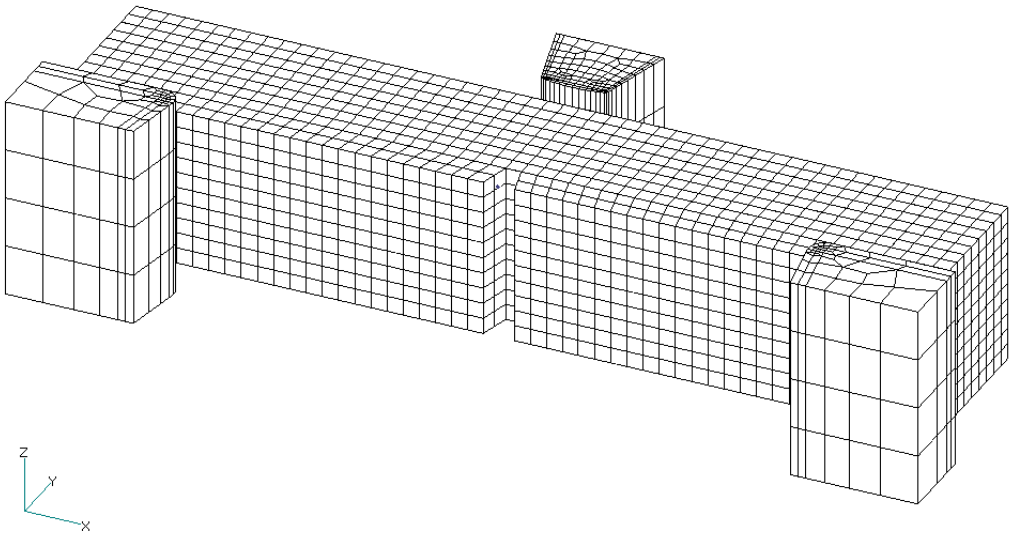

FIGURE 3.1 Finite element model for simulation of the Charpy test.

Gurson parameter $q_1 = 1.81$
Gurson parameter $q_2 = 0.82$
Gurson parameter $q_3 = q_1^2 = 3.2761$
Nucleation strain mean value $\varepsilon_N = 0.30$
Nucleation strain standard deviation $s_N = 0.10$
Void nucleation initial void volume fraction $f_N = f_0$
Critical void fraction $f_c = 0.15$

The initial void fraction, f_o, was a fitting parameter in the model.

Figure 3.2 is a plot of absorbed energy versus initial porosity for the 4 steels considered in this study. It is important to note that these calibration curves apply only to 1 mm^3 elements. Finite element fracture models, where an element is deleted when a failure criterion is reached, are inherently mesh dependent. Real materials contain microstructural length scales, such as grain size and inclusion spacing, that govern toughness. In a finite element model, the de facto length scale is the element size. The material model must be re-calibrated for each element size. Increasing the element size shifts the calibration curve (absorbed energy vs. f_0) upward and to the right. This point is discussed further in Section 3.4

Note that the assumed strain rate dependence on tensile properties has an effect on the calibration curve for HPS 70 steel. The energy versus porosity curve is considerably higher when flow properties are extrapolated using Eq. (2.1).

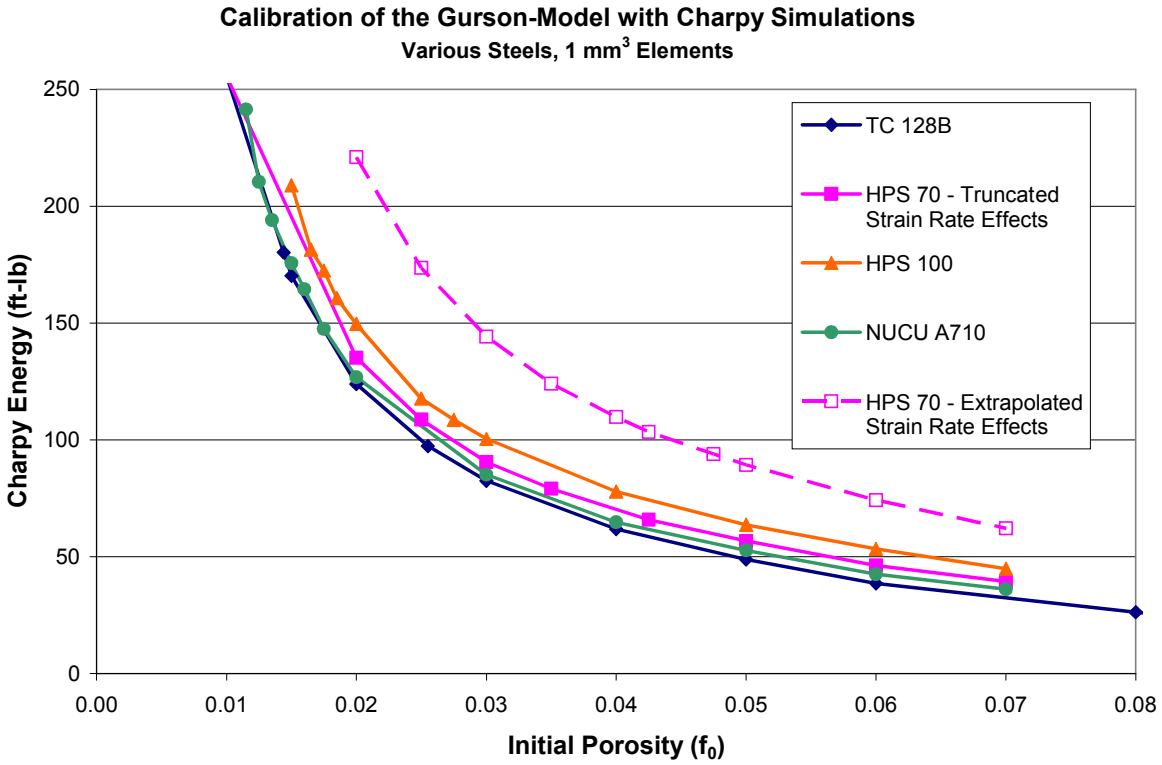

FIGURE 3.2 Calibration of initial porosity, f_o, to Charpy energy for 1 mm^3 elements.

3.3 BFCM Specimen

The material fracture model was calibrated to notched Charpy tests, but puncture in tank cars typically occurs in the absence of pre-existing notch-like features. In order to determine whether or not the material model calibrated to Charpy data is applicable to unnotched configurations, finite element simulations of the BFCM specimens were compared to the experimental results.

Figures 3.3 and 3.4 show a typical finite element model of the BFCM test. For clarity, the grips and endplates are not shown. In the impact zone the elements were 1 mm wide by 1 mm high, which corresponds to the mesh size in the Charpy specimens. (Recall the earlier discussion about the material model calibration being mesh sensitive.) The element dimension in the specimen thickness direction was *very close* to 1 mm, but was adjusted slightly so that the total specimen thickness would exactly match the desired value. For example, consider a specimen thickness of 0.822 inch, which corresponds to 20.88 mm. In this case, the mesh in the impact zone consists of 21 elements through the specimen thickness. Each element has the following dimensions: 1 mm x 1 mm x 0.994 mm. The latter value is the through-thickness dimension, which corresponds to 20.88 mm/21 elements.

Initial models neglected friction effects, as well as the gaps between the specimen and the fixure (Fig. 2,17). Subsequent analyses incorporated these effects in order to assess their relative effect on fracture energy. For these latter cases, a friction coefficient of 0.1 was assumed for contact between the specimen, grips, end plates and striker.

Figure 3.5 shows the simulation of a BFCM test for TC128-B steel and thickness = 0.5 in. Note that fracture initiates from the specimen surface that is opposite the surface in contact with the striker. This is consistent with observations from high-speed videography of BFCM tests.

Table 3.1 compares the predicted and experimental absorbed energies in the BCFM specimens on various materials and thicknesses. Figure 3.6 is a plot of absorbed energy versus specimen thickness for both predicted and experimental BFCM tests. A single data point for TC 128B Plate C is included along with the Plate D data because the two samples have virtually identical Charpy properties in the longitudinal direction. The predictions and experimental data agree very well for specimen thickness of 0.5 inch and below, but the model slightly under-predicts the experimental data for thicker samples. As discussed in Section 6.1, the stress state in the thinner samples, where the simulation and experimental data agree, is more representative of the stress state at puncture in tank cars.

Figure 3.7 compares predicted and experimental energies for all of the materials tested. There is very good correlation between prediction and experiment for A 710 and HPS 100 steel, but the simulation under-predicts the fracture energy in the HPS 70 steel samples. The agreement between prediction and experiment for HPS 70 steel is improved when the strain rate dependence of the tensile properties is extrapolated using Eq. (2.1). The open symbols in Fig. 3.7 correspond to analyses that incorporated friction effects as well as gaps between the specimen and the fixture. In most cases, the predicted fracture energy was not significantly affected by simplifying assumptions of the initial simulations.

Overall, the model predictions are good, but not perfect. Ideally, the model should predict energies to within 5 or 10% of experimental values in this case, which is consistent with scatter in individual experimental values. The reasons for under-predictions of > 15% in some cases are not fully understood at present. Perhaps these predictions could be improved by varying more than one parameter in the Gurson-Tvergaard material model to optimize the fit to experimental data. An exhaustive parameter study with the Gurson-Tvergaard model was beyond the scope of this project.

.

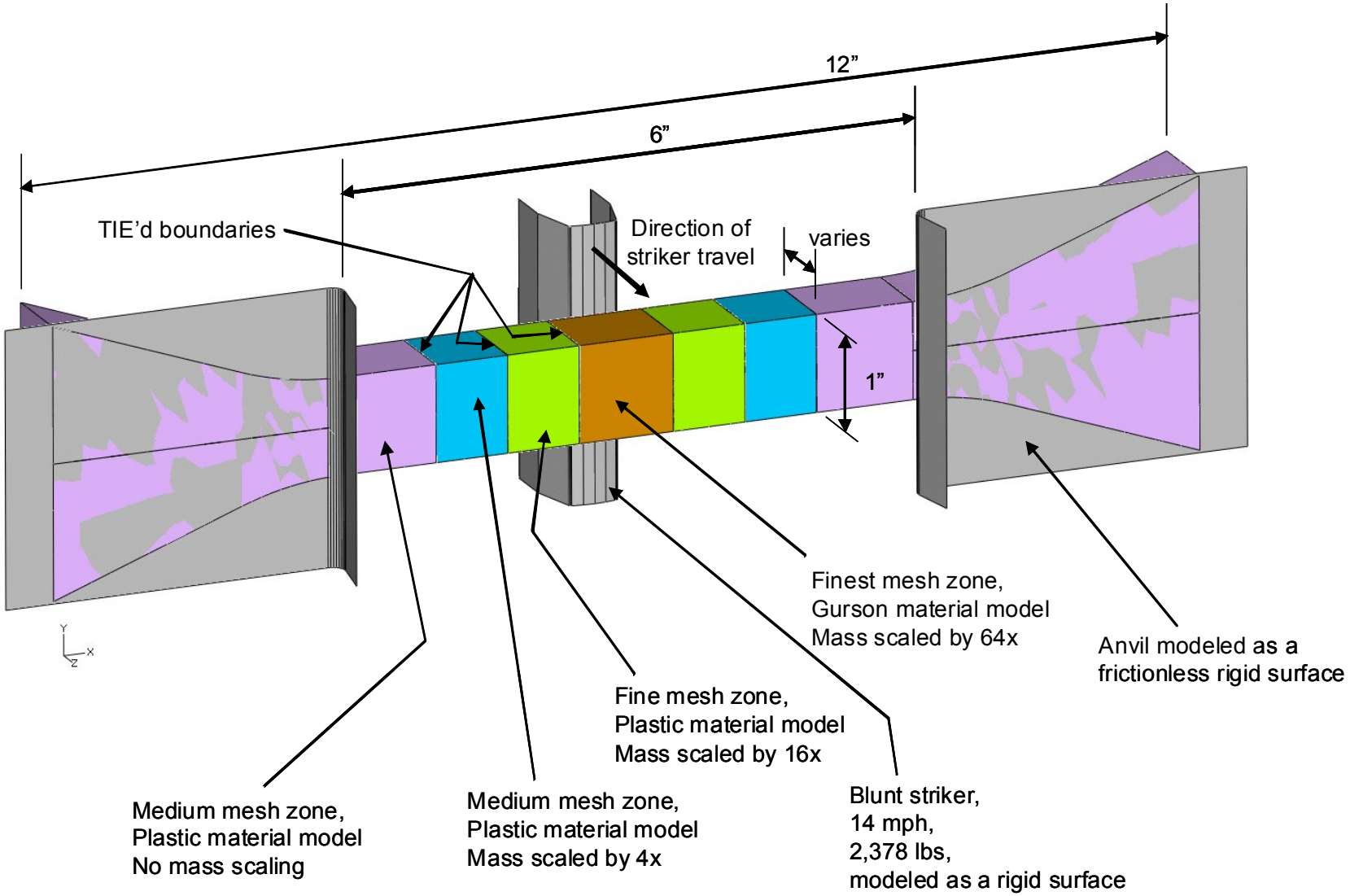

FIGURE 3.3 Finite element model of BFCM specimen (grips and end plate not shown).

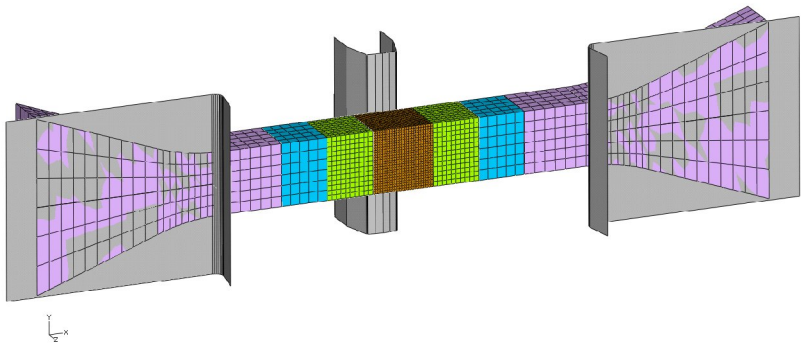

View from anvil side

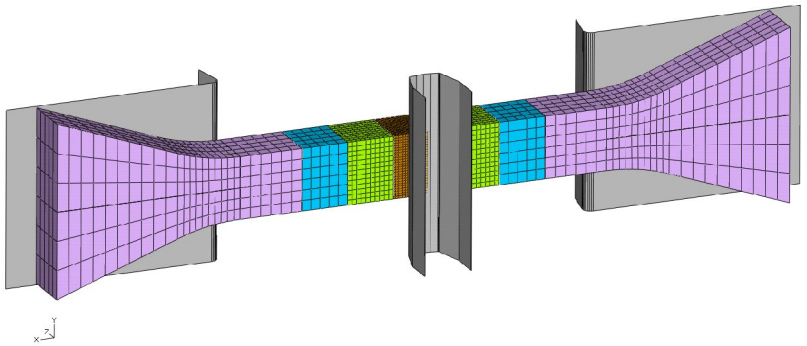

View from striker side

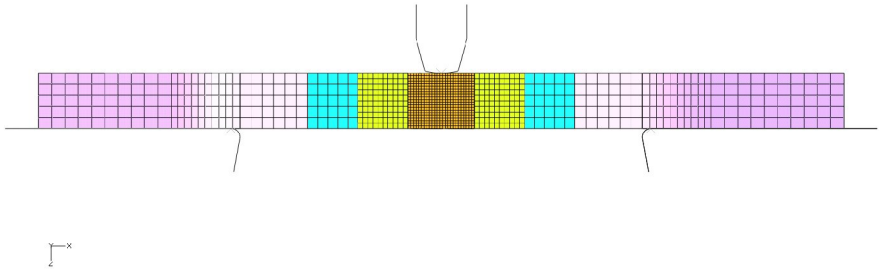

Top view

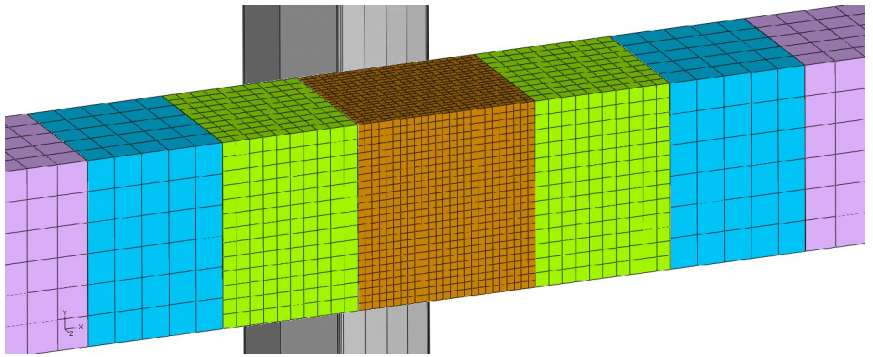

Close up of finest mesh region

FIGURE 3.4 Meshing of finite element model of BFCM specimen (grips and end plate not shown).

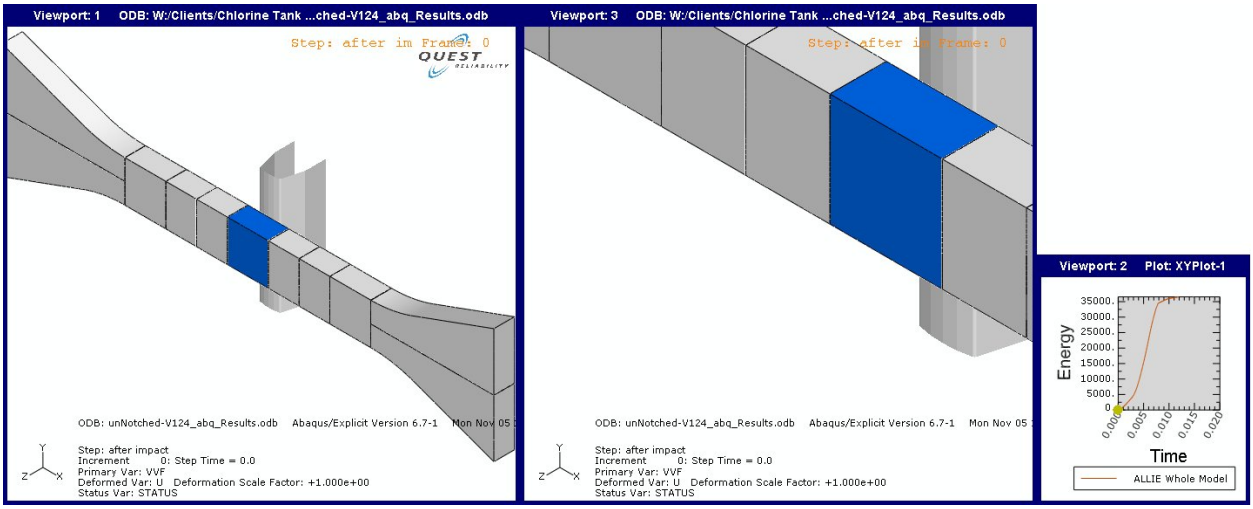

(a) Time = 0 ms

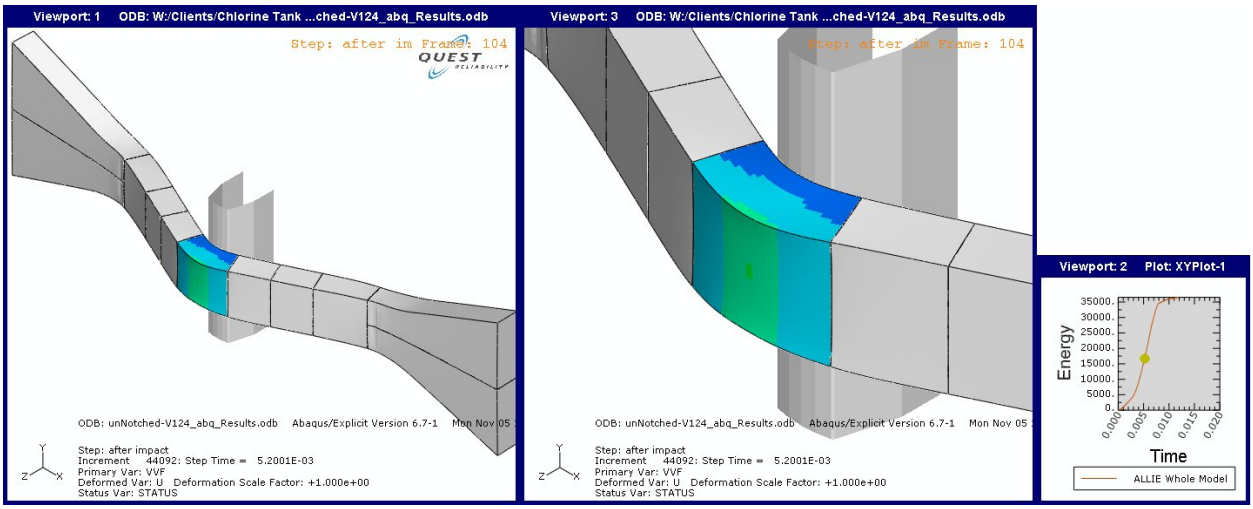

(b) Time = 5.2 ms

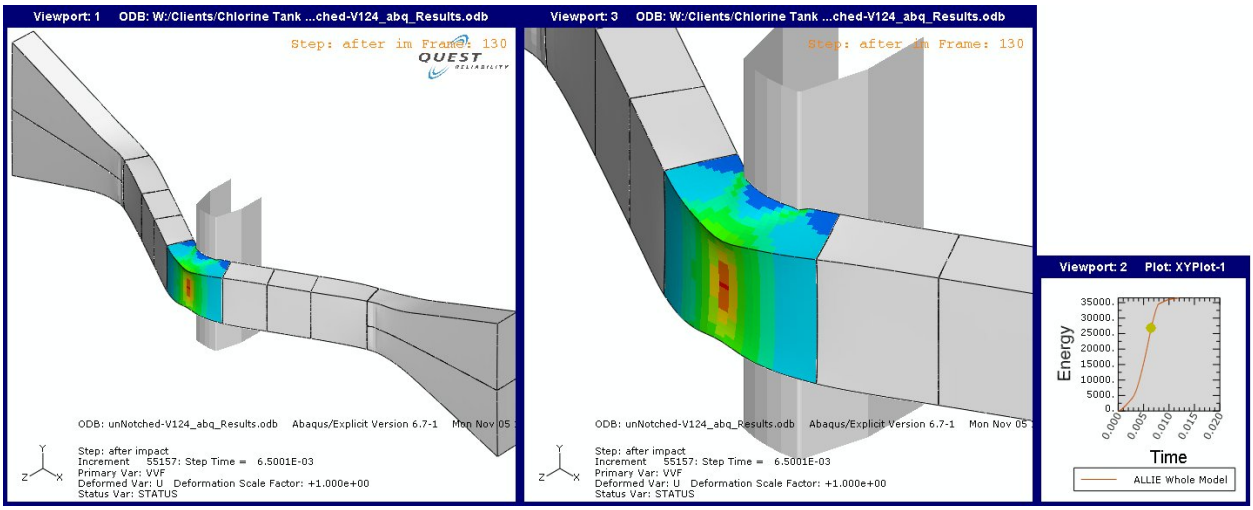

(c) Time = 6.5 ms

FIGURE 3.5 Typical results from a simulation of a BFCM test (end plates, platens & grips not shown).

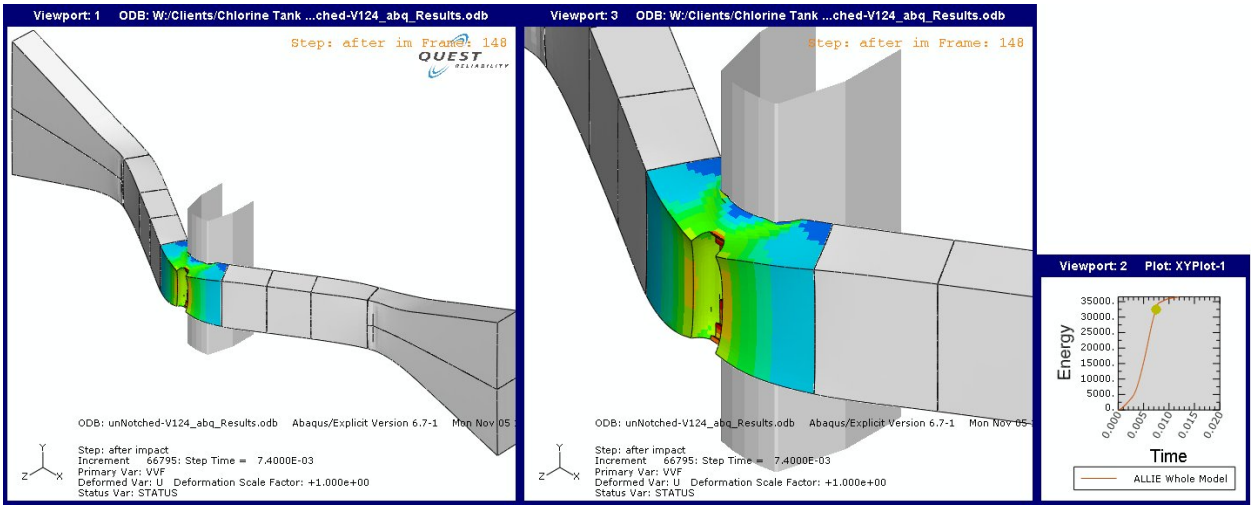

(d) Time = 7.4 ms

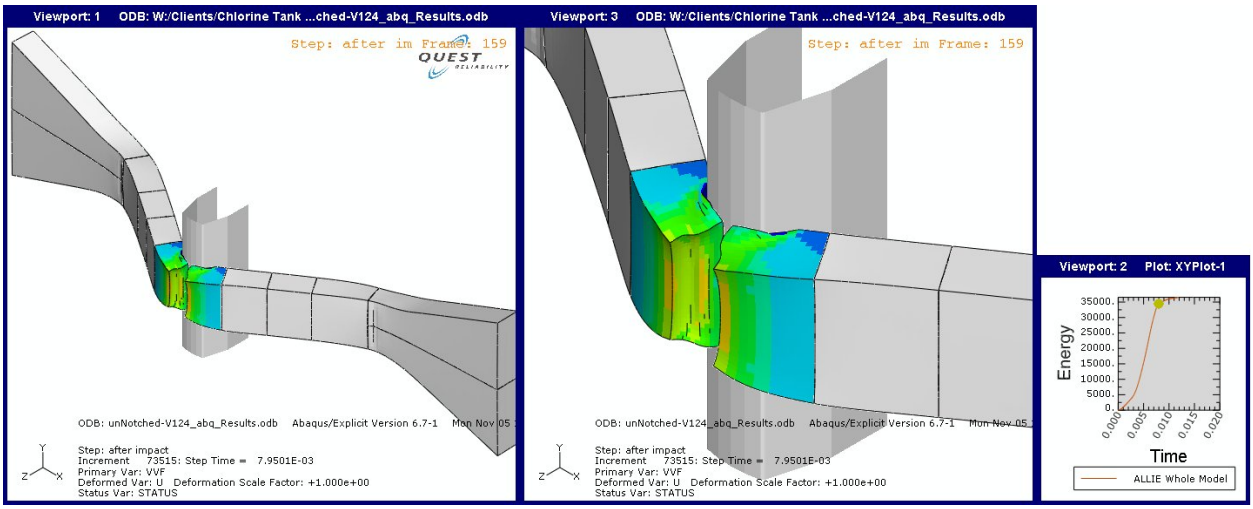

(e) Time = 8.0 ms

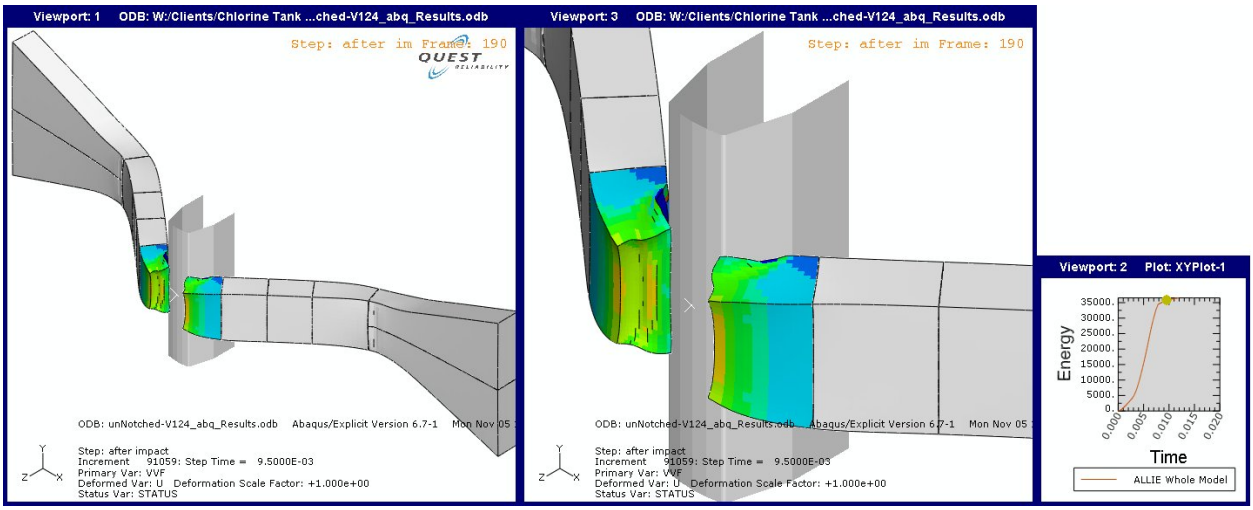

(f) Time = 9.5 ms

FIGURE 3.5 (cont.) Typical results from a simulation of a BFCM test (end plates, platens & grips not shown).

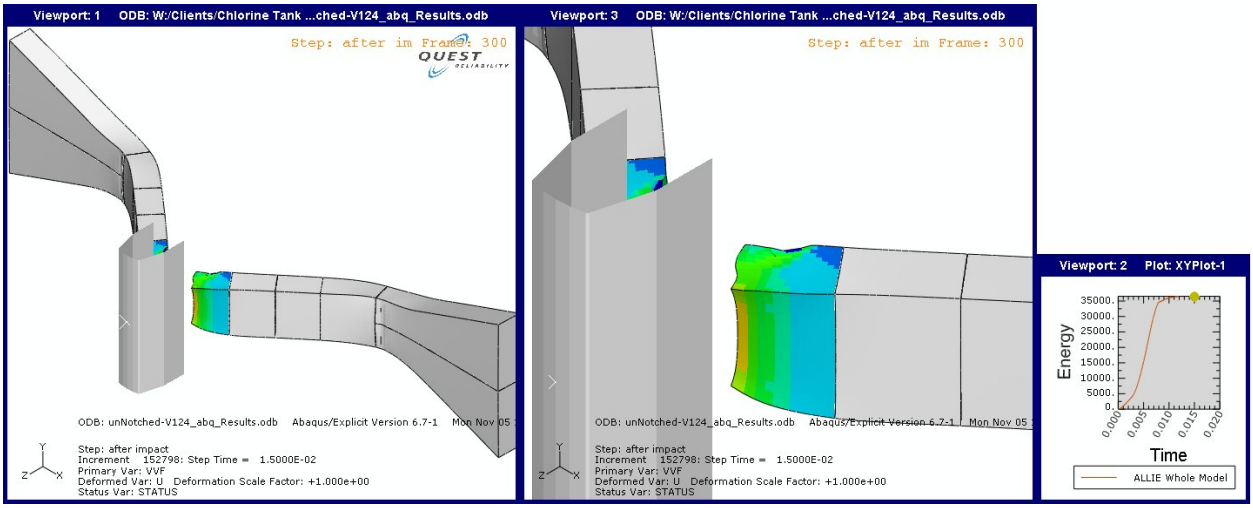

(g) time = 15 ms

FIGURE 3.5 (cont.) Typical results from a simulation of a BFCM test (end plates, platens & grips not shown).

TABLE 3.1

Comparison of experimentally-determined fracture energies for the BFCM specimens with finite element predictions. The gaps between the fixture and specimen, as well as friction effects, were neglected in the results tabulated below.

Material	Specimen Thickness, in	Charpy Energy, ft-lb	BFCM Energy, ft-lb		
			Experiment	Simulation	Sim./Exp. Ratio
TC 128B Sample C	0.822	89	7002	5098	73%
	0.624	89	4277	3804	89%
	0.502	89	3170	3005	95%
	0.370	89	2303	2058	89%
	0.251	89	1430	1410	99%
TC 128B Sample D	0.689	90	4993	4226	85%
A 710	0.777	170	6149	5925	96%
HPS 70	0.777	62	5938	4611*	78%
HPS100	0.777	170	7192	7190	100%

*Strain rate effects on tensile properties were truncated at 10 s^{-1}.

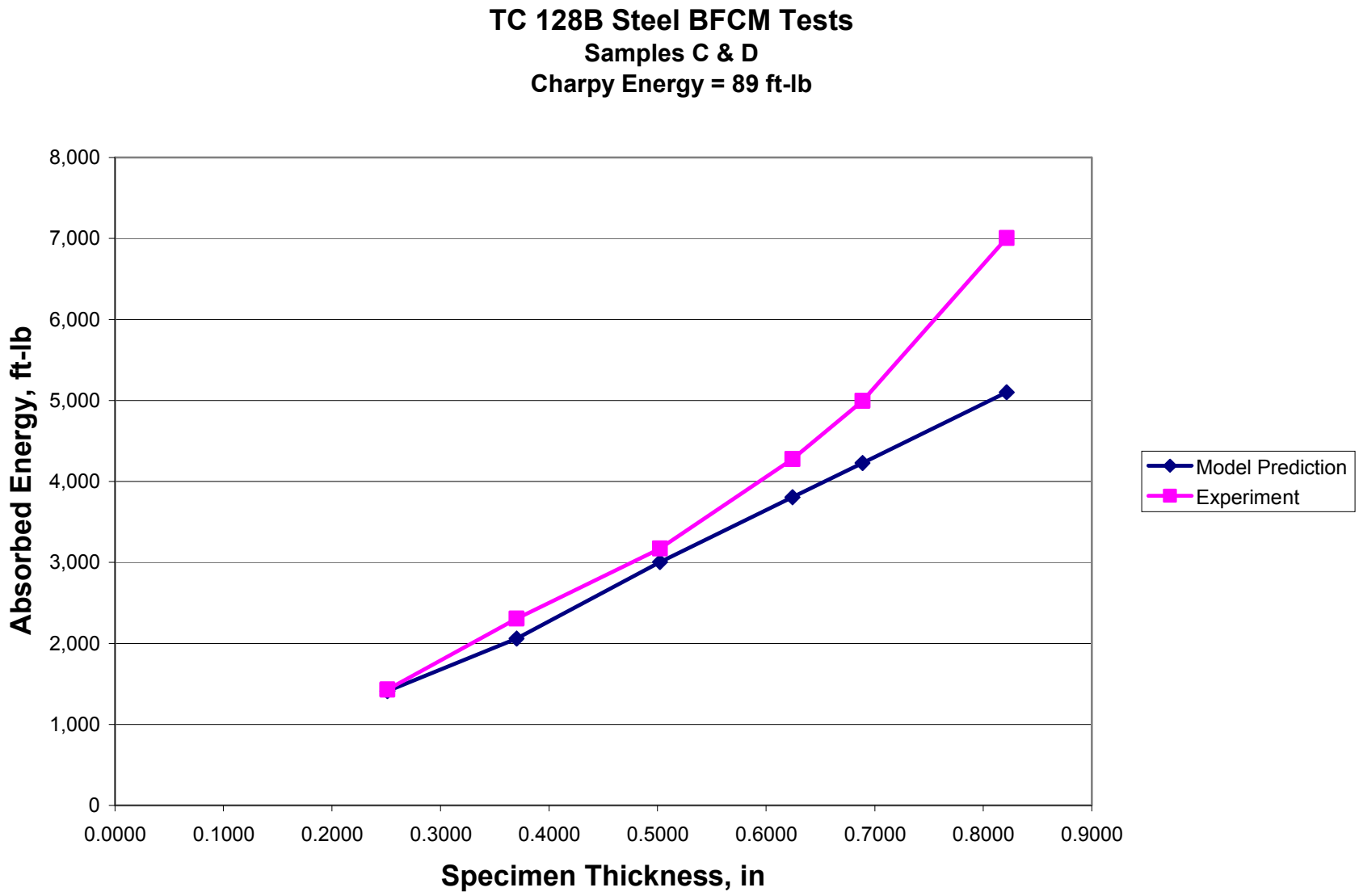

FIGURE 3.6 Effect of specimen thickness on BFCM absorbed energy for both the experiments and finite element simulations. Data for both Plates C and D are included in this plot.

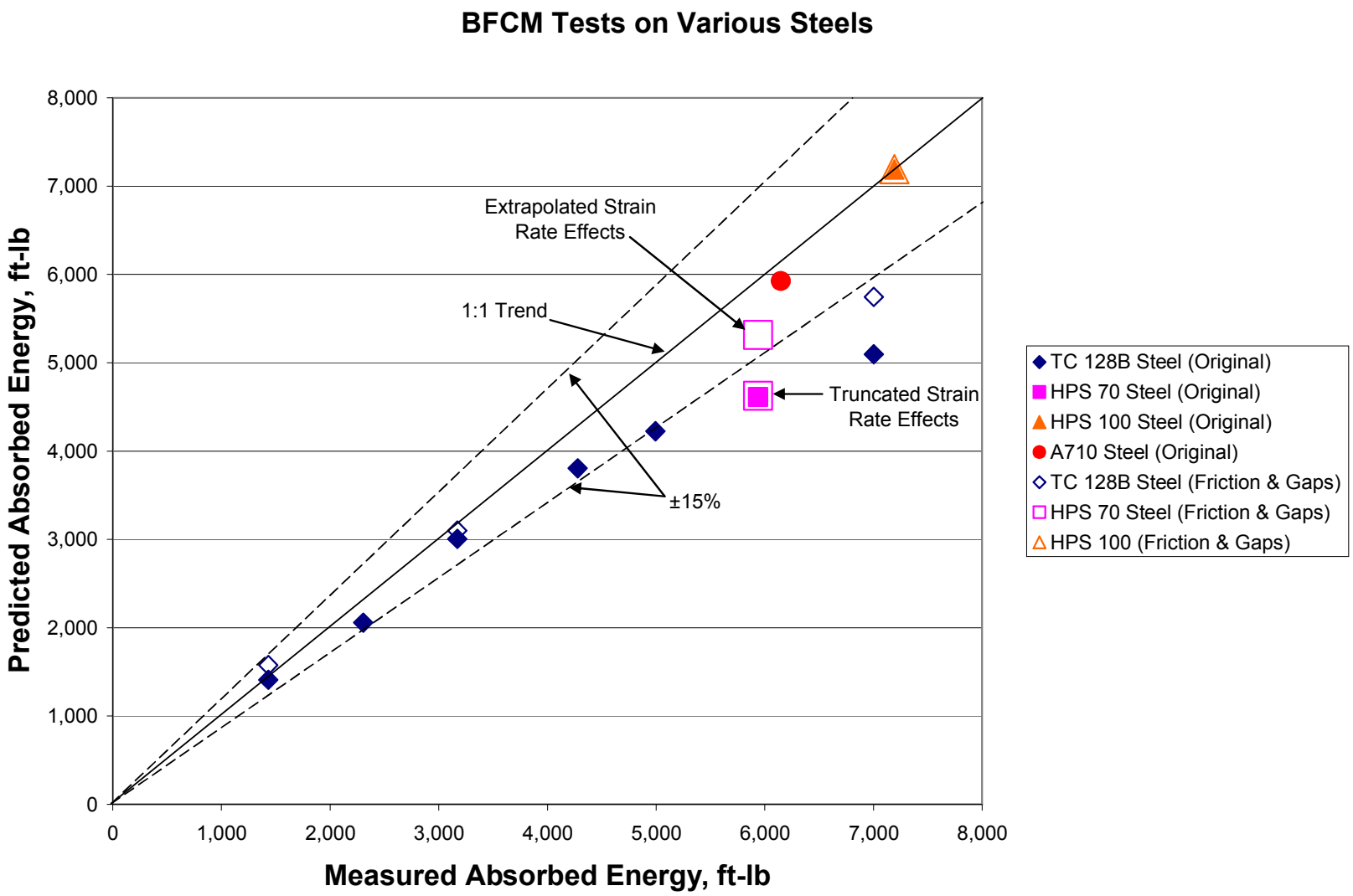

FIGURE 3.7 Predicted versus experimental absorbed energy in the BCFM tests.

3.4 Large-Scale Calibration Specimens

Given existing computational resources, it was not practical to perform full-scale tank car puncture simulations with 1 mm^3 elements in the target zone. We chose to increase the element length and width to 5 mm while maintaining the through-thickness mesh refinement. Thus the element dimensions for the most of the tank car simulations were 5 mm x 5 mm x ~ 1 mm.[1] As was the case for the BFCM simulations, the element thickness dimension was adjusted slightly from 1 mm so that the overall model conformed exactly to the desired section thickness.

As discussed earlier, the Gurson-Tvergaard ductile fracture model must be re-calibrated when the element dimensions change. In this case, however, it is not possible to calibrate using Charpy specimens, since their cross section is only 10 mm x 10 mm. Even the BFCM specimens are not suitable to calibrate a mesh with 5 mm x 5 mm elements because the striker would be less than three elements wide.

We chose to re-calibrate the material model with a simulation of puncture in a flat plate. The plate dimensions were chosen to induce a tension dominated failure in the plate, to match the expected failure mode in a tank car collision. Figure 3.8 shows the model used for this exercise. Note that the model is ¼ - symmetric. A 6-inch x 6-inch square striker (or 3" x 3" in the ¼ - symmetric model) with a 0.5-inch chamfer radius was impacted into the plate, and the resulting puncture energy was computed. This striker configuration is identical to that used in the tank car puncture simulations (Sections 4 and 5), so this simulation is representative of the tank car configuration, but with a much smaller model. The plate puncture is simulated with 1 mm x 1 mm elements, and then repeated with 5 mm x 5 mm elements. One or more parameters in the material model can then be adjusted in the coarser mesh so that the two meshes give the same puncture energy. Figure 3.9 shows the results of a typical plate puncture simulation.
As a check on the material model re-calibration, a second configuration was analyzed. Figure 3.10 shows the notched tension configuration that was used for this purpose. As was the case with the plate puncture simulation (Figs. 3.8 and 3.9), this configuration was analyzed with both 1 mm x 1mm and 5 mm x 5 mm elements in the fracture zone in order to adjust the material model for the coarser mesh. Figure 3.11 shows the results from a typical simulation of the notched tension configuration.

Figure 3.12 illustrates a typical re-calibration to a coarser mesh. In this example, we wish to model TC 128B steel with 50 ft-lb Charpy energy. The corresponding initial porosity, f_o, for 1 mm^3 elements be inferred from Fig. 3.2. The plate model is simulated with 1 mm^3 elements to obtain puncture energy, which in this case is 13,955 ft-lb. A second mesh with 5 mm x 5 mm x 1 mm elements is analyzed with a range of f_o values. The f_o value need to match the 13,955 ft-lb puncture energy is obtained by interpolation.

Ideally, the f_o values inferred from the plate puncture and notched tension configurations should be identical. In reality, they typically differ by a few percent. Reasonably close agreement between the two f_o estimates provides confidence that the material model is insensitive to the geometry of the component or specimen being analyzed. The f_o values used in the tank car impact simulations (Sections 4 and 5) were obtained by averaging the f_o estimates inferred from the plate and notched tension configurations.

[1] Some early tank car simulations used 2.5 mm x 2.5 mm x ~1 mm elements, but computation times were excessive.

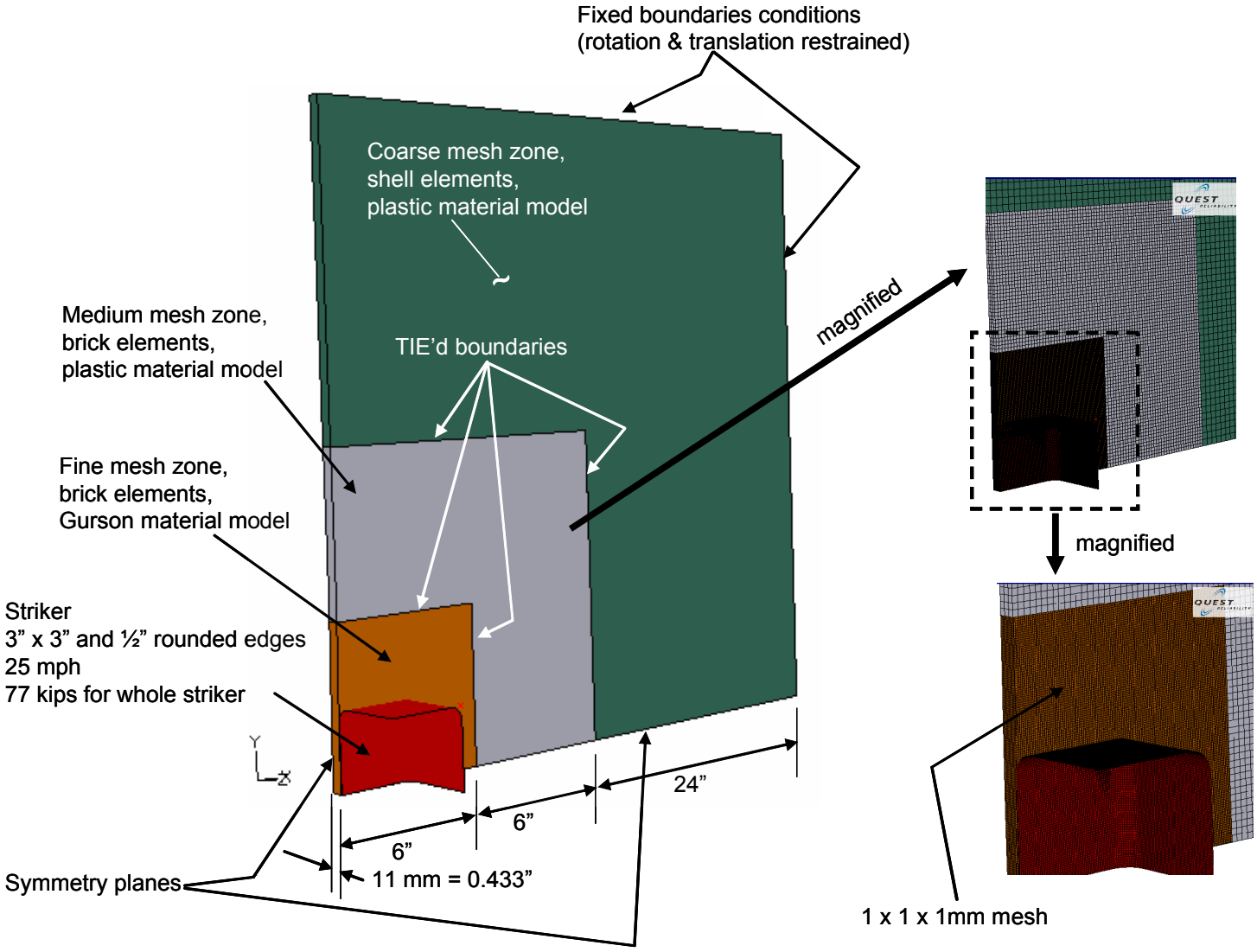

FIGURE 3.8 Flat plate impact specimen for calibrating the material model for various element sizes.

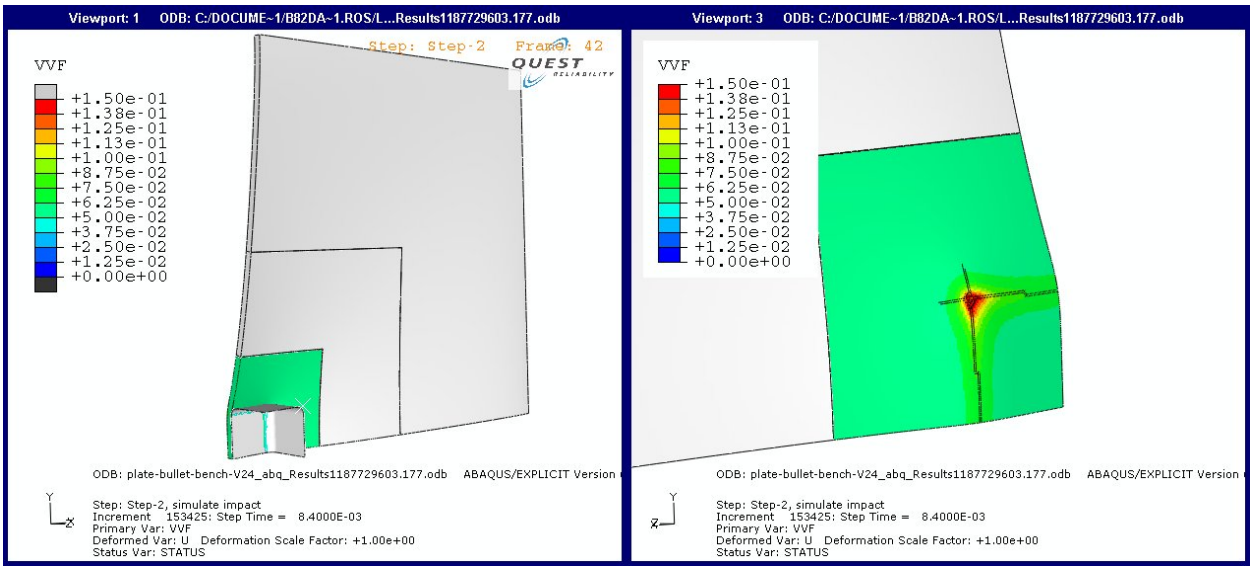

(a) Time = 8.4 ms

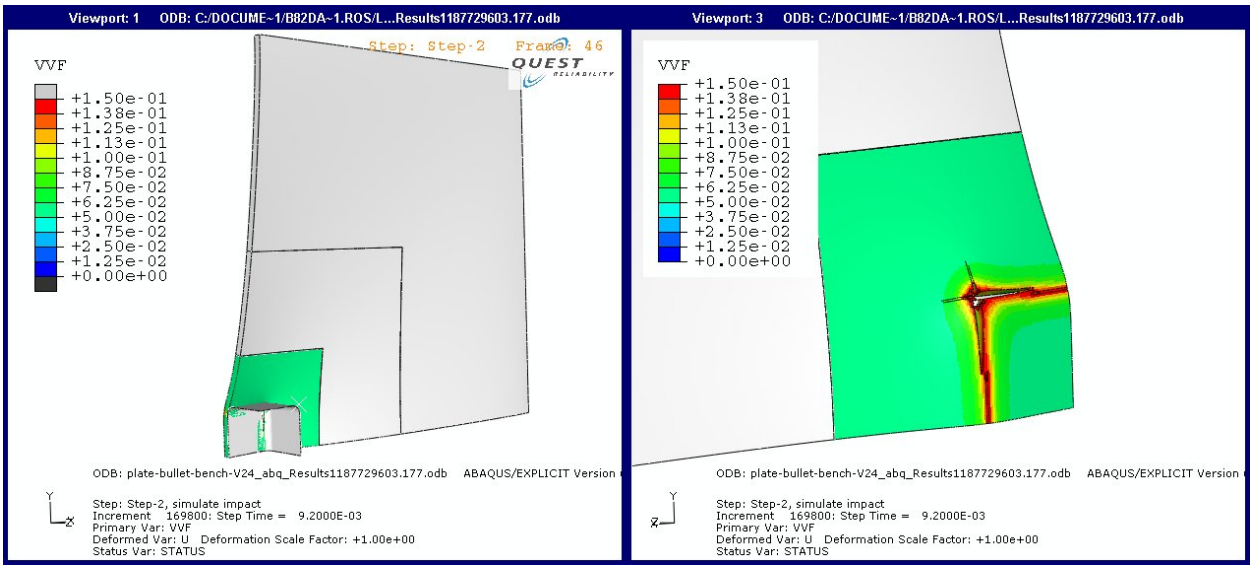

(b) Time = 9.2 ms

FIGURE 3.9 Typical results of the plate puncture simulation.

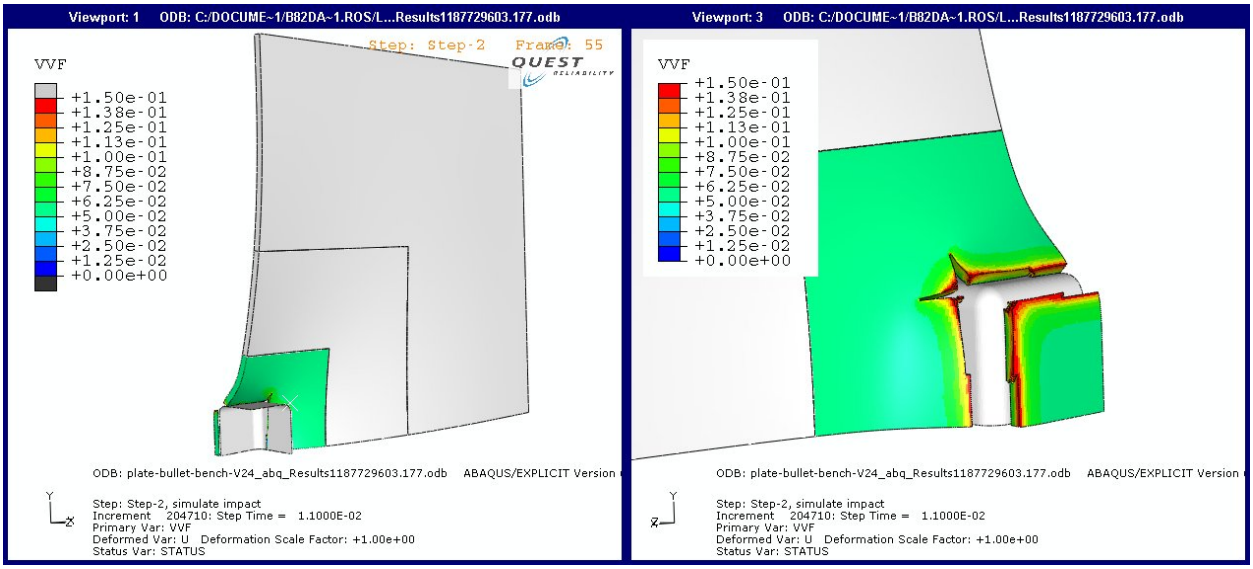

(c) Time = 11.0 ms

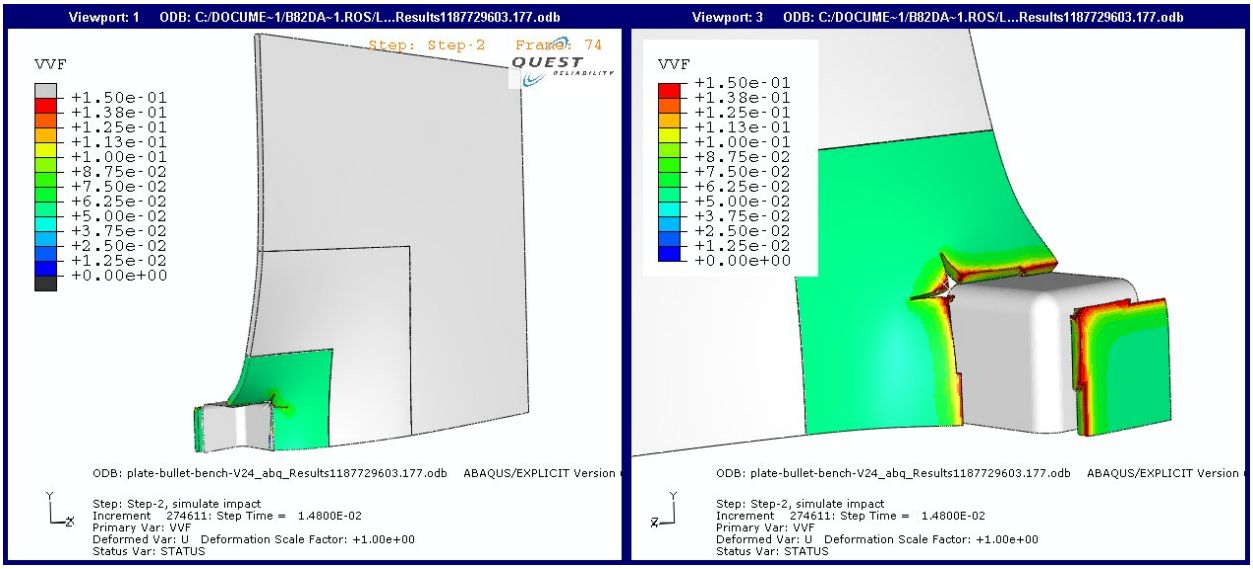

(d) Time = 14.8 ms

FIGURE 3.9 (Cont.)

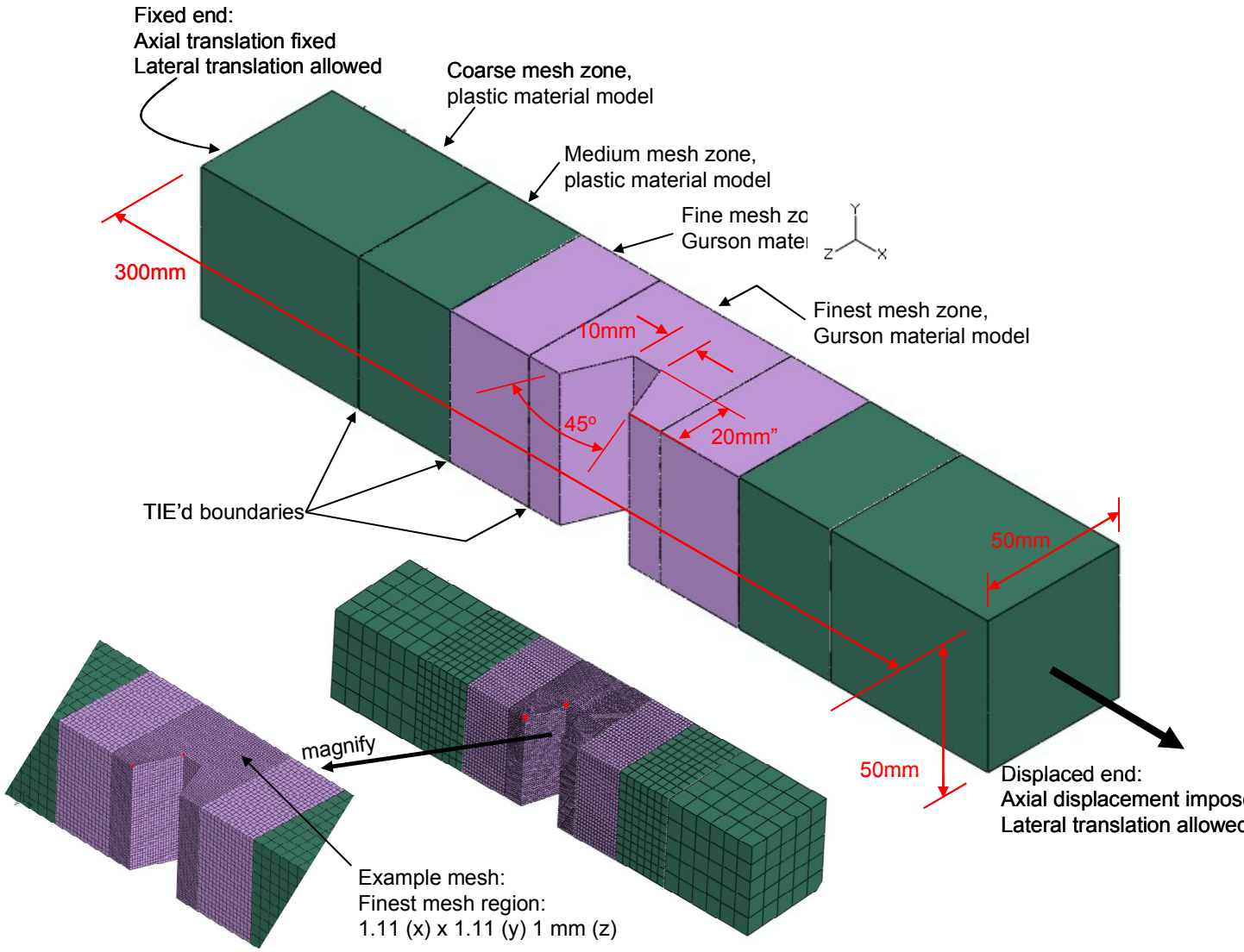

FIGURE 3.10 Finite element model for notched tension specimens

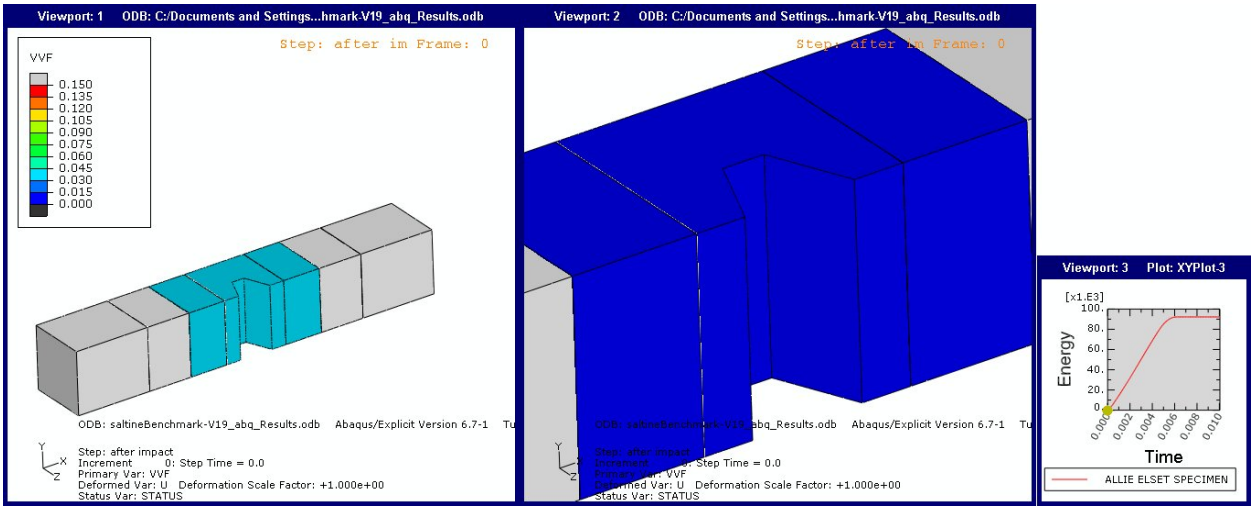

(a) Time = 0.0 ms

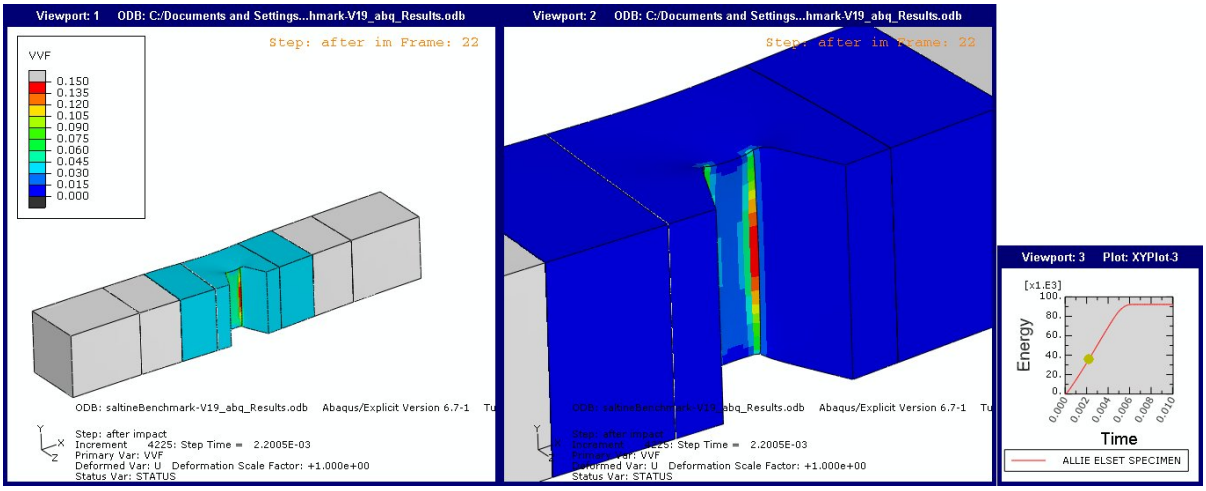

(b) Time = 2.2 ms

FIGURE 3.11 Typical fracture simulation in the notched tension configuration.

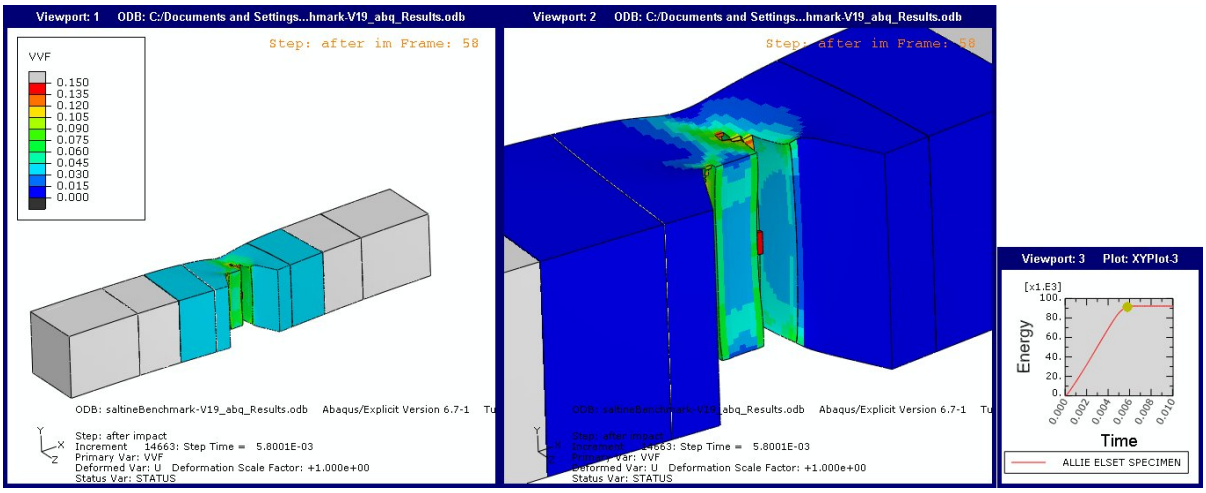

(c) Time = 5.8 ms

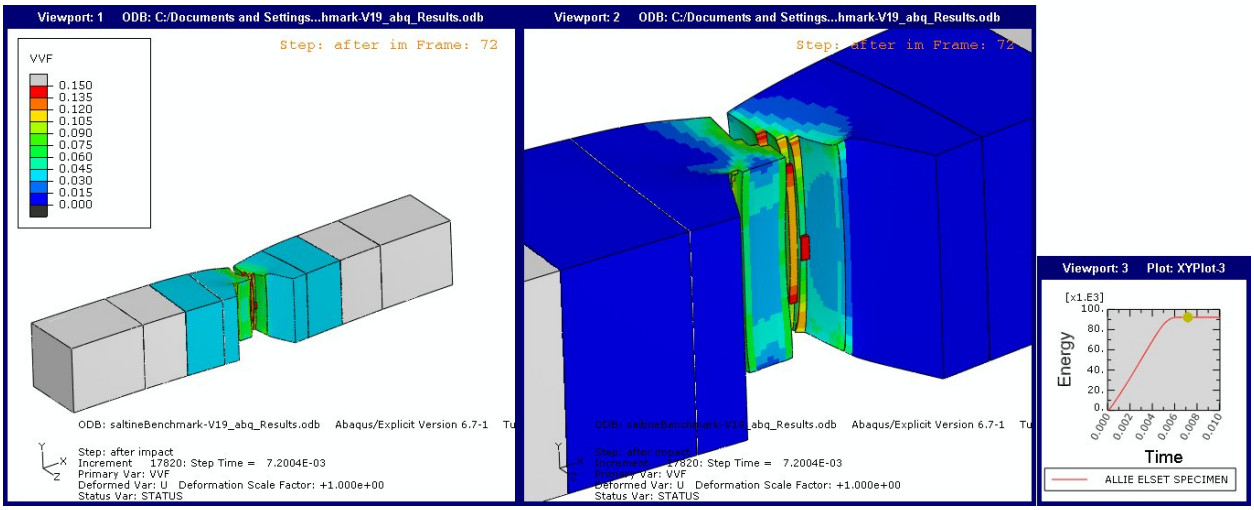

(d) Time = 7.2 ms

FIGURE 3.11 (Cont.)

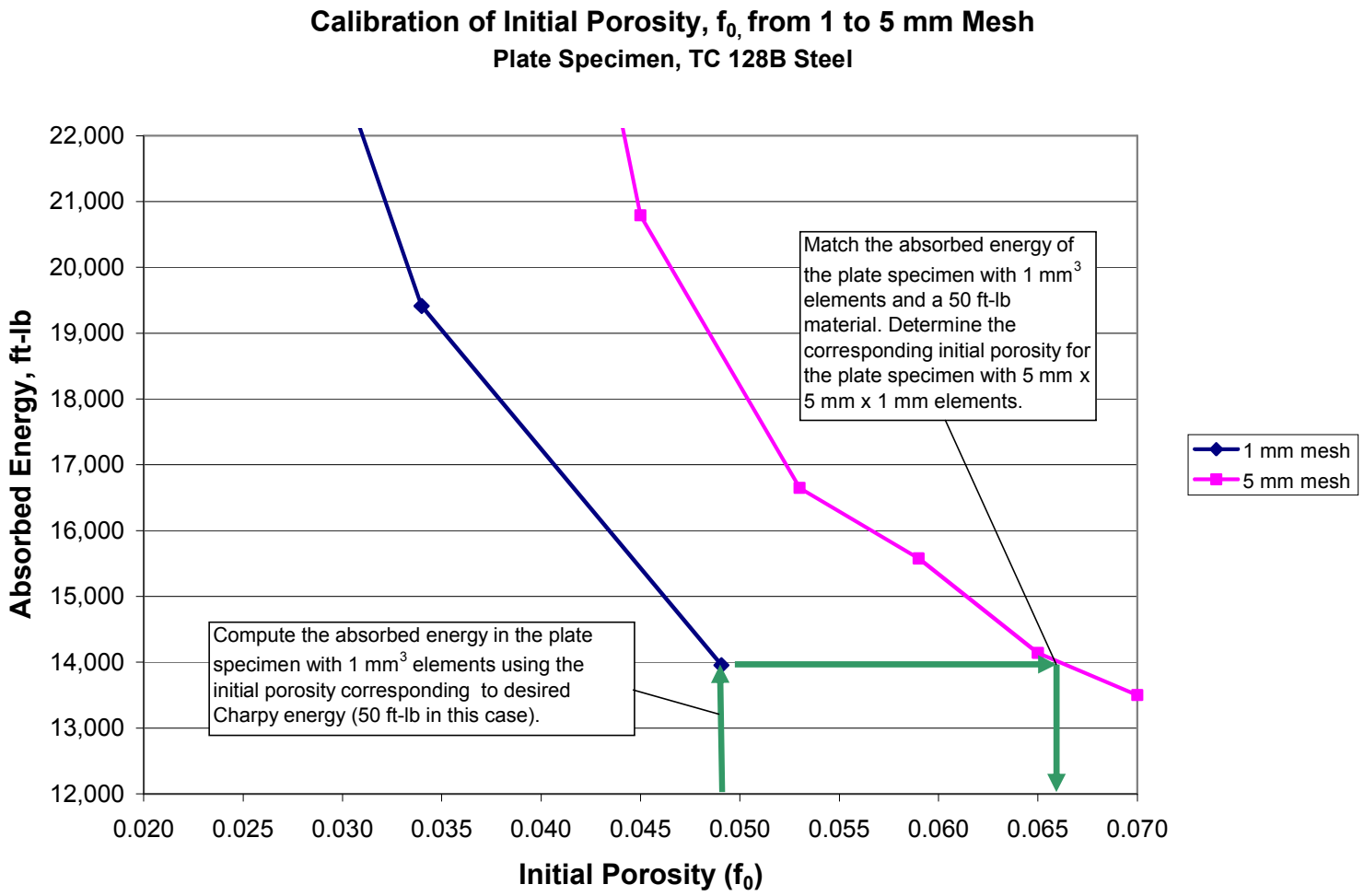

FIGURE 3.12 Calibration of material model for different element sizes. The initial porosity, f_o, is adjusted to give the same absorbed energy in the two meshes.

4 TANK CAR IMPACT SIMULATION PROCEDURES

This chapter describes the finite element models and modeling techniques for tank car simulations. The objective of the tank car simulations is determining energy absorbed by the tank car during an impact event. Absorbed energy values are subsequently used to determine sensitivity to various design and simulation parameters.

The base tank car configurations included in this study are listed in Table 4.1. The base configurations were modified to add or remove jackets and/or head shields as appropriate to quantify the relative effect of these design features.

A total of 6 collision scenarios were considered for each base tank car specification, as outlined in Table 4.2. In addition, a series of parametric analyses were performed to determine the effect of variables such as internal pressure, striker size, initial impact speed, friction, lading mass, and material toughness.

Table 4.1 Tank car configurations included in the finite element simulation study.

Car Specification	Shell Thickness, in	Head Thickness, in	Inside Diameter, in	Head-to-Head Length, in	Design Pressure, psi	Assumed Operating Pressure, psi*
111A100W	0.4375	0.4688	119.2	648	-	55
105J300W	0.5625	0.603	117.9	568	300	71
105J500W	0.777	0.8281	100.6	524	500	115
105J600W	0.981	1.136	106.0	494	600	138

*Based on typical operating pressures, but adjusted to maintain a constant hoop stress in all four tank car sizes.

Table 4.2
Collision scenarios considered in the present study

Impact Location	Tank Car Configuration
Shell	Bare shell (no jacket)
	0.112-inch thick jacket
Head	Bare head (no jacket or head shield)
	0.112-inch thick jacket
	0.500-inch thick head shield without standoff
	0.500-inch thick head shield with standoff (jacketed car)

For the shell impact scenario, the striker impacts the tank car at mid-span and half height with the striker traveling laterally with respect to the tank car as shown in Fig. 4.1. For a head impact, the striker impacts the tank car at the center of the head with the striker traveling longitudinal

with respect to the tank car axis, as shown in Fig. 4.2. For computational efficiency, only ¼ of the tank car was modeled, as illustrated in Figs. 4.1 and 4.2.

For most simulations, a striker weight 280,000 lb and an initial striker velocity of 40 mph were assumed. Higher initial velocity simulation results in impact events of shorter duration, which translates to shorter computation times. The initial impact velocity was varied in a limited number of simulations to demonstrate its effect on puncture energy.

Figures 4.3 and 4.4 compare finite element models with and without head shields and jackets. In all models, the tank car abuts a reaction wall as shown in Figs. 4.1 to 4.7 The reaction walls are idealized as rigid, frictionless surfaces.

Figures 4.6 and 4.7 show the mesh configuration for shell and head impacts of an unjacketed car. The mesh is progressively refined, with the finest mesh adjacent to the striker. "Tied" interfaces connect the various mesh zones, in lieu of using a mesh size transition zone. The element size in the refined zone was either 5 x 5 x ~1mm or 2.5 x 2.5 x ~1 mm, as shown in Fig. 4.6. The ~1 mm dimension in the thickness direction assures that through thickness gradients of stress, strain, etc have adequate resolution. The early tank car models had a 2.5 mm refined zone mesh, but computation times were on the order of several days per simulation. The mesh size was increased to 5 mm x 5 mm x ~1 mm to reduce computation time to a reasonable level. Benchmarks were performed to ensure that the same results were achieved in both mesh configurations, provided the material model was properly calibrated to the corresponding mesh.

The refined and medium zone meshes contain first-order, reduced integration brick elements, while the remainder of the model contains continuum shell elements. Continuum shell elements resemble brick elements when viewed in a pre/postprocessor, but behave like shell elements located at the element mid-surface. Continuum shell elements efficiently capture plate-bending effects in areas away from the impact zone. Meshes for the five other combinations of tank car configuration and impact location are similar to the mesh for the broadside impact of an unjacketed car.

The symmetry boundaries are constrained with the appropriate boundary conditions. There are no additional boundary conditions applied to the model.

For jacketed configurations, the jacket is separated 4 in. from the shell by studs. The studs are idealized by a solid layer with an equivalent stiffness, as shown in Figs. 4.3 and 4.4. The equivalent stiffness of the solid layer is only 0.12% of the stiffness of steel. For shell impact, the insulation layer is located on the half of the model away from the impact zone, providing a means to transfer impact forces to the reaction wall. The remaining half of the model lacks an insulation layer, to ease model construction. Omission of the equivalent insulation layer from the impact side of the model will not affect the absorbed energy because the studs and insulation do not contribute significantly to the strength of the tank shell. Similarly, for head impacts, the head region lacks an equivalent insulation layer.

The interactions between the striker, tank shell, jacket and head shield are modeled with the penalty contact formulation. A few simulations incorporate friction and contact between the striker and fracture surfaces. However the majority of the simulations assume friction-less interaction.

A few simulations incorporate the effect of the lading mass. The mass of the lading is distributed to the shell wall by increasing the density of the shell wall.

Mass scaling of 6.25x is applied to the refined zone during the impact portion of the simulation, resulting in a modest decrease in computation time. Larger mass scaling has proven to degrade the accuracy of the solution. Portions of the model incorporating lading mass are not mass scaled.

The inner surface of the shell wall is pressurized as shown in Figures 4.5 and 4.7. Simple calculations showed that the volume of the tank does not decrease significantly during the impact event up to rupture, justifying the use of constant pressure during the impact event.

Accommodating both pressurization and impact events in one simulation requires a special technique. The explicit solution does not allow static analyses and therefore, the simulations capture tank vibrations caused by pressurization. This technique ensures that pressure induced vibrations are damped out before the impact event and damping is negligible during the impact event. Mass proportional damping eliminates unwanted vibrations and is described below:

$$\mathbf{C} = \alpha \cdot \mathbf{M} \tag{4.1}$$

where

$\mathbf{C}$ = the damping matrix,
$\mathbf{M}$ = the mass matrix, incorporating mass scaling,
α = mass proportional damping coefficient, on the order of 0.4.

To minimize vibrations, mass scaling is tuned to result in critical damping in the first mode of the tank. This requires a large amount of mass scaling and the resulting natural period is on the order of 500 seconds. The pressure is ramped up over a duration exceeding the natural period of the tank. The pressure is then held constant, allowing vibrations to dissipate. At the end of the hold period, mass scaling is reduced, thereby decreasing the damping ratio to a miniscule fraction of critical.

The energy absorbed during the impact event is calculated from velocities:

$$E = \tfrac{1}{2} m \left(V_i^2 - V_f^2 \right) \tag{4.2}$$

where

V_i = initial velocity of the striker,
V_f = final velocity of the striker,
m = mass of the striker.

This energy measure is convenient because it includes strain, kinetic, plastic deformation and rupture energies, as well as frictional dissipation. Energy at two occurrences are examined:

- First leak: when a rupture propagates through the entire thickness of the tank shell or head, allowing the lading to escape the tank
- Puncture: when the shell/head material at the impact zone completely separates from the remainder of shell/head.

Figures 4.8 through 4.14 show snapshots from a series of simulations for the size impact scenarios listed in Table 4.2. In each illustration, the left, middle and right frames show a view from the outside of tank, a view from the inside of tank and the striker velocity time history, respectively. The snapshots illustrate a sequence of bending of the tank wall, initiation of tank wall rupture, propagation of a rupture through the entire thickness resulting in a leak, and puncture (complete tear-through) of the steel in the impact zone.

Figure 4.15 is a plot of energy versus time for shell impact on a tank car with and without a jacket. The base car configuration for this example is 105J500W. The absorbed energy of the jacketed car is somewhat higher than for the unjacketed car, as one would expect. For the jacketed car, there is a brief period in which the absorbed energy increases only slightly immediately after impact. During this brief time window, the jacket bends inward and contacts the shell. Because the jacket has low stiffness, minimal energy is dissipated during this event. The energy increases more rapidly once the shell begins to bend inward.

Two points are labeled on each of the curves in Fig. 4.15: where initial leak would occur and where complete puncture occurs. These two events occur in rapid succession, as the simulation results in Figs. 4.8 to 4.14 indicate. Minimal energy is absorbed between the initial leak and complete puncture. Figure 4.16 is a plot of energy for leak and puncture as a function of shell thickness in jacketed and unjacketed cars.

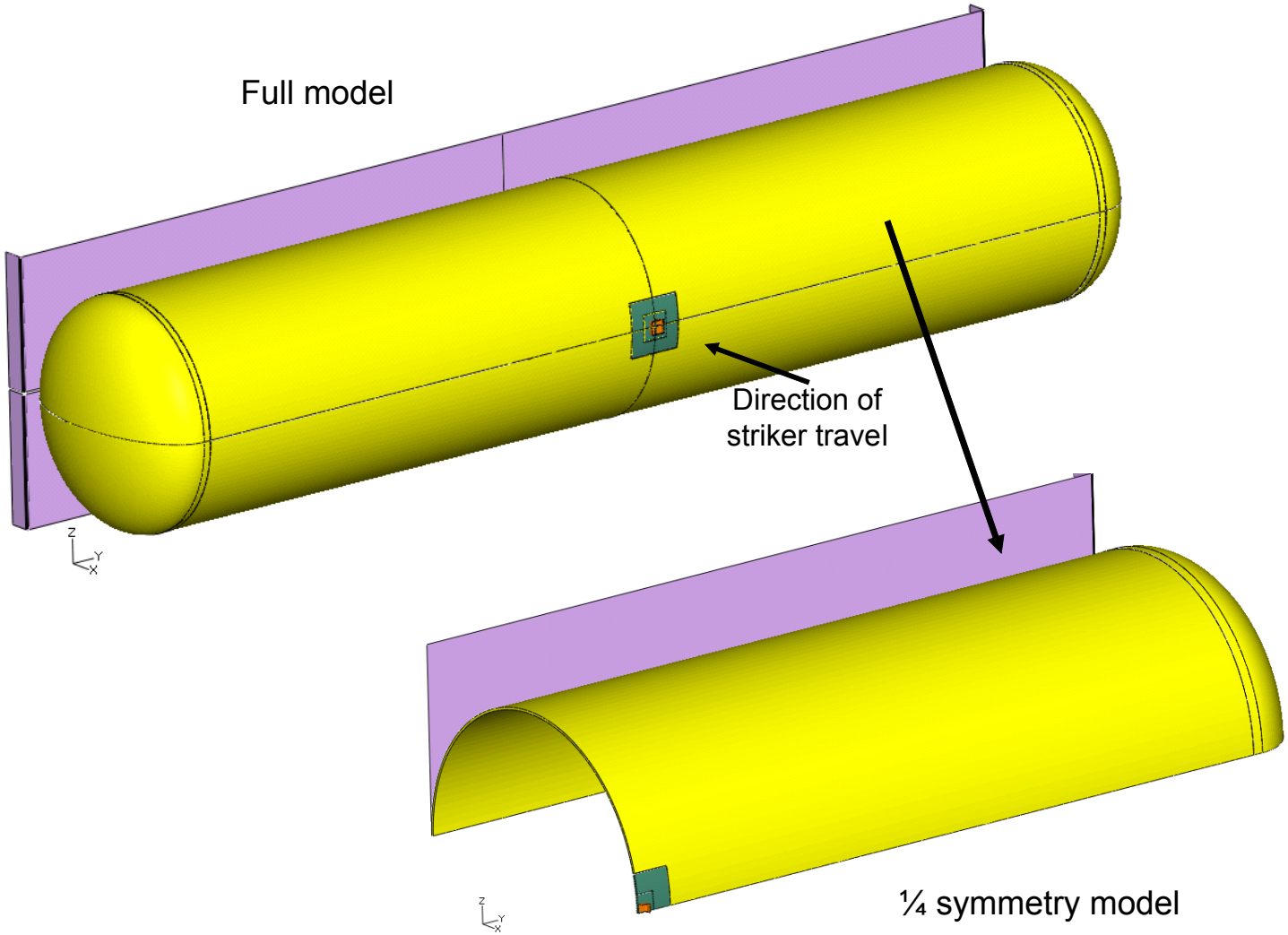

FIGURE 4.1 Typical tank car finite element model for shell impact.

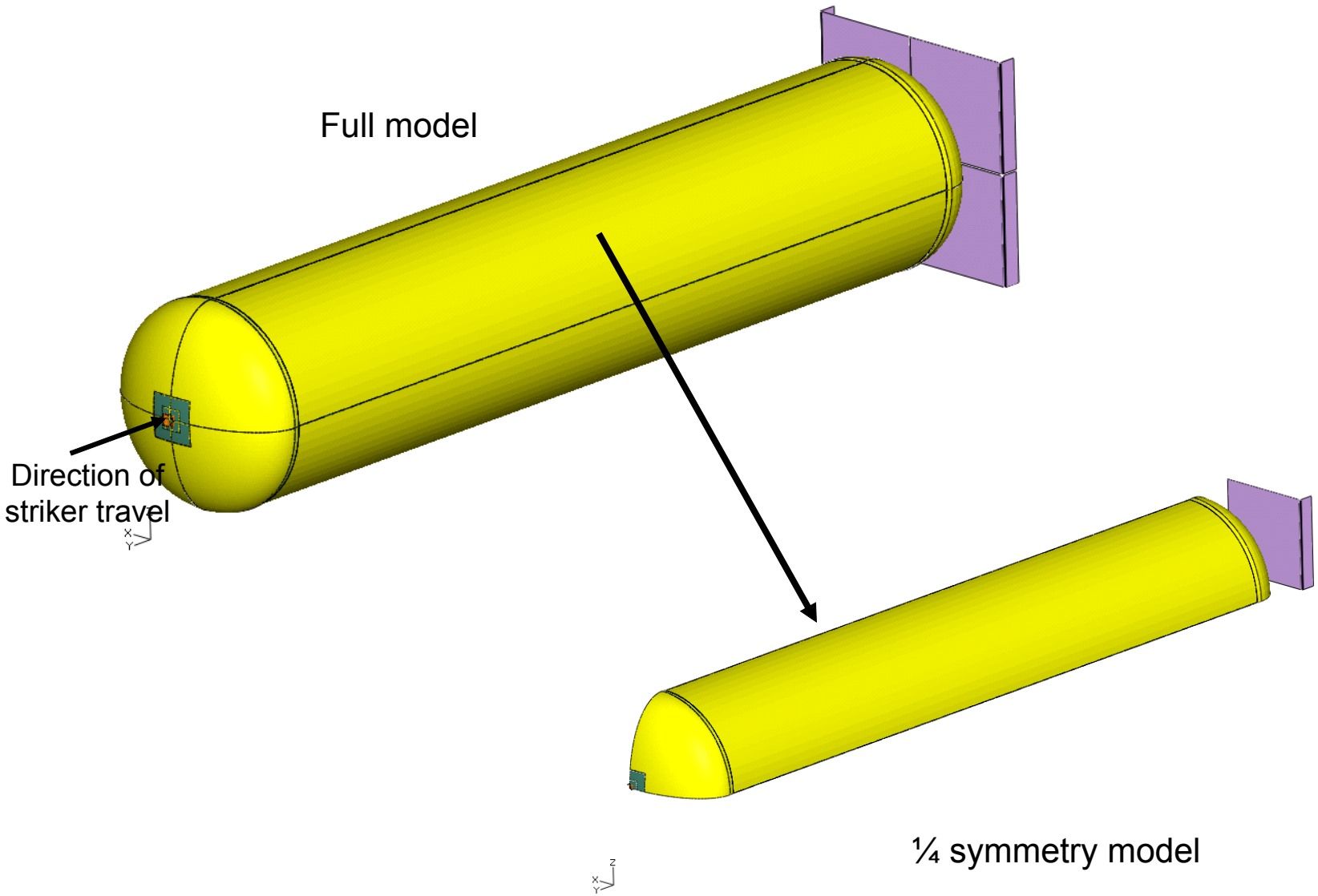

FIGURE 4.2 Typical tank car finite element model for head impact.

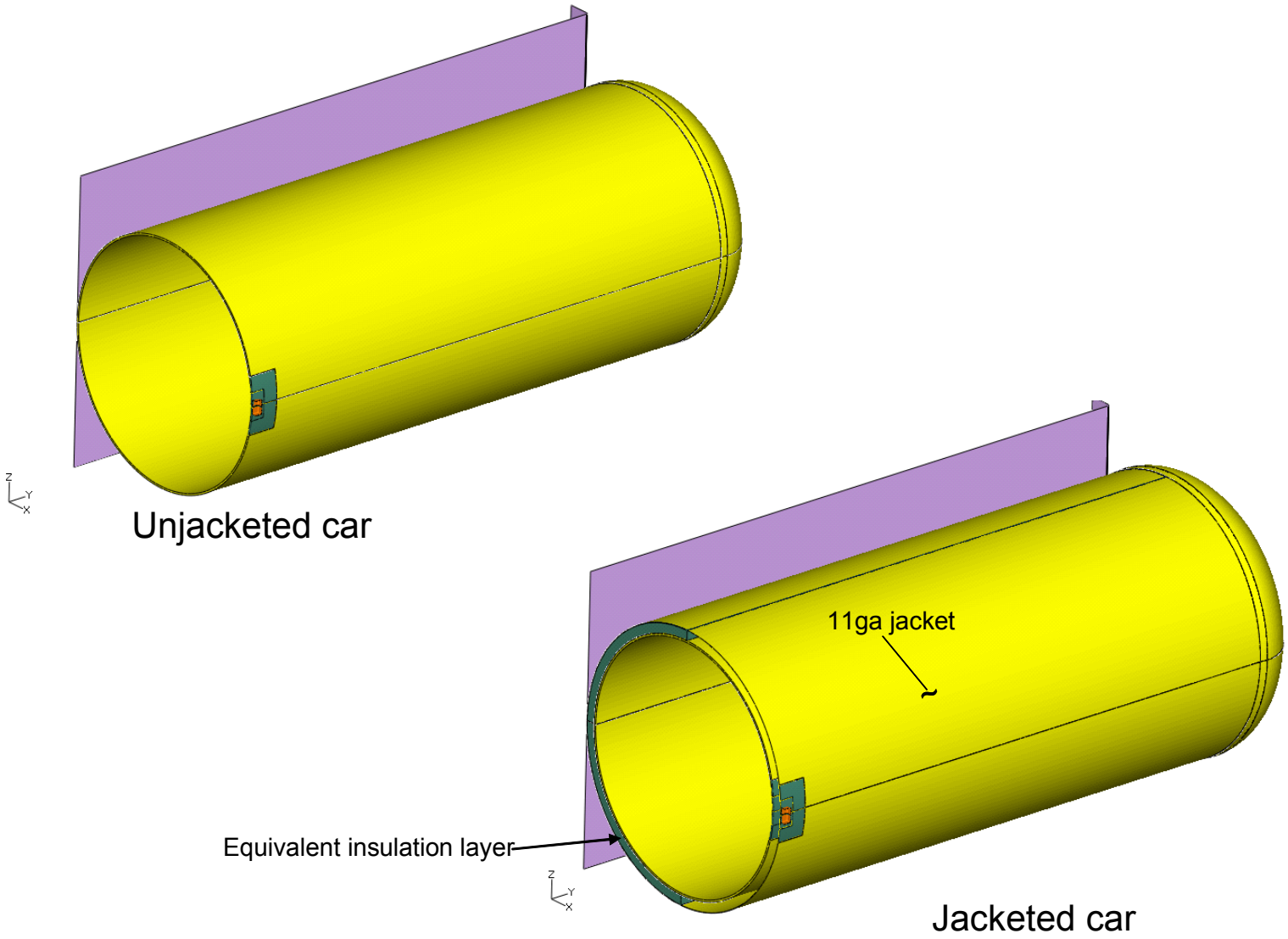

FIGURE 4.3 Finite element models of tank cars for shell impact, with and without a jacket.

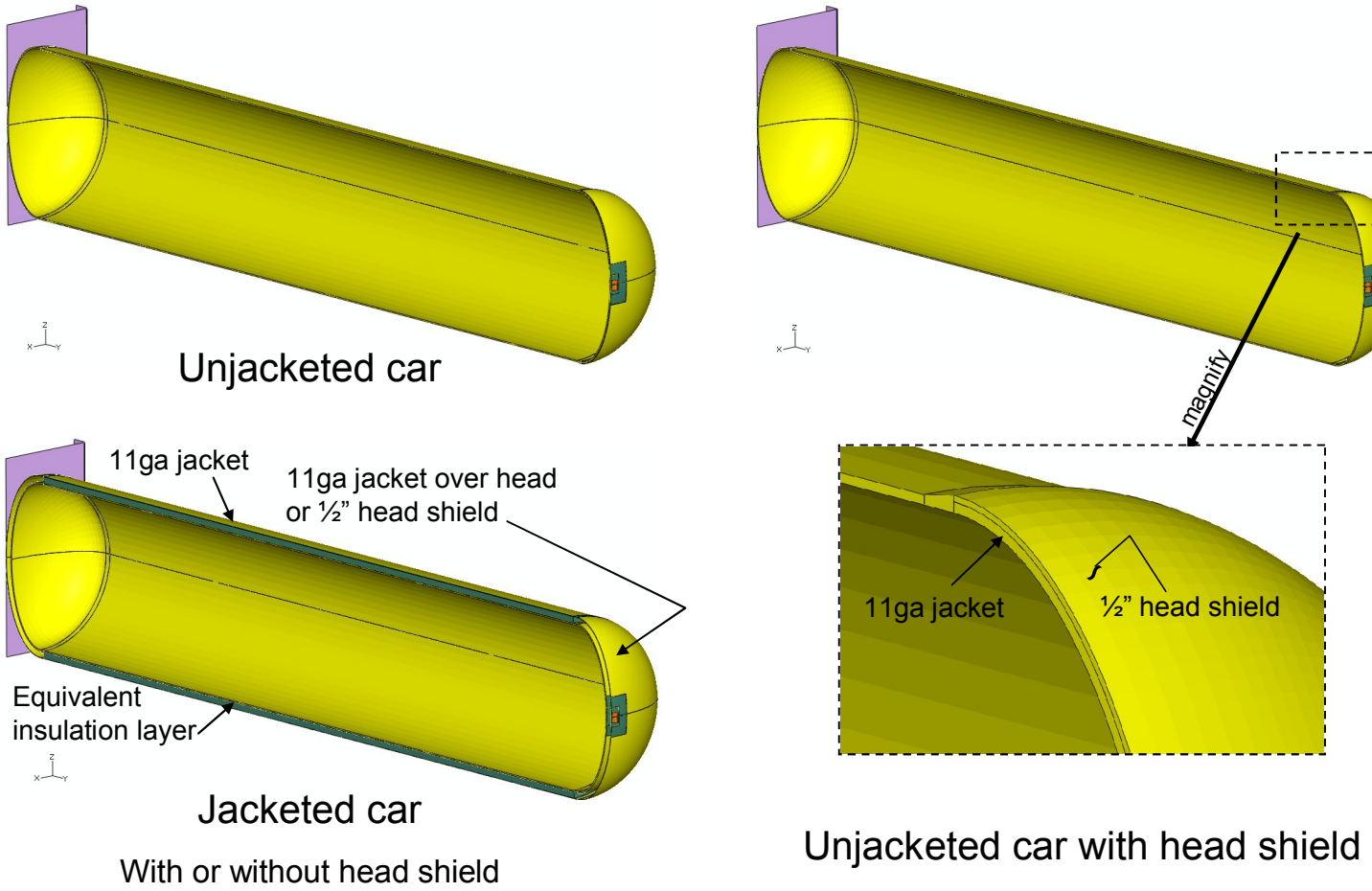

FIGURE 4.4 Finite element models for head impact, with and without a jacket or head shield.

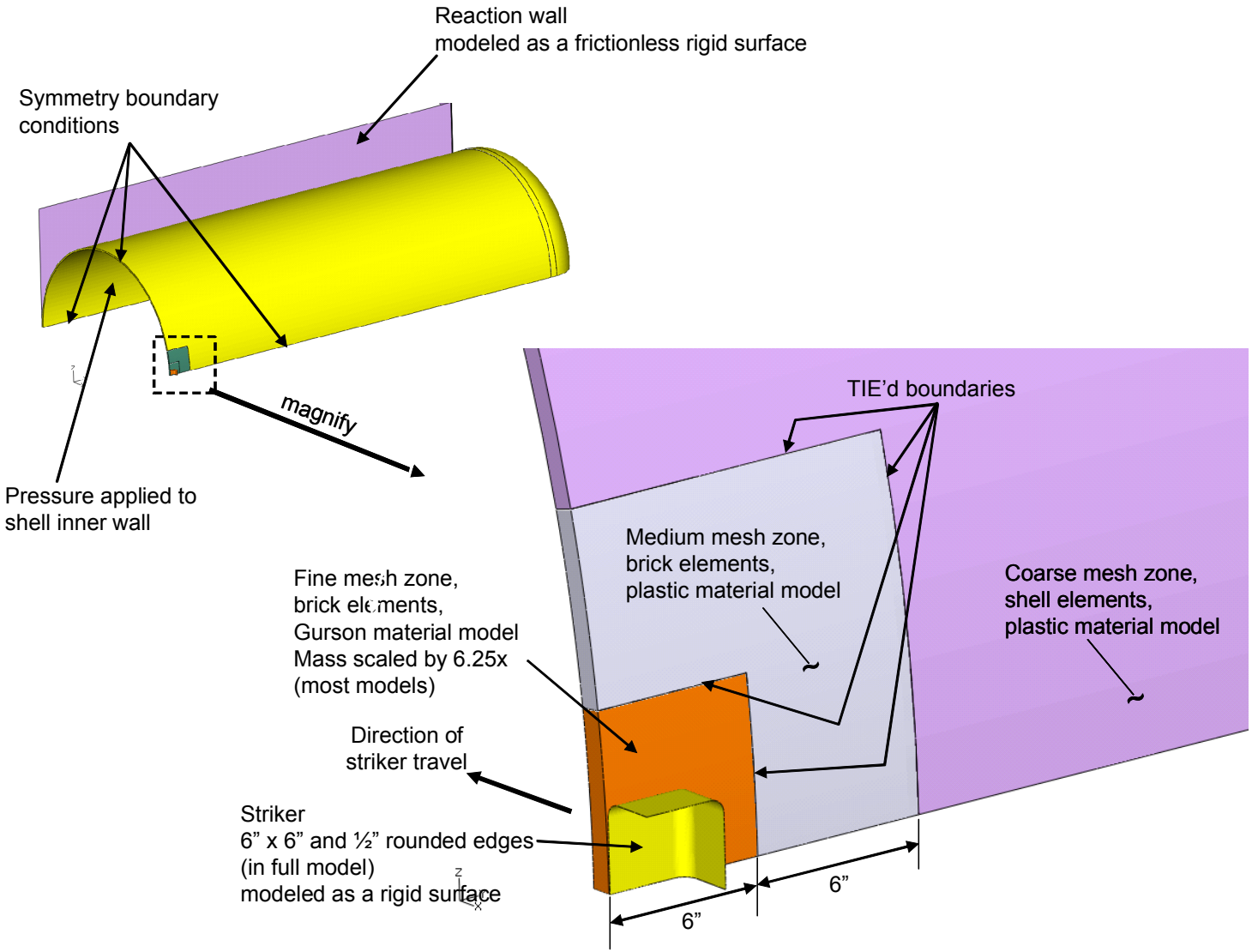

FIGURE 4.5 Details of a typical finite element model for shell impact.

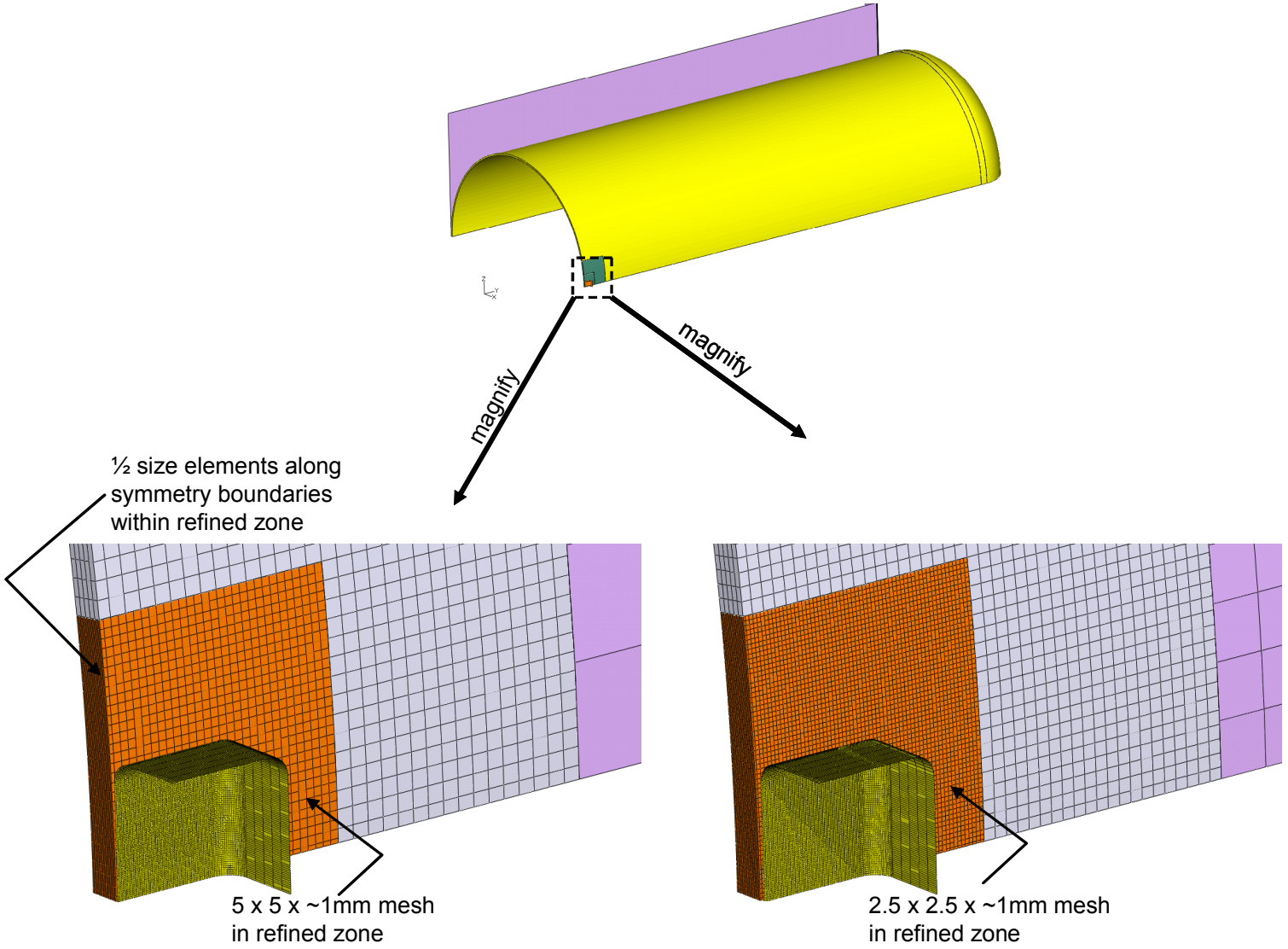

FIGURE 4.6 Typical finite element mesh for tank car subject to shell impact

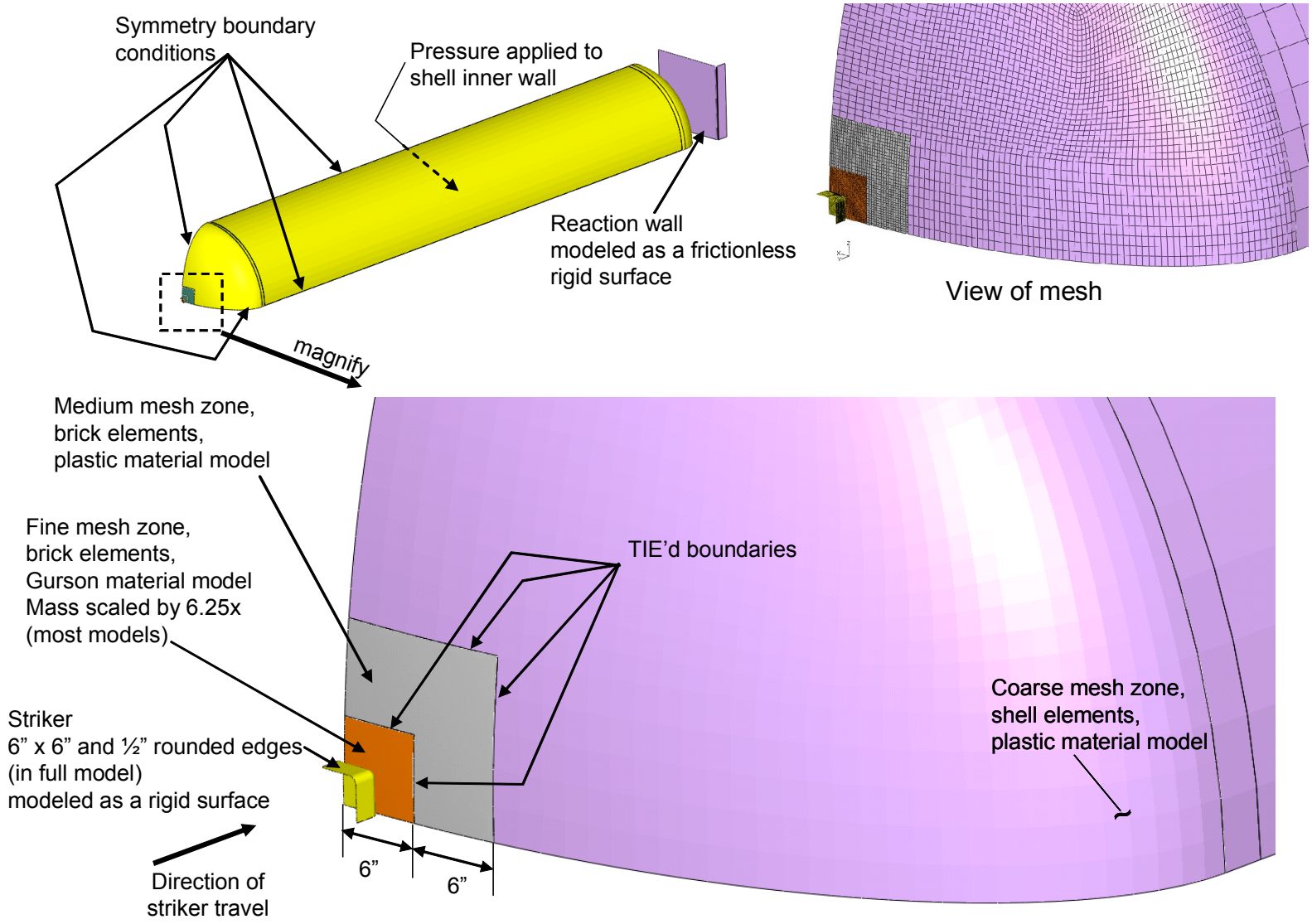

FIGURE 4.7 Details of a typical finite element model for head impact

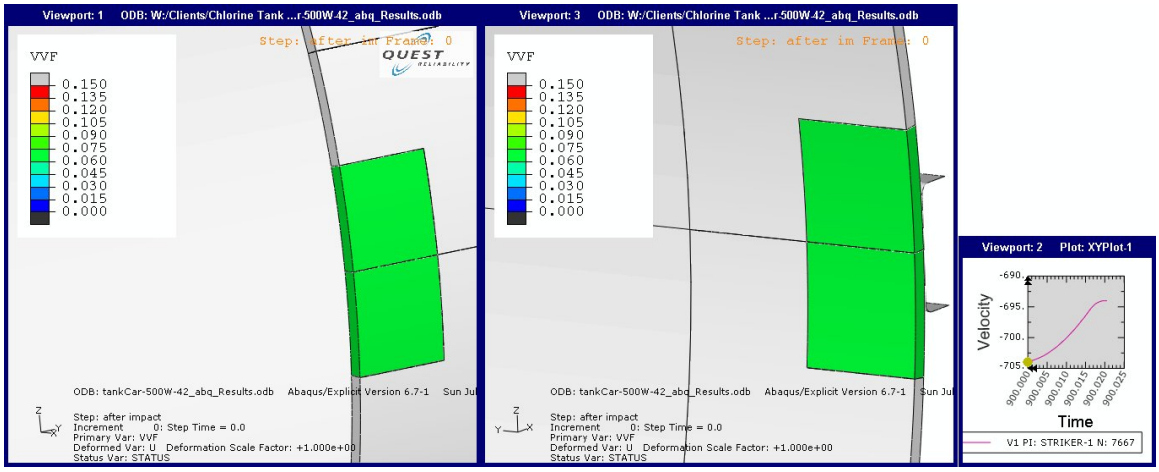

(a) Time = 0 ms

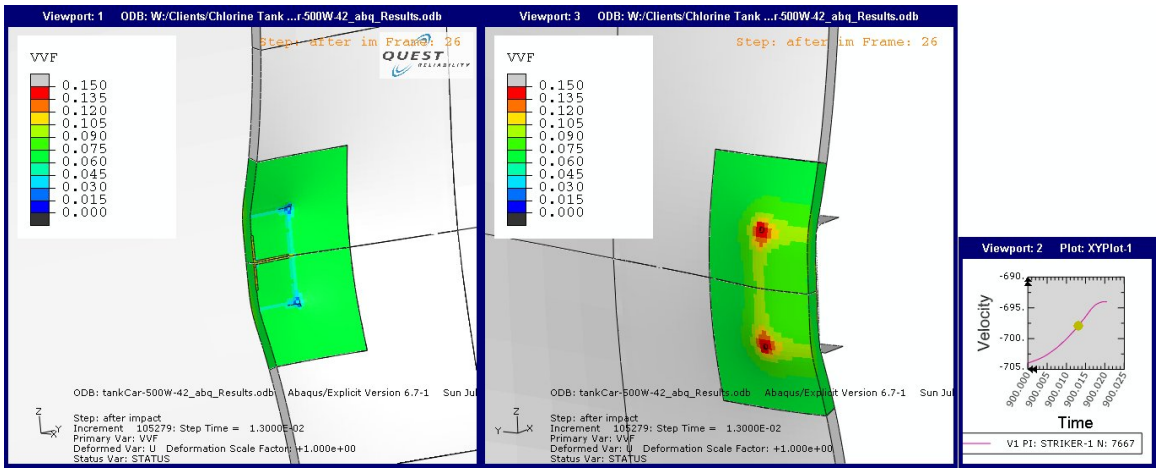

(b) Time = 13 ms

FIGURE 4.8 Typical simulation of a shell impact on an unjacketed car.

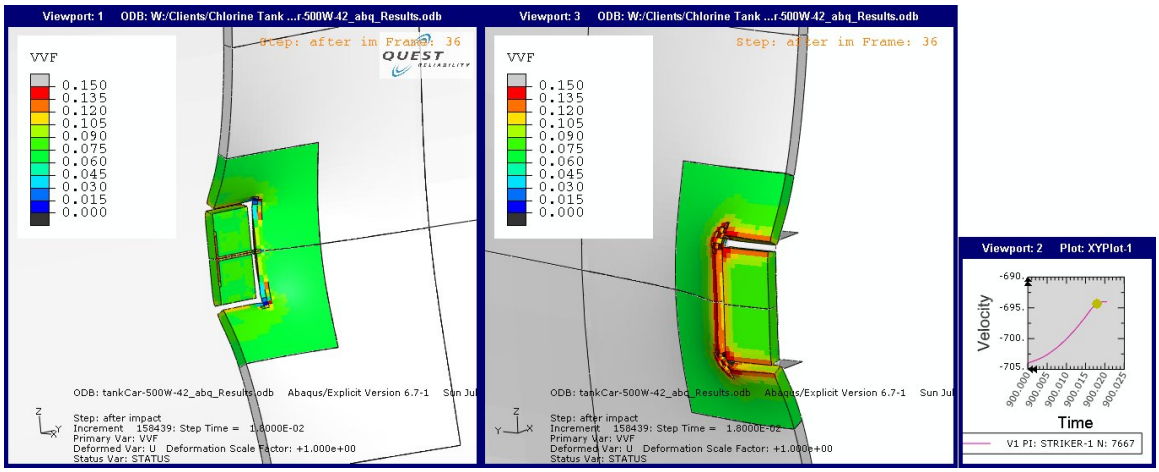

(c) Time = 18 ms

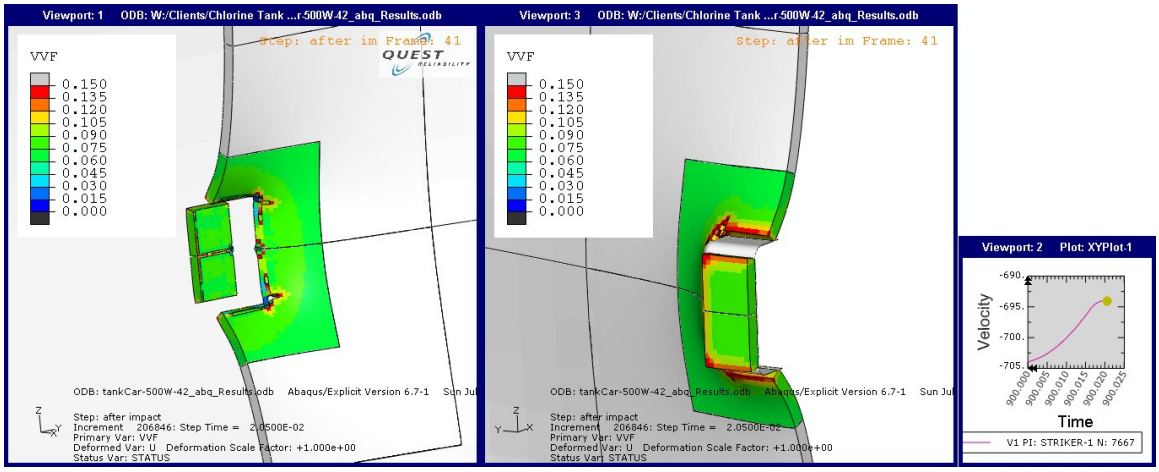

(d) Time = 20.5 ms

FIGURE 4.8 (Cont.)

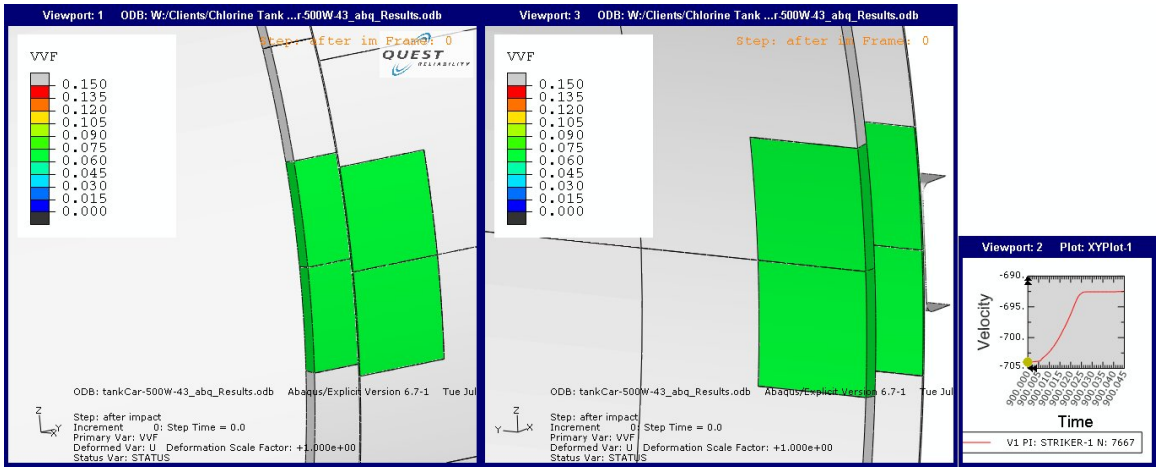

(a) Time = 0 ms

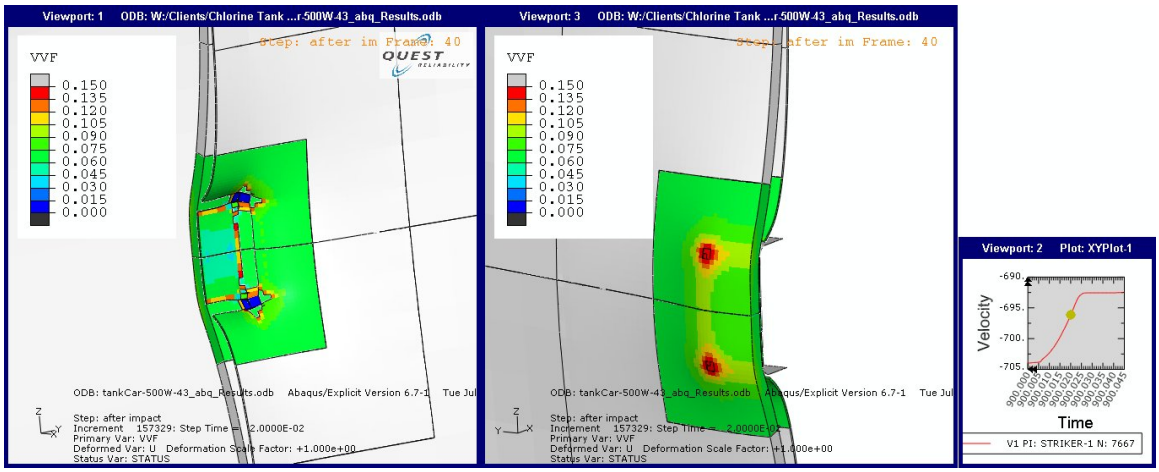

(b) Time = 20 ms

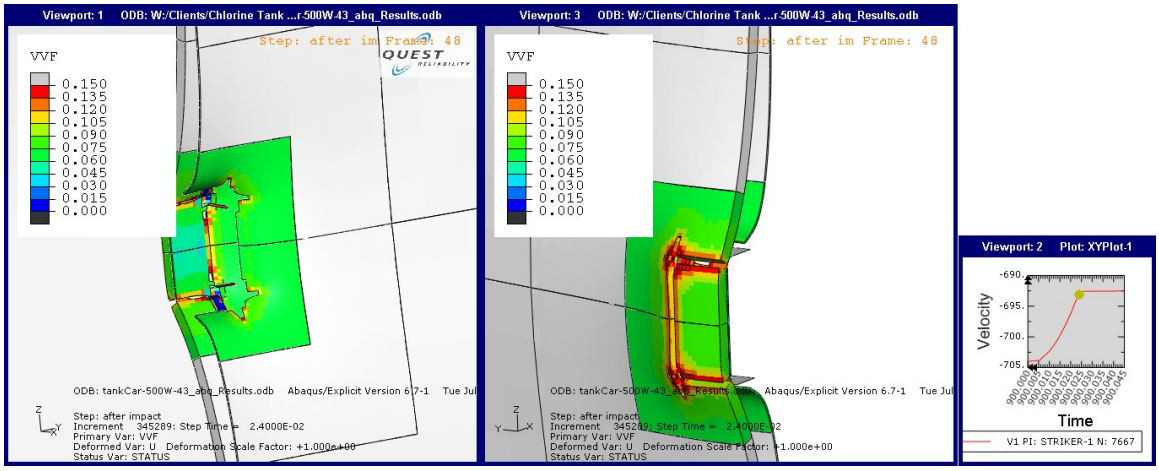

(c) Time = 24 ms

FIGURE 4.9 Typical simulation of a shell impact on a jacketed car.

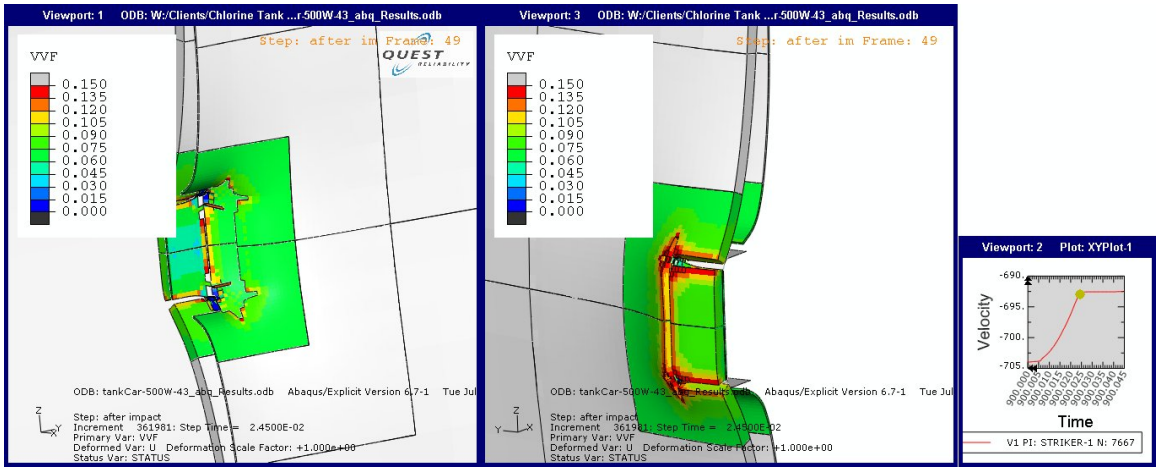

(d) Time = 24.5 ms

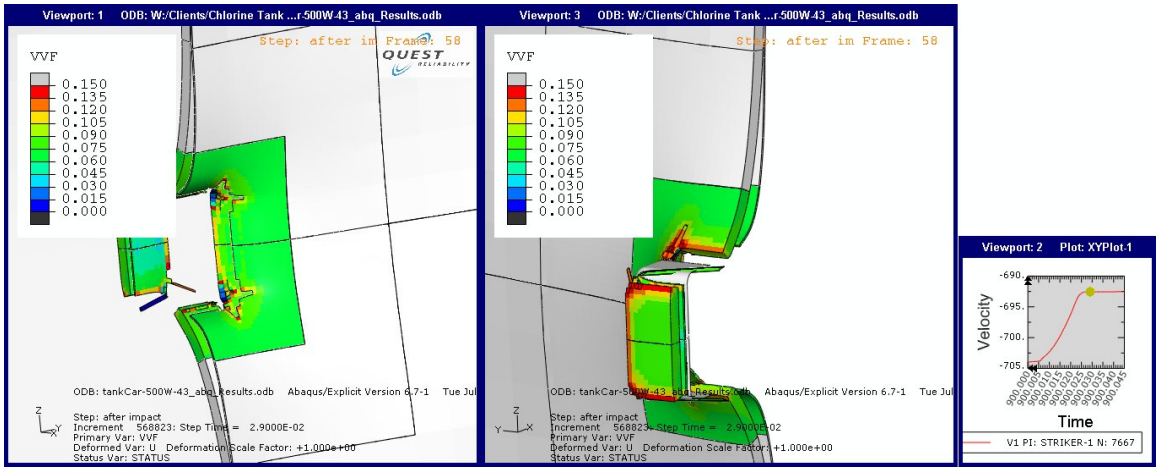

(e) Time = 29 ms

FIGURE 4.9 (Cont.)

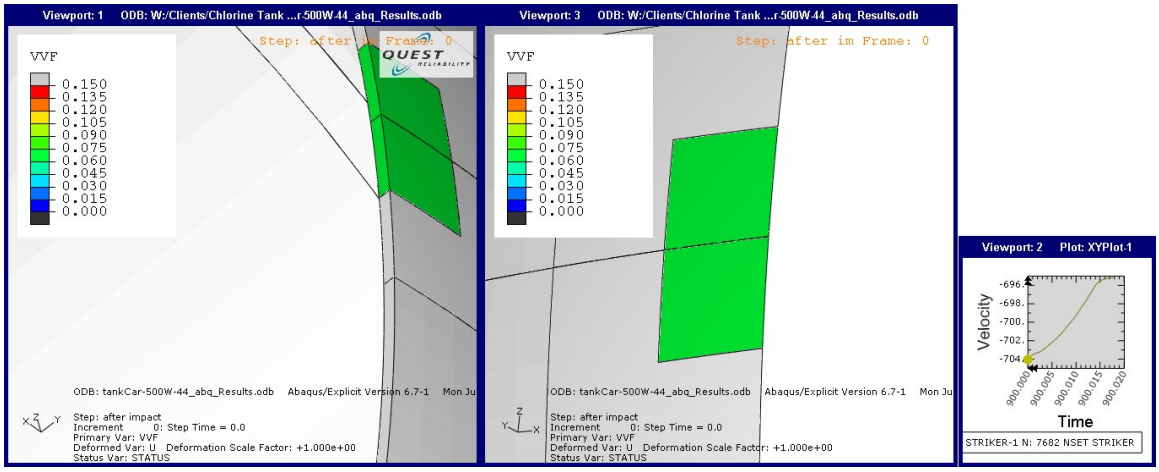

(a) Time = 0 ms

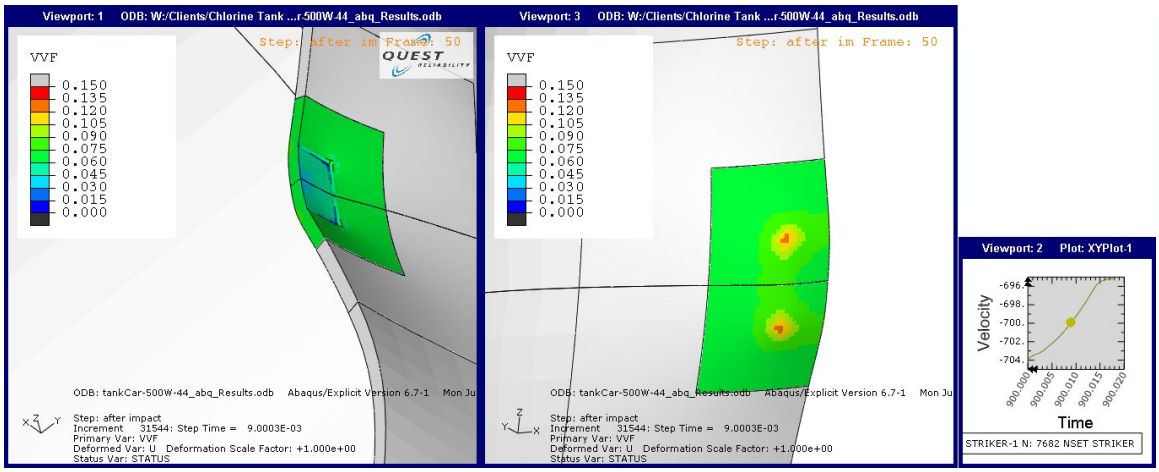

(b) Time = 9 ms

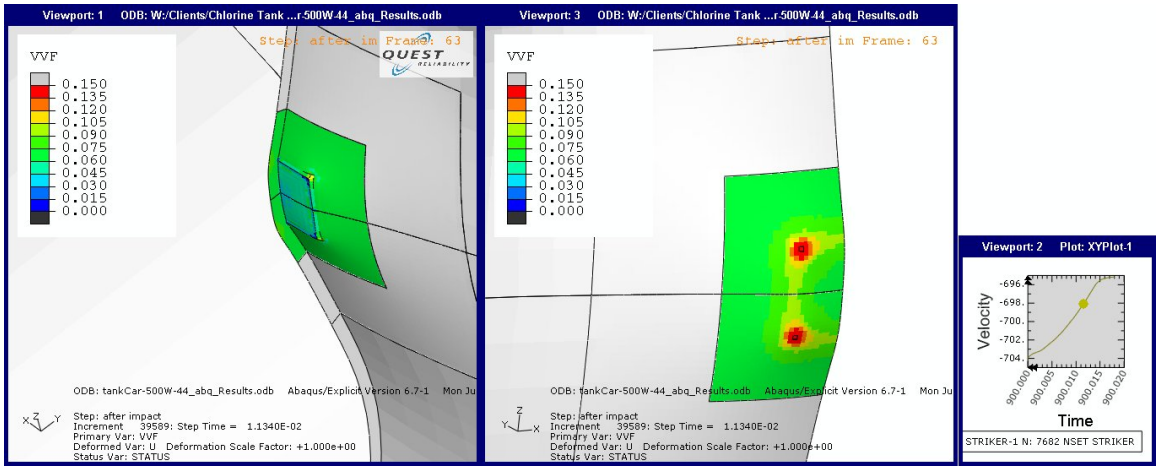

(c) Time = 11.3 ms

FIGURE 4.10 Typical simulation of a head impact (no head shield or jacket).

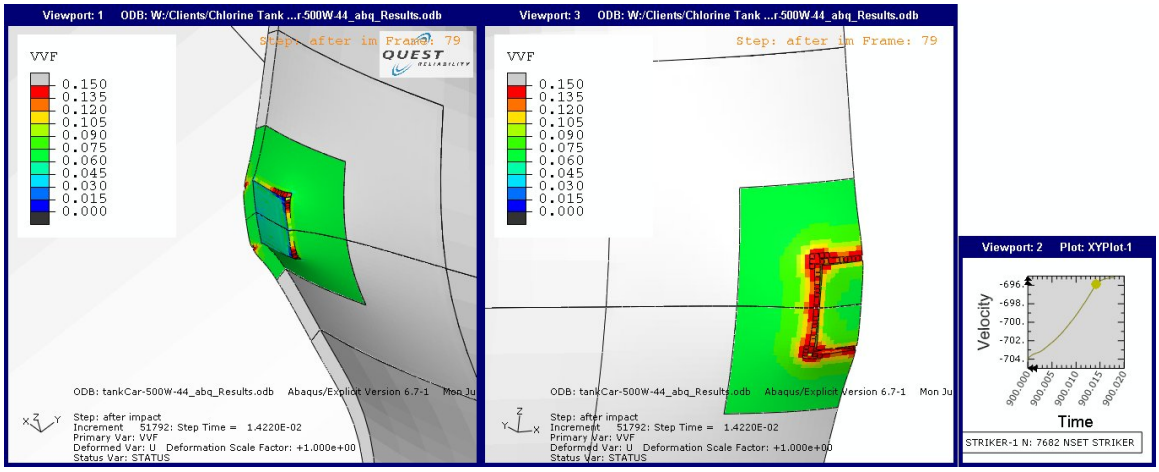

(d) Time = 14.2 ms

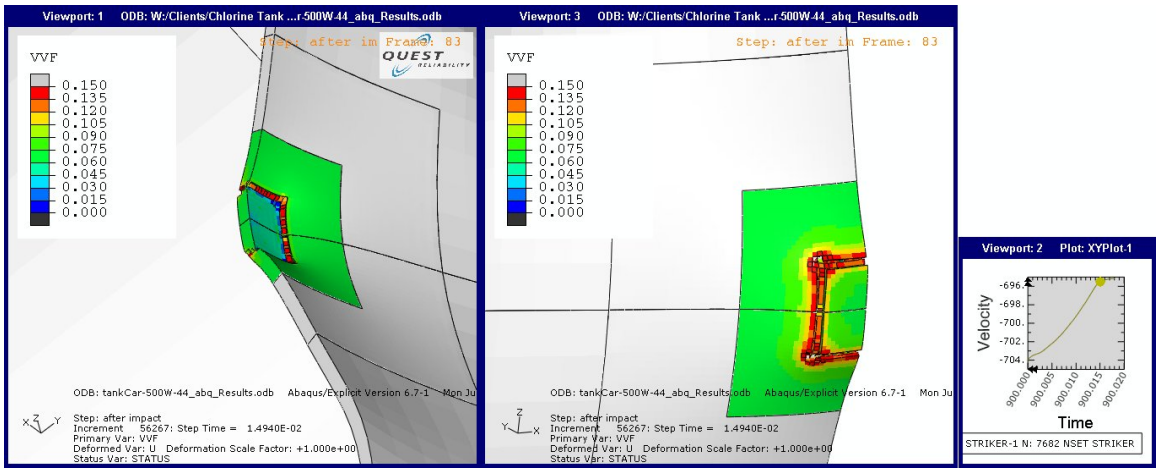

(e) Time = 14.9 ms

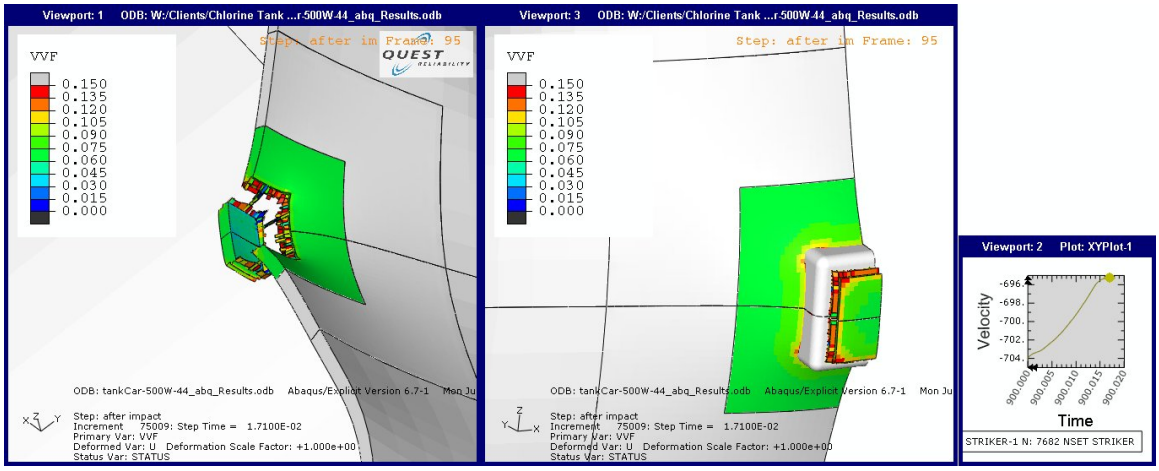

(f) Time = 17.1 ms

FIGURE 4.10 (Cont.)

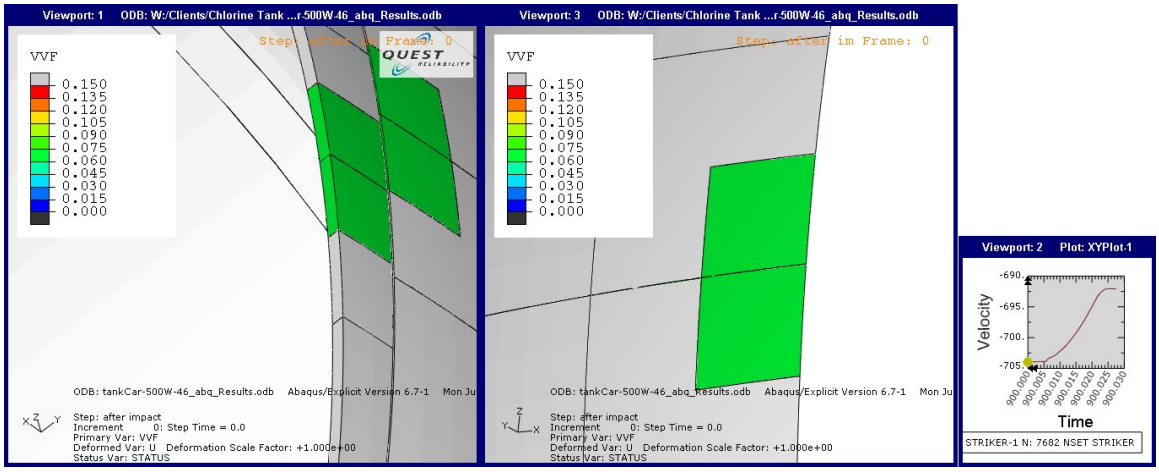

(a) Time = 0 ms

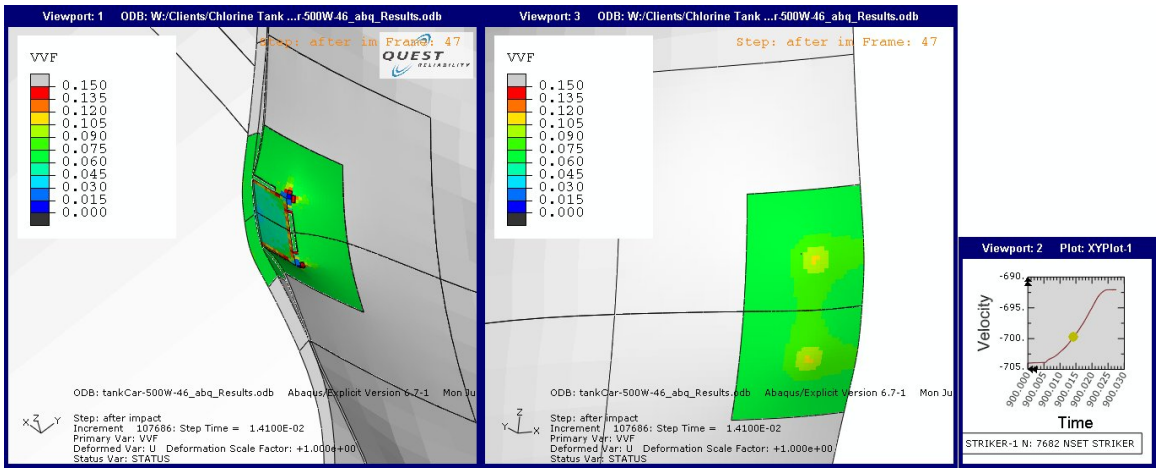

(b) Time = 14.1 ms

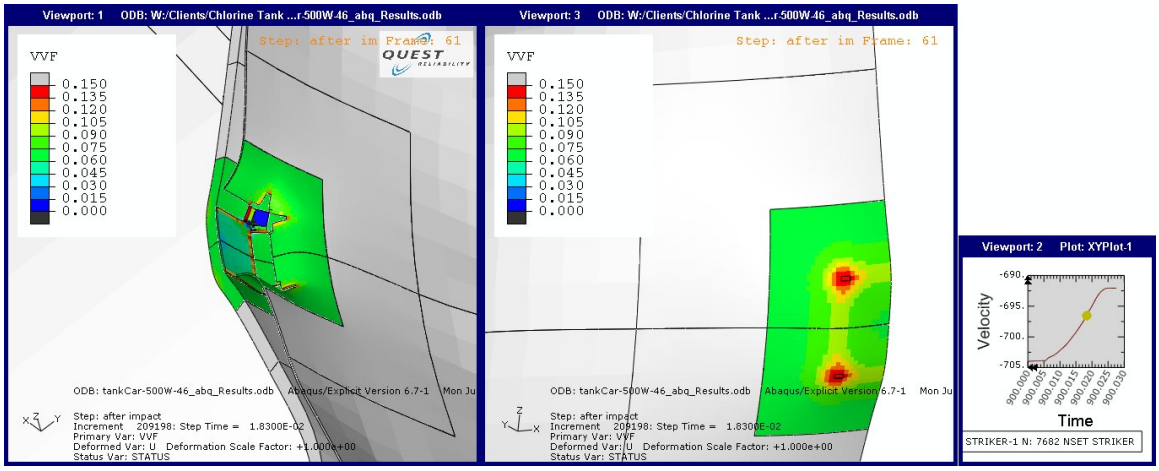

(c) Time = 18.3 ms

FIGURE 4.11 Typical simulation of a jacketed head impact.

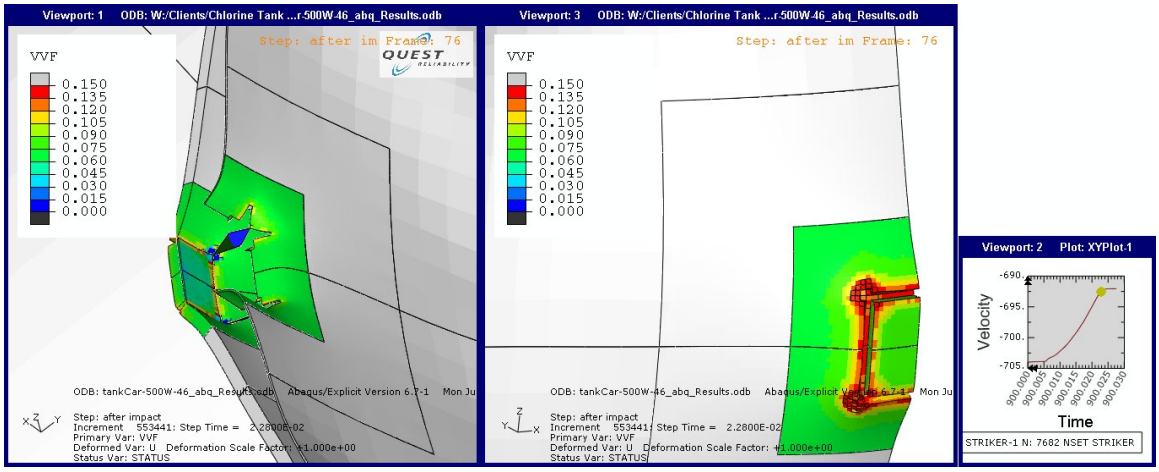

(d) Time = 22.8 ms

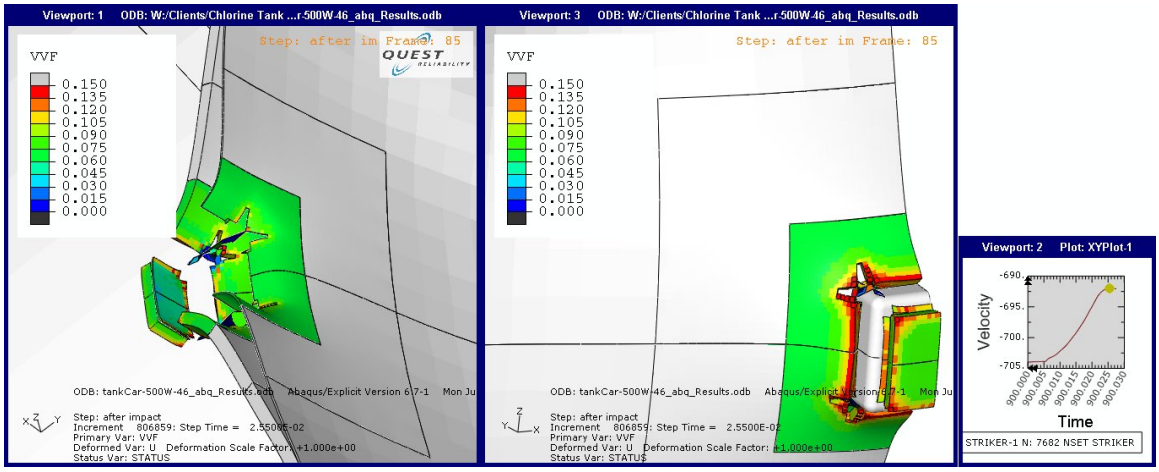

(e) Time = 25.5 ms

FIGURE 4.11 (Cont.)

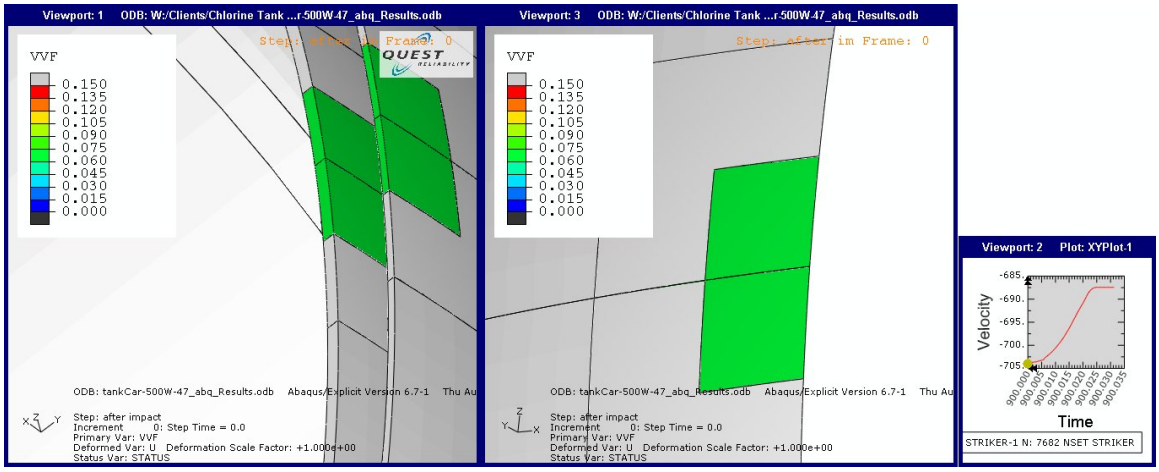

(a) Time = 0 ms

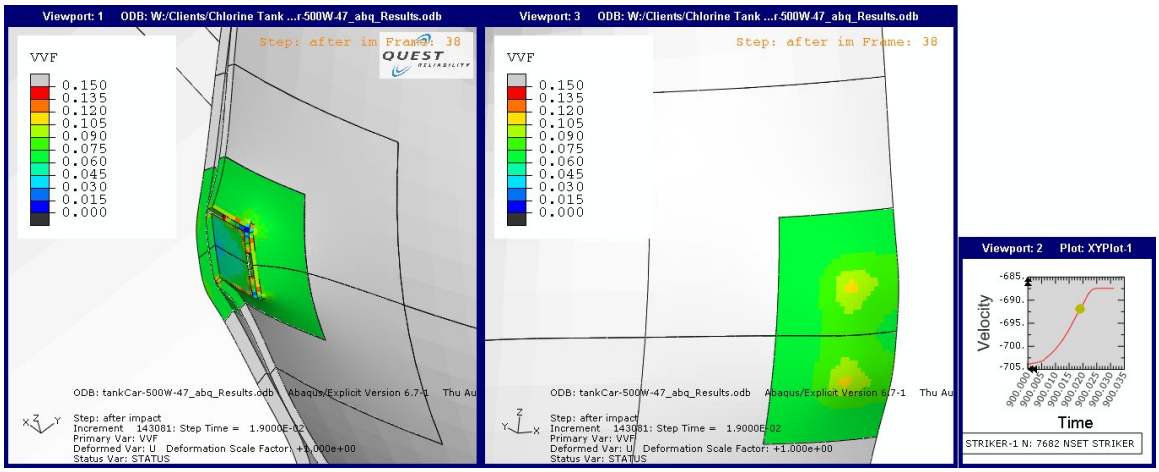

(b) Time = 19 ms

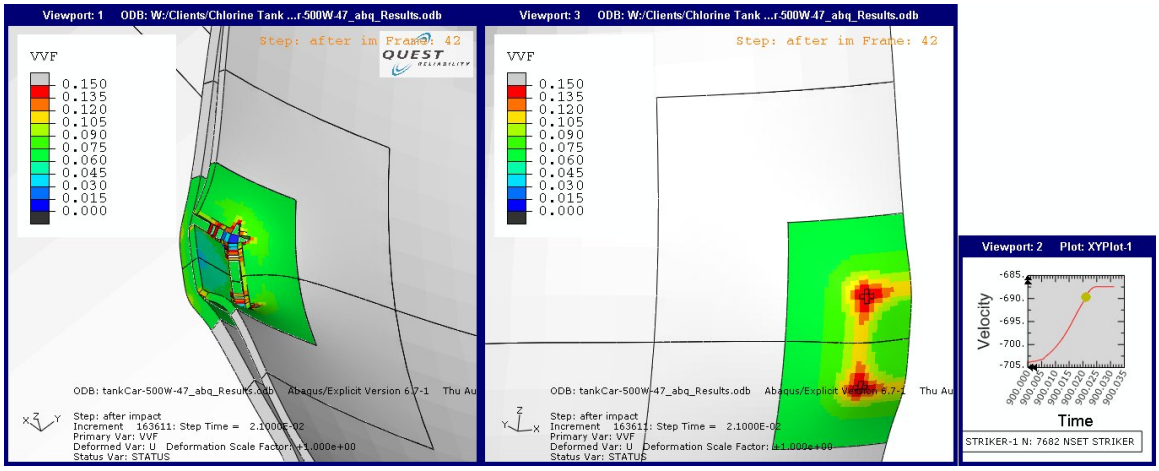

(c) Time = 21 ms

FIGURE 4.13 Typical simulation of a head impact on a jacketed car with head shield.

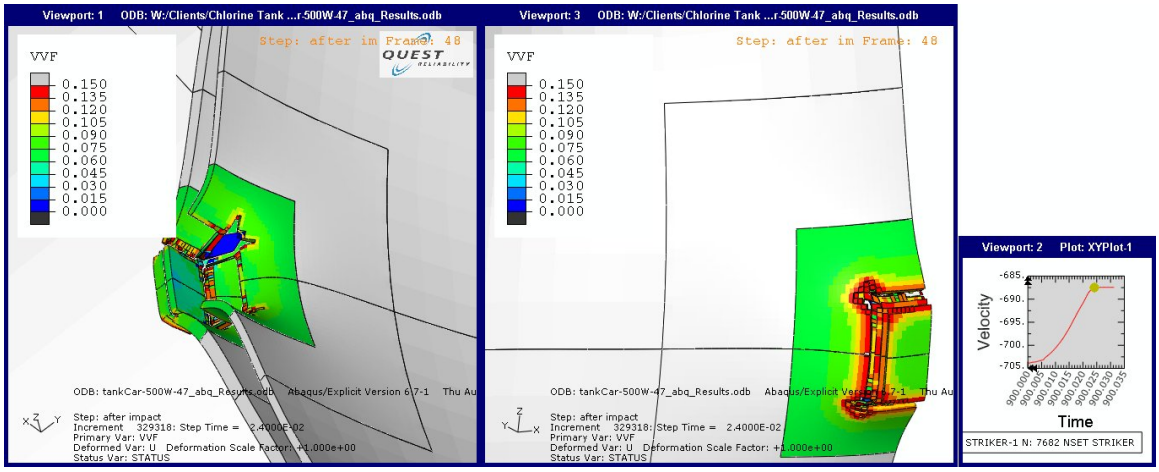

(d) Time = 24 ms

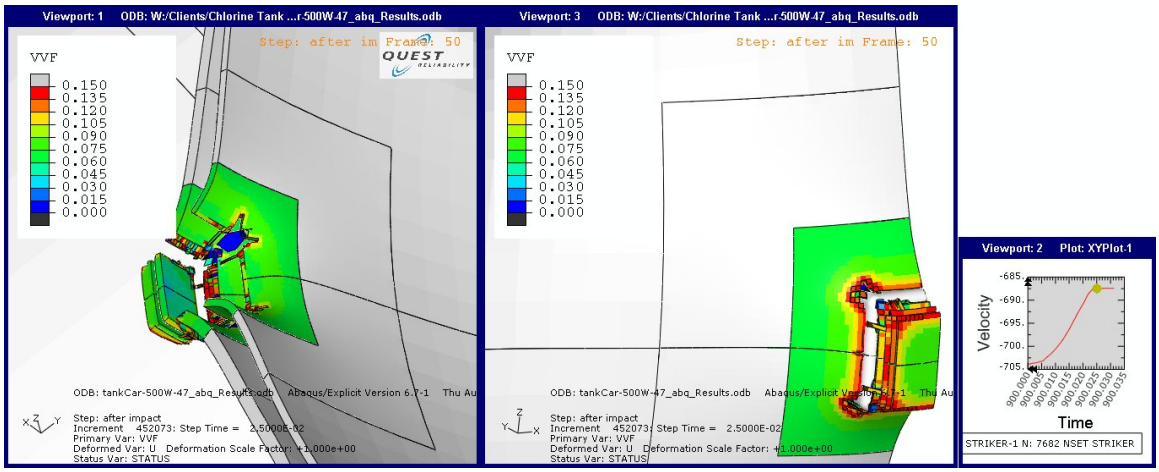

(e) Time = 25 ms

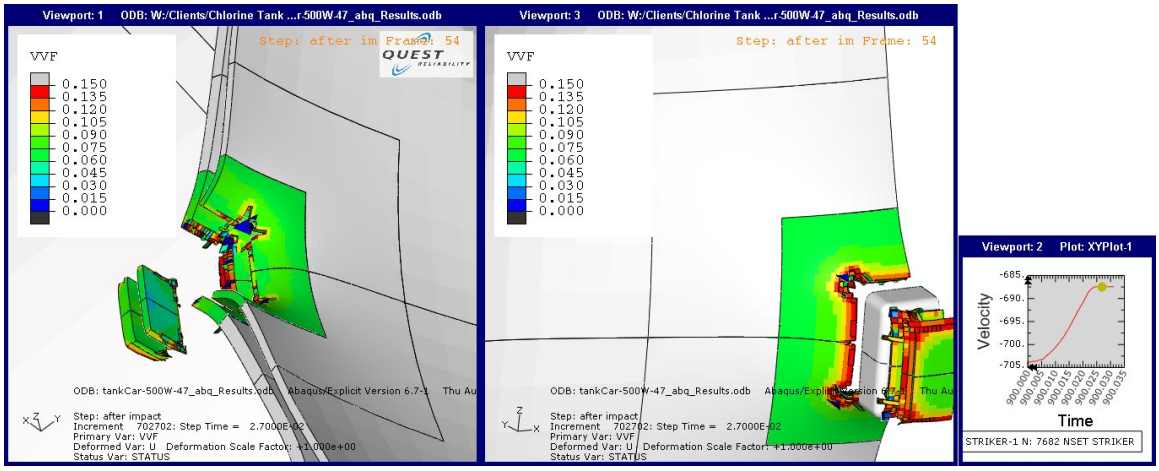

(f) Time = 27 ms

FIGURE 4.13 (Cont.)

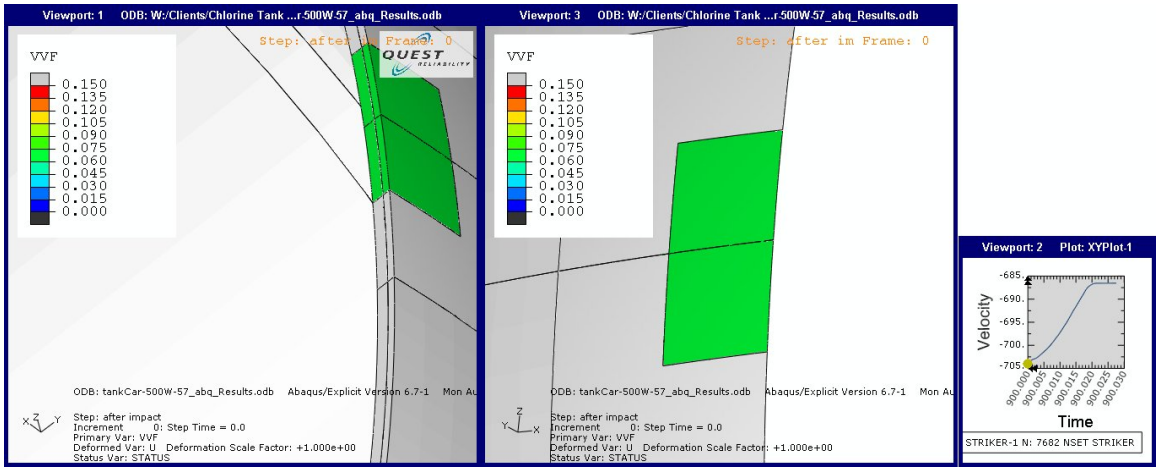

(a) Time = 0 ms

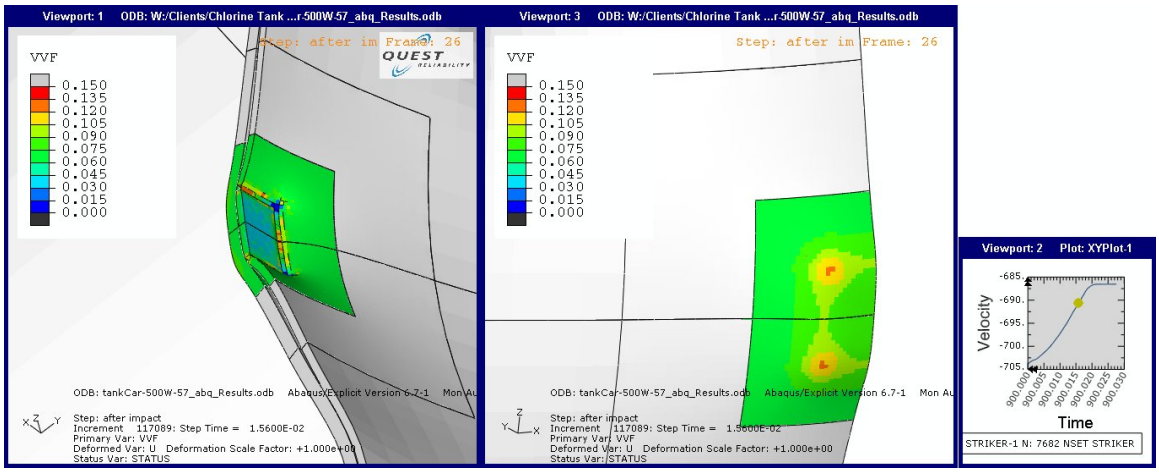

(b) Time = 15.6 ms

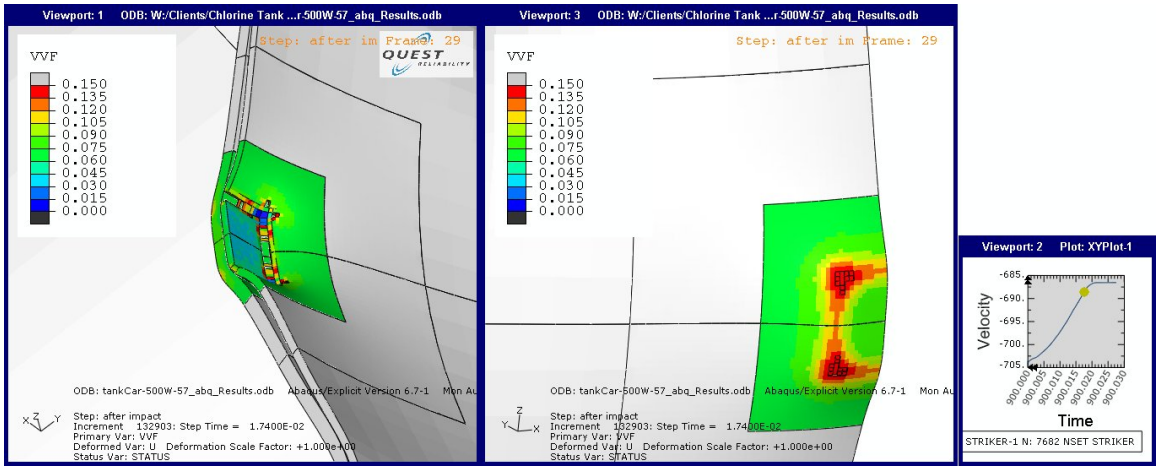

(c) Time = 17.4 ms

FIGURE 4.14. Typical simulation of a head impact on an unjacketed car with a head shield.

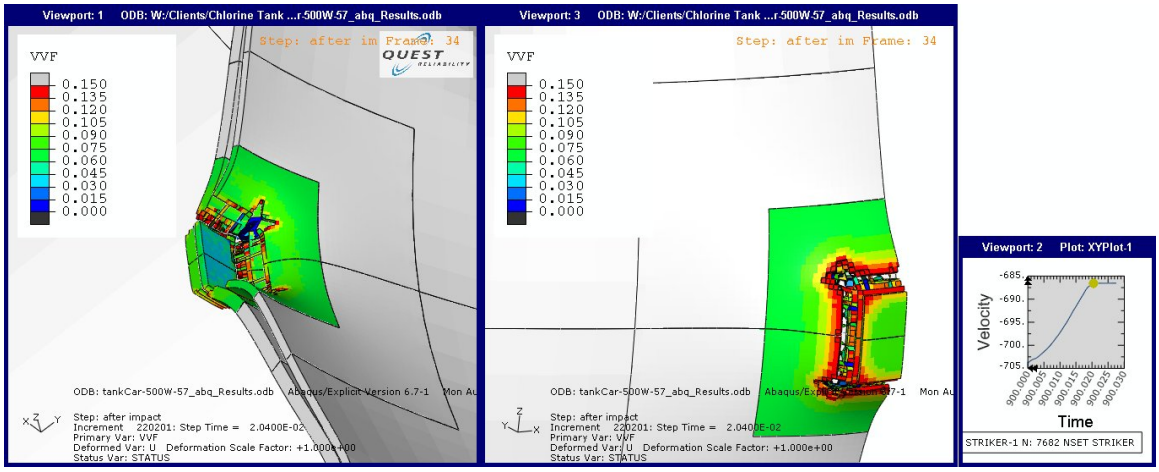

(d) Time = 20.4 ms

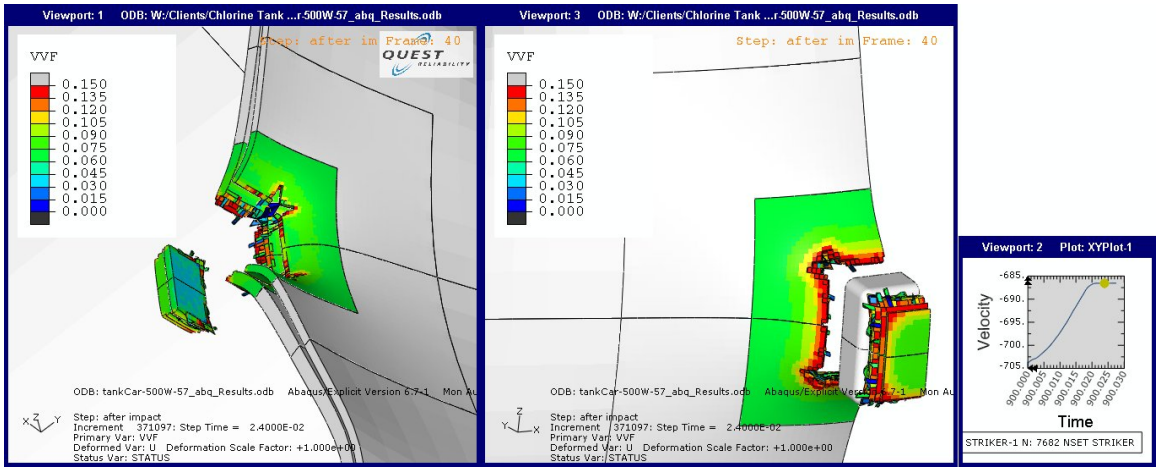

FIGURE 4.x Simulation, 500W, head impact, unjacketed car with head shield, at time = 24 ms

FIGURE 4.14 (Cont.)

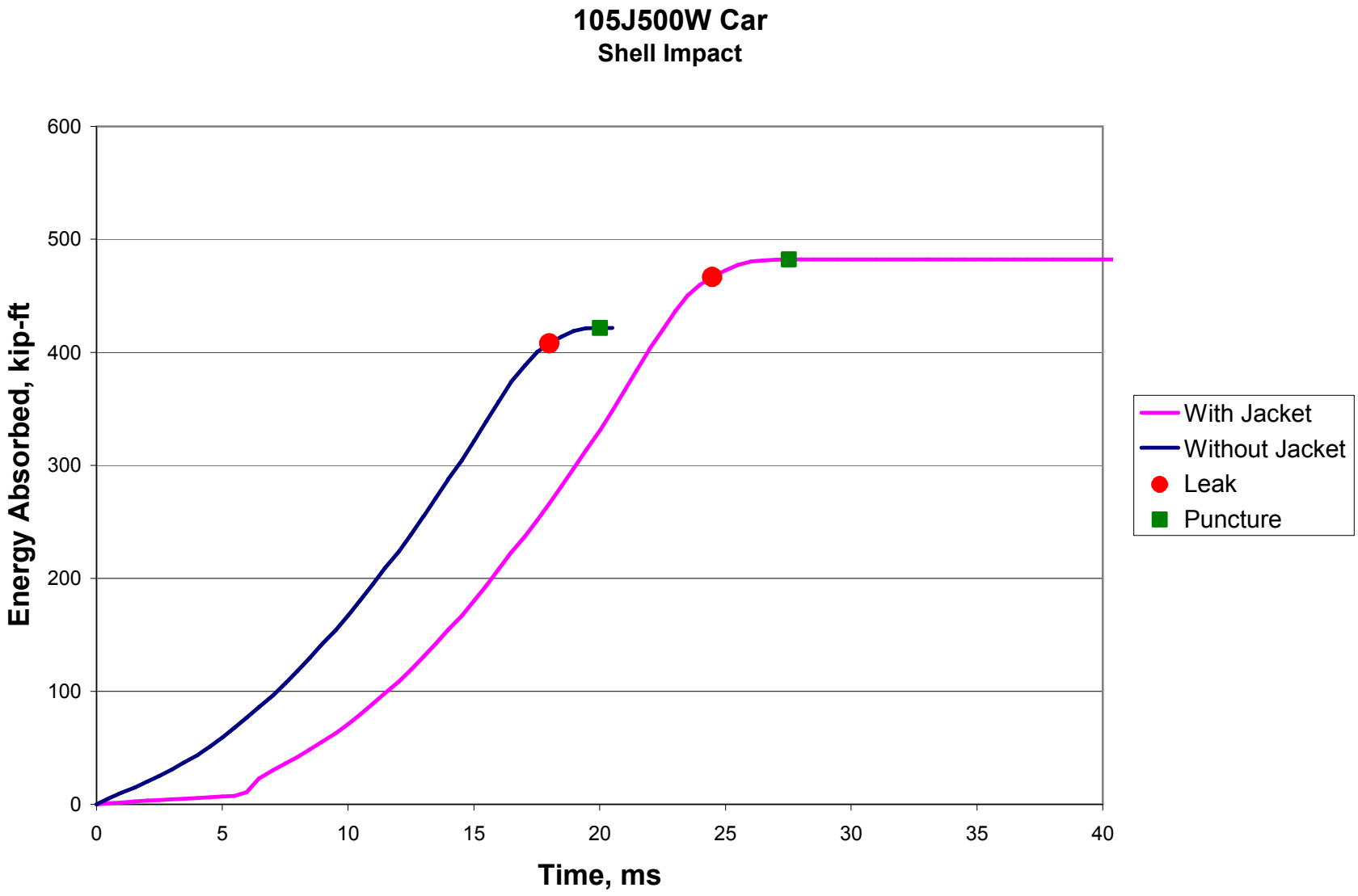

FIGURE 4.15 Absorbed energy versus time for a 105J500W car with and without a jacket.

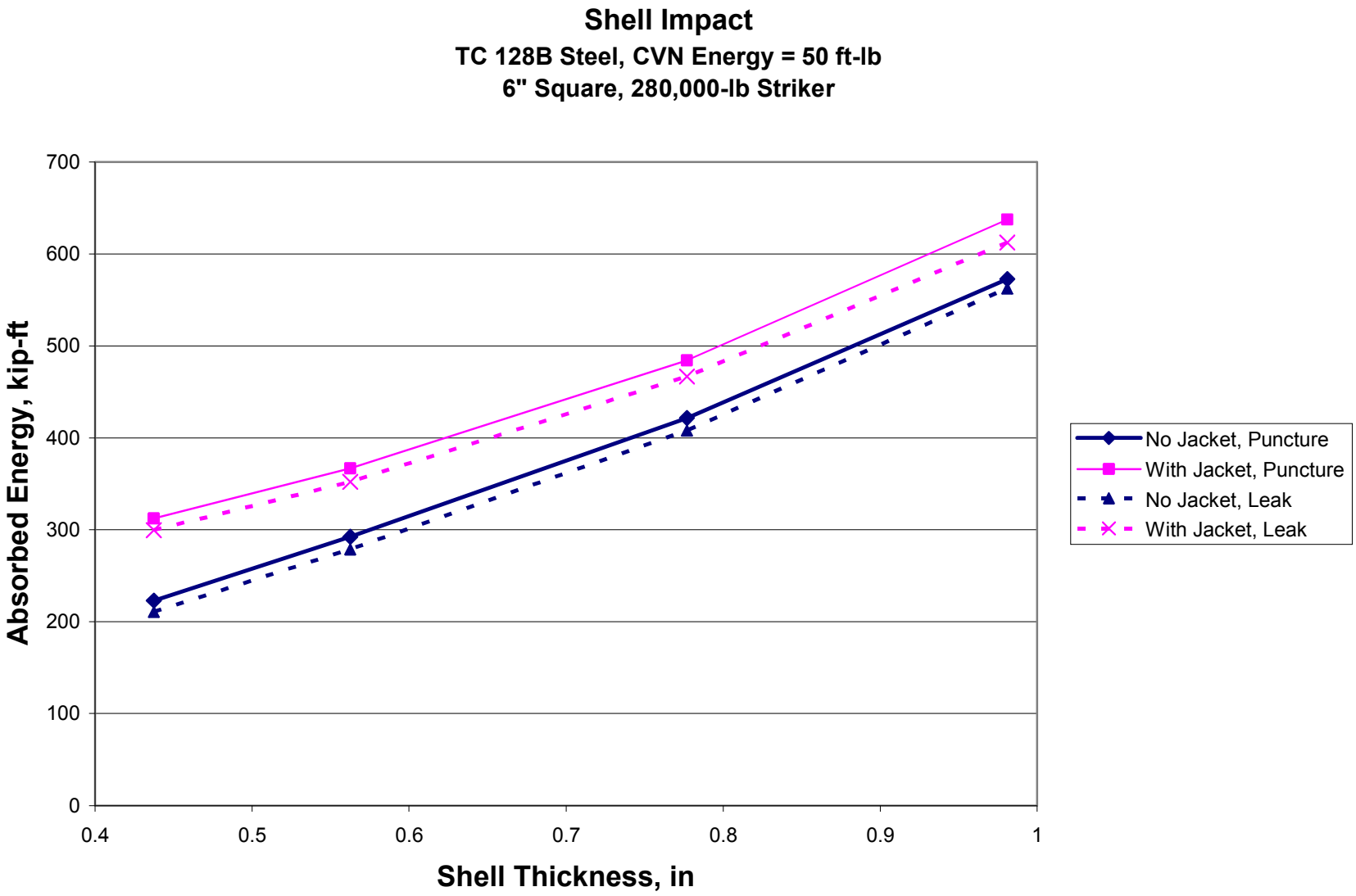

FIGURE 4.16 Effect of shell thickness and a jacket on the energy required for leak or puncture.

5 TANK CAR IMPACT SIMULATION RESULTS

Over 100 finite element simulations of tank car impacts were performed in this project. Appendix B list the 83 *successful* simulations that were considered. A parametric study was conducted to quantify the effect of a number of variables and modeling assumptions on computed puncture resistance. A series of simulations were calibrated to the RSI-AAR Accident Database to relate puncture energy to probability of lading loss. In addition, the simulation methodology employed here was benchmarked against a recent full-scale test conducted at the Transportation Technology Center, Inc. (TTCI) in Pueblo, Colorado.

The energy to cause a leak or complete puncture was computed from Eq. (4.2). The minimum velocity for a leak or puncture can be estimated from the corresponding energy as follows:

$$V = \sqrt{\frac{2E}{m}} \tag{5.1}$$

The above relationship assumes that the puncture energy does not depend on initial velocity. This assumption is not strictly correct, so the inferred puncture velocities should be viewed as approximate.

The calculated puncture velocities should not been applied literally to actual accidents. For example, if the computed puncture velocity is 9 mph, it should not be assumed that a 9 mph collision will necessarily result in lading loss in an accident. The velocity required for puncture is a function of a number of factors, including the mass driving the collision, the object impacting the tank, and the location of the impact. Moreover, the collision speed is not necessarily the same as the train speed, since rail cars typically decelerate during a derailment.

Unless otherwise stated, the values of energy and velocity (or speed) that are reported and plotted correspond to that required for complete puncture. The conditions for leak are somewhat subjective, but the puncture energy can be defined unambiguously. In any case, the difference between puncture energy and energy to leak is generally small, as Figs. 4.15 and 4.16 illustrate.

5.1 Parametric Study

A number of variables were considered in the parametric study: pressure, striker size, initial velocity, friction, and lading mass. The effect of jackets and head shields is considered in Section 5.2, and the effect of material toughness is addressed in Section 5.3. The analyses that follow are all shell impacts on unjacketed tank cars. Tables 4.1 and 4.2 describe the tank car configurations that were analyzed.

Note that the parametric study was conducted in parallel with the material model calibration (Section 3). Consequently the initial porosity in the analyses below varies from one parametric analysis to the next, and differs from the material properties used in the benchmark to the Accident Database. Once the material model calibration task was complete, we determined the -Charpy toughness that corresponds to the initial porosity used for each of the parametric

analyses. The corresponding Charpy values are indicated in the plot titles. We have not investigated the effect of varying toughness on the conclusions drawn from the various parametric studies, but the *relative* effects of other variables such as pressure and section thickness should not be sensitive to the assumed material toughness.

5.1.1 Effect of Internal Pressure

Figures 5.1 and 5.2 are plots of puncture energy and speed, respectively, as a function of internal pressure. The puncture resistance of a tank car at full design pressure is considerably lower than at normal operating levels. The empty tank car did not puncture during the simulated 40 mph collision event.

5.1.2 Effect of Striker Size

The 6-inch square striker geometry was chosen to coincide with the Next Generation Rail Tank Car Project test recently conducted at TTCI. As Figs. 5.3 and 5.4 illustrate, the puncture energy and minimum speed (for a weight of 280,000 lb) is sensitive to the size and shape of the object that impacts the tank car. The 6-inch square striker represents an extreme case.

5.1.3 Effect of Initial Velocity

Most simulations assumed an initial impact velocity of 40 mph. The higher the impact speed, the shorter the duration of the impact event, which translates to a shorter computation time in the simulation. In this particular parametric analysis, the initial speed was varied from 20 to 40 mph. The results are plotted in Figs. 5.5 and 5.6. In the initial set of simulations, the puncture energy and inferred minimum speed for puncture were relatively insensitive to the initial speed. However, subsequent simulations that incorporated lading mass (Section 5.5.1) did show a marked effect of initial impact velocity on puncture energy. When simulating a specific collision event (e.g. the Next Generation Project test at TTCI), it is best to use the actual velocity, but for a comparative study, it is reasonable to use a high velocity that guarantees puncture.

5.1.4 Effect of Friction

Most of the simulations performed in this study assume frictionless interaction between the striker, shell, jacket, etc. Figures 5.7 and 5.8 illustrate the effect of friction on the puncture energy and inferred puncture speed, respectively. As one would expect, including friction does increase the energy dissipation, but not to a large extent. The static coefficient of friction for steel on steel is approximately 0.5, but the dynamic value is considerably lower. A reasonable estimate for coefficient of friction for a dynamic impact event is around 0.1, where the effect on puncture energy is modest.

5.1.5 Effect of Lading Mass

Most analyses in this project incorporated the mass of the steel in the tank, jacket and head shield (where applicable), but did not consider the mass of the lading. In one set of runs, whose results are plotted in Figs 5.5 and 5.6, the lading mass was modeled by adjusting the density of the tank. This assumption does not place the center of gravity of the lading in the correct location, nor does it consider liquid sloshing effects. Therefore, incorporating lading mass by increasing the density of the shell and head is an approximation.

Table 5.1 compares the puncture energy with and without the lading mass incorporated by adjusting the density of the shell and head. In this case, incorporating lading mass increases the puncture energy and reveals a sensitivity to initial collision velocity. Thus the parametric study, which neglected lading mass in most cases, is suitable for comparison purposes, but the absolute values may not be reliable.

TABLE 5.1 Effect of including lading mass in the finite element simulation. 300W car without jacket.

Initial Collision Velocity, mph	Computed Puncture Energy, kip-ft	
	Without Lading Mass	With Lading Mass
20	545	896
30	552	781
40	505	636

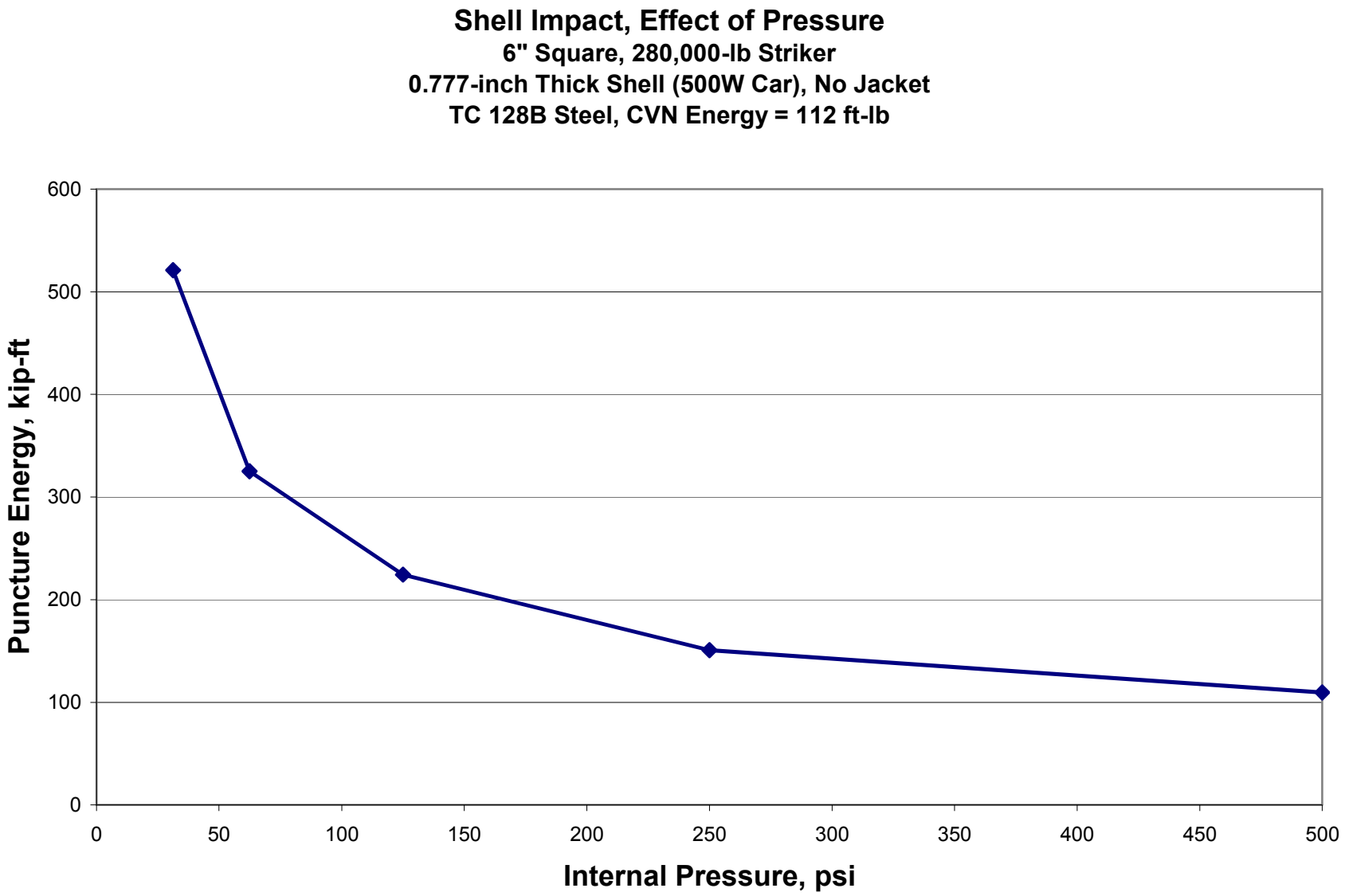

FIGURE 5.1 Effect of internal pressure on puncture energy for a shell impact. The shell did not puncture at zero internal pressure.

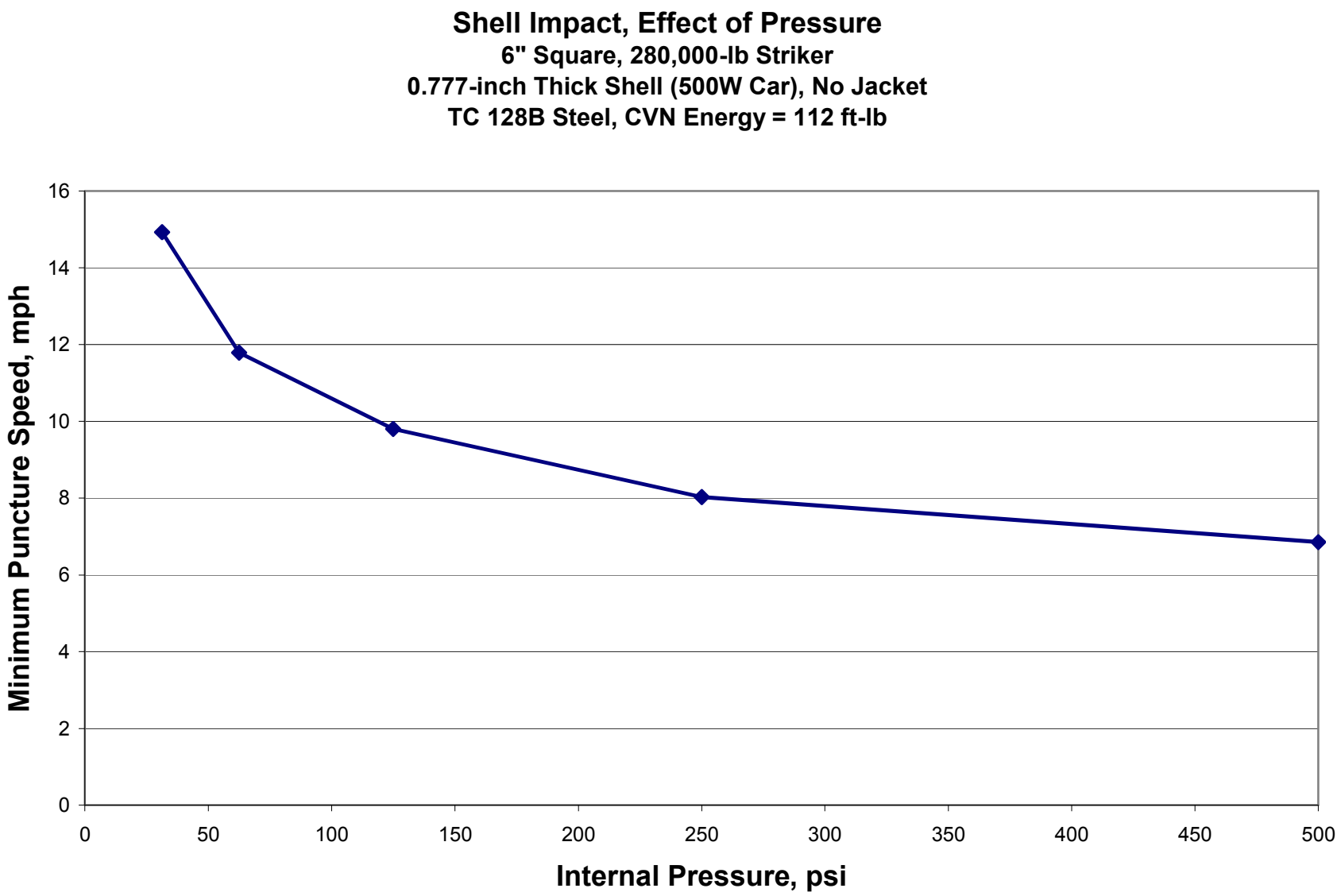

FIGURE 5.2 Effect of internal pressure on minimum puncture speed for a shell impact. The shell did not puncture at zero internal pressure.

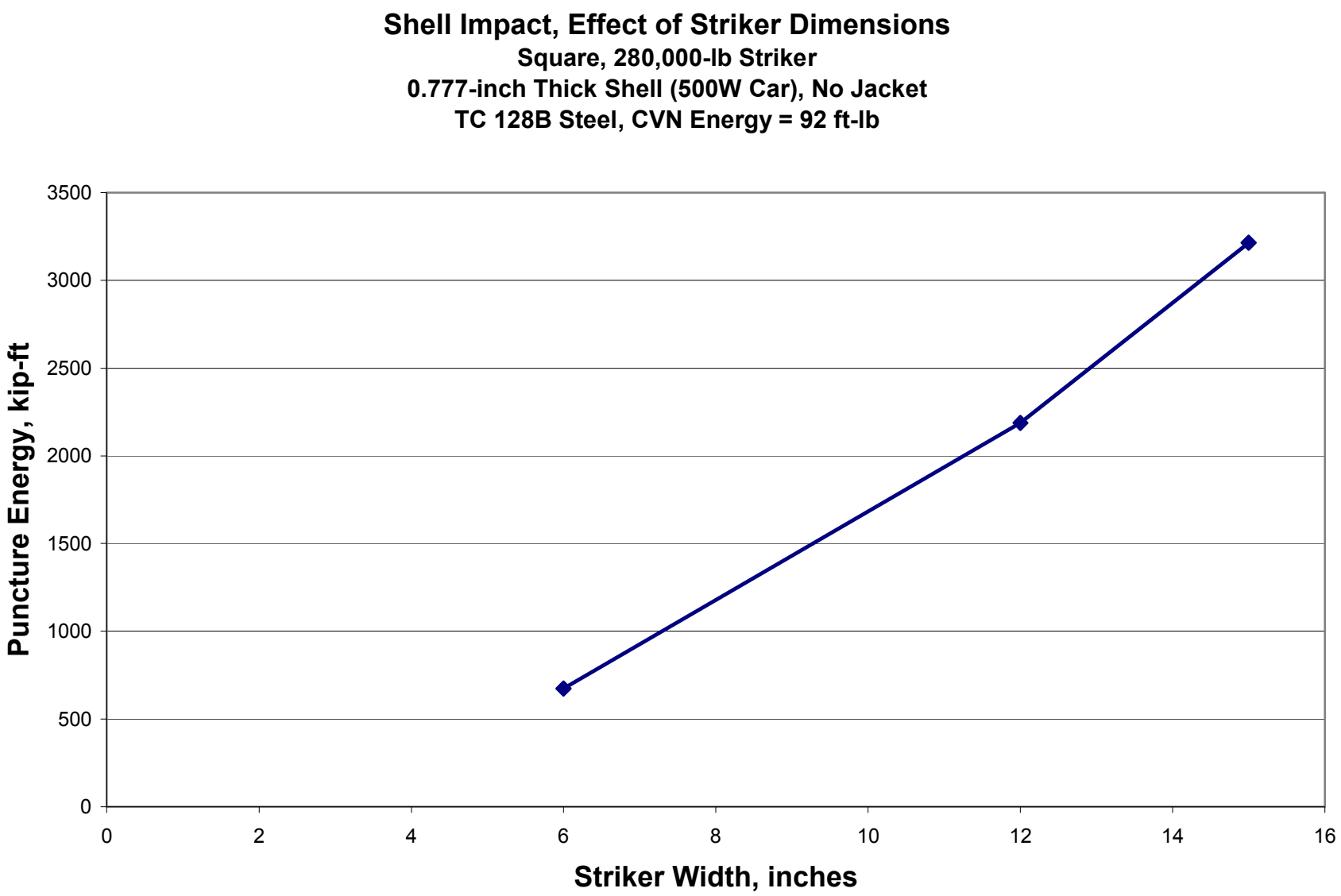

FIGURE 5.3 Effect of striker size on puncture energy for a shell impact.

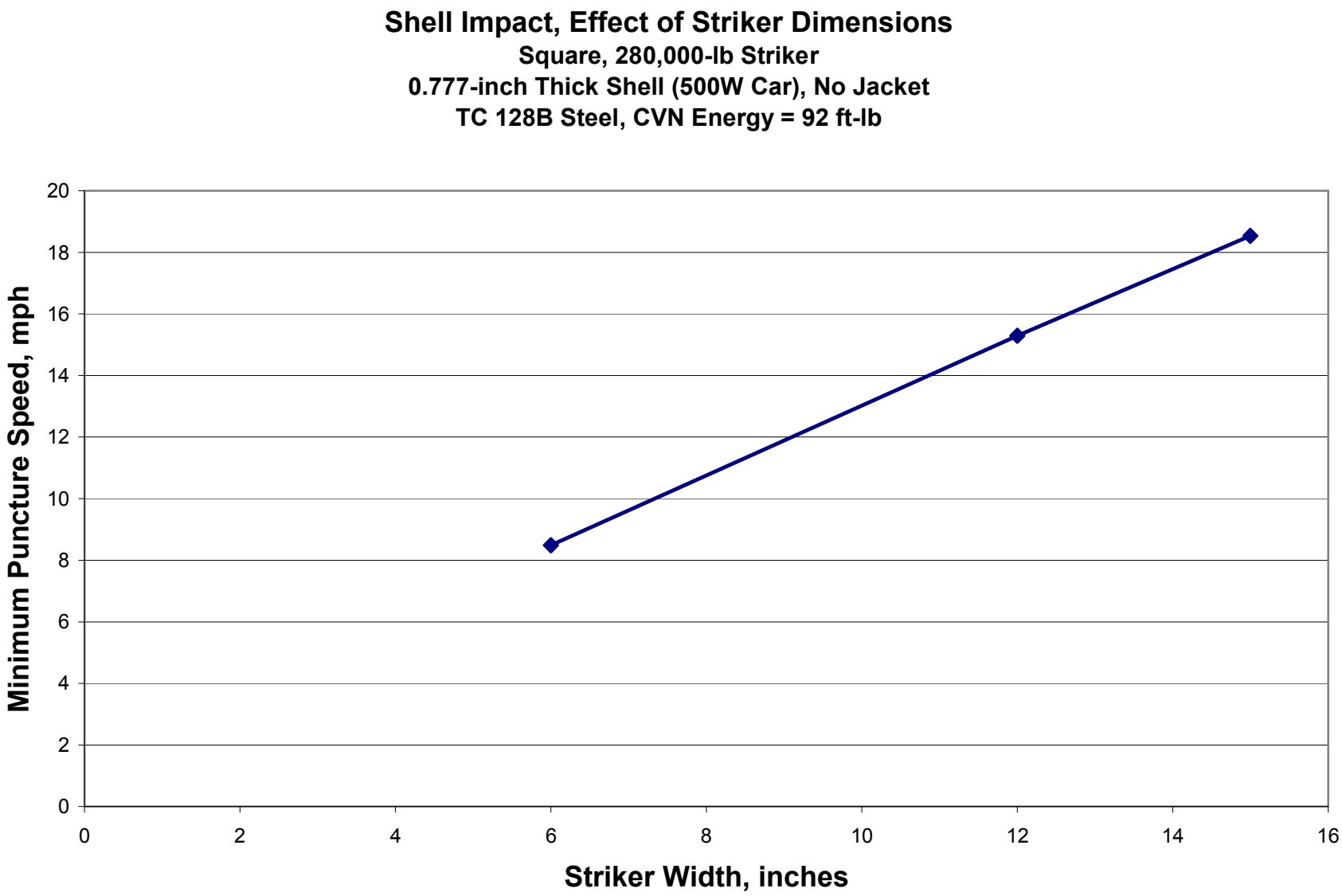

FIGURE 5.4 Effect of striker size on the minimum puncture speed.

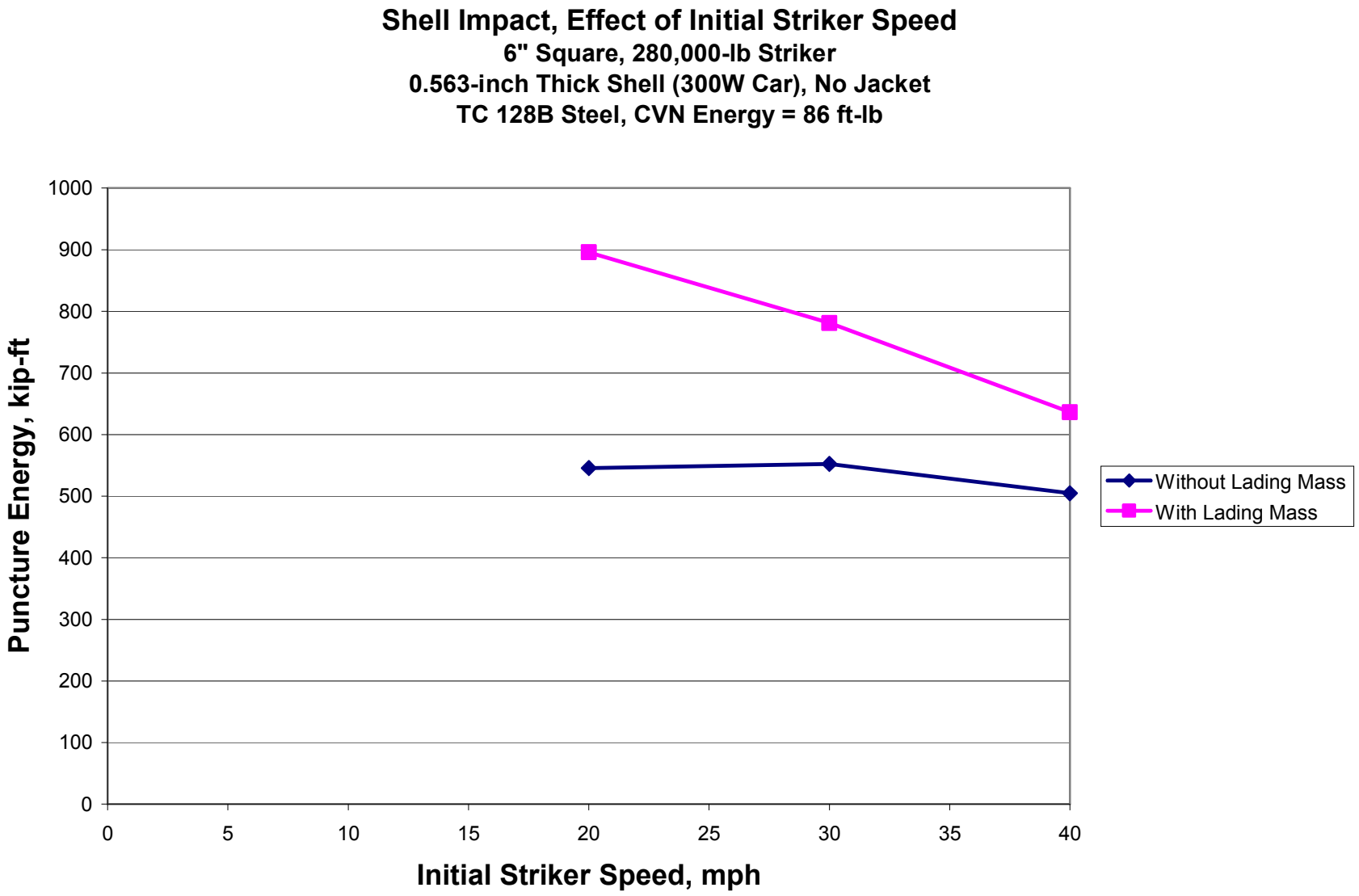

FIGURE 5.5 Effect of initial striker speed on puncture energy for a shell impact.

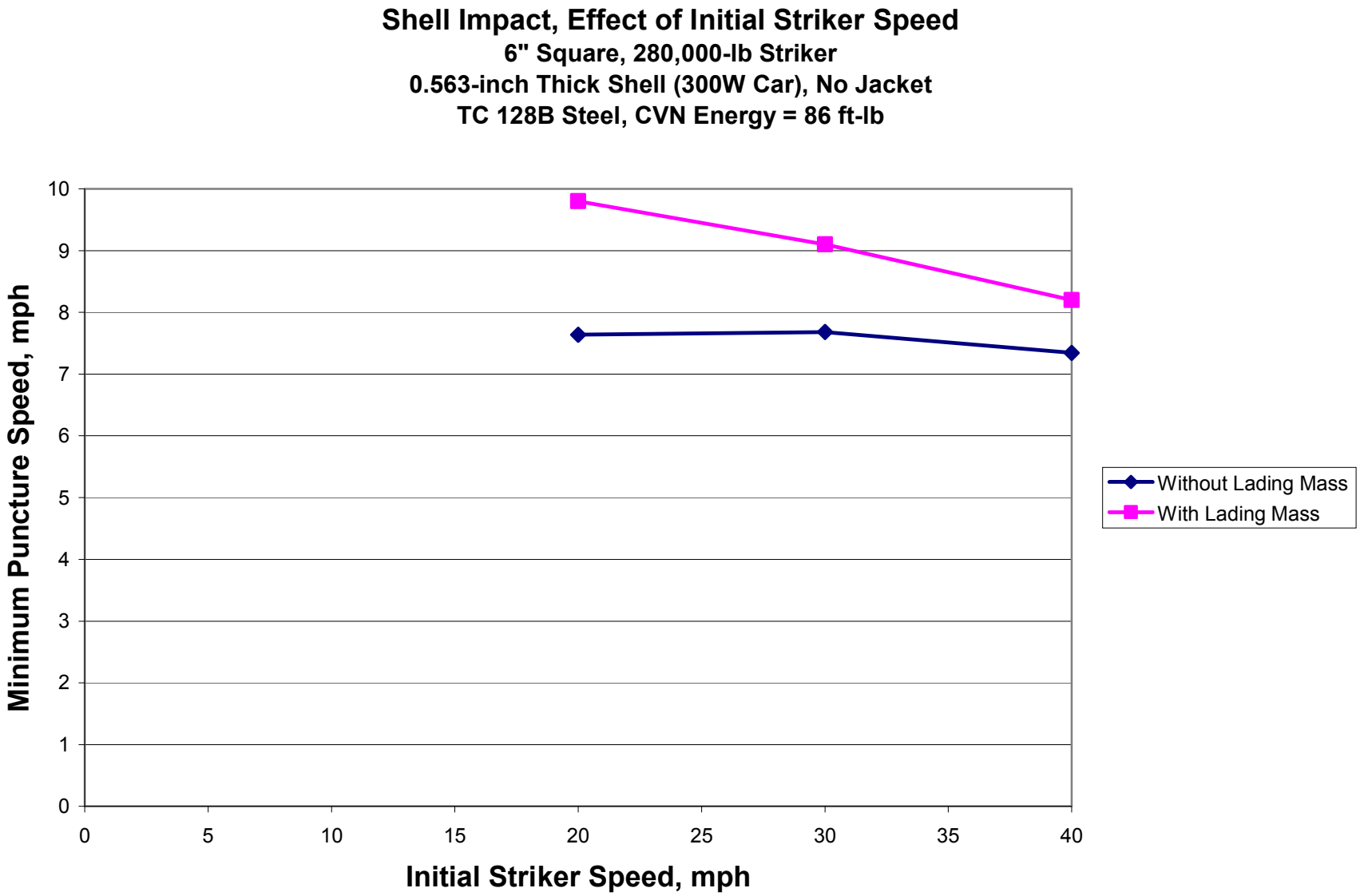

FIGURE 5.6 Effect of initial striker speed on minimum puncture speed for a shell impact

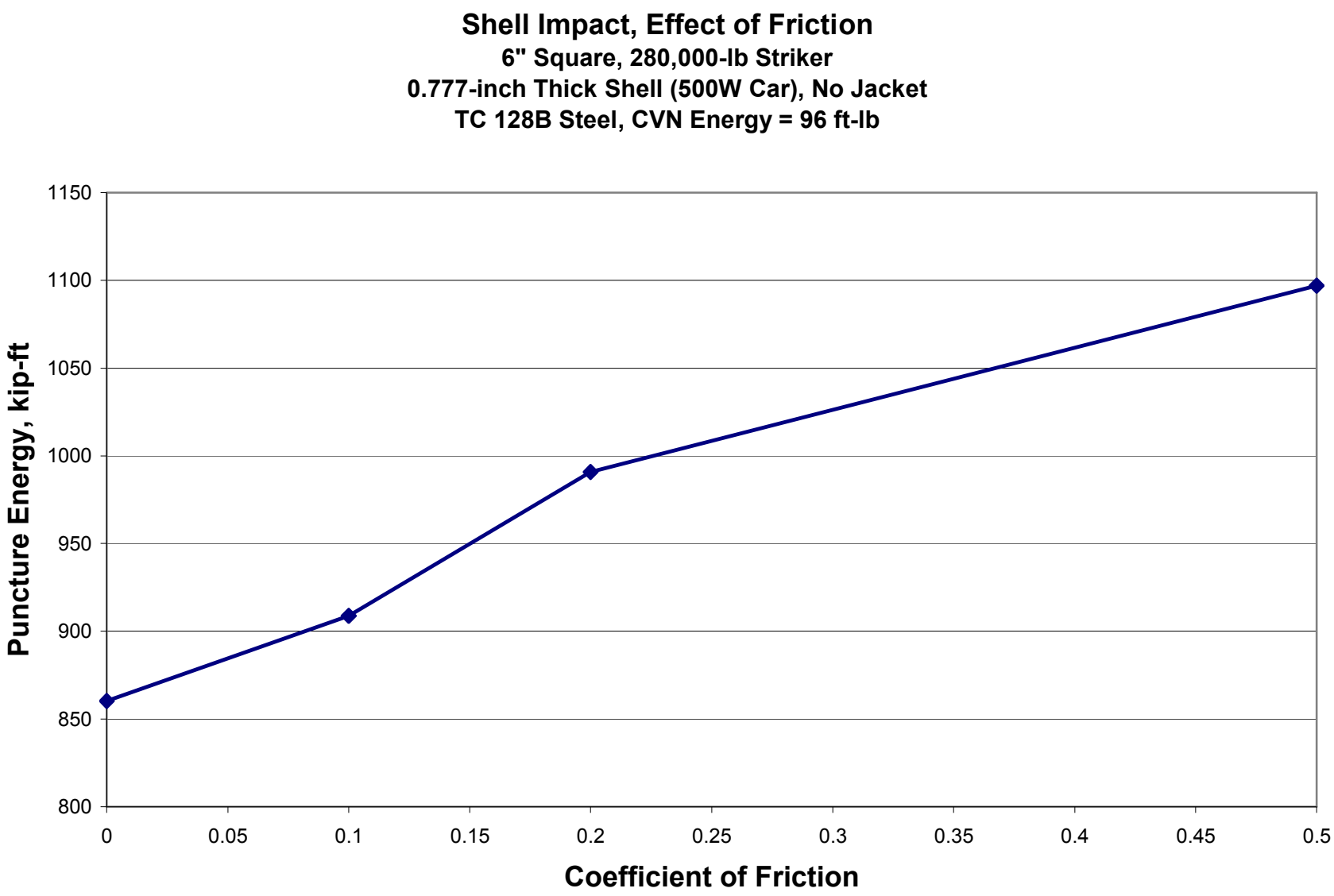

FIGURE 5.7 Effect of friction on puncture energy for a shell impact.

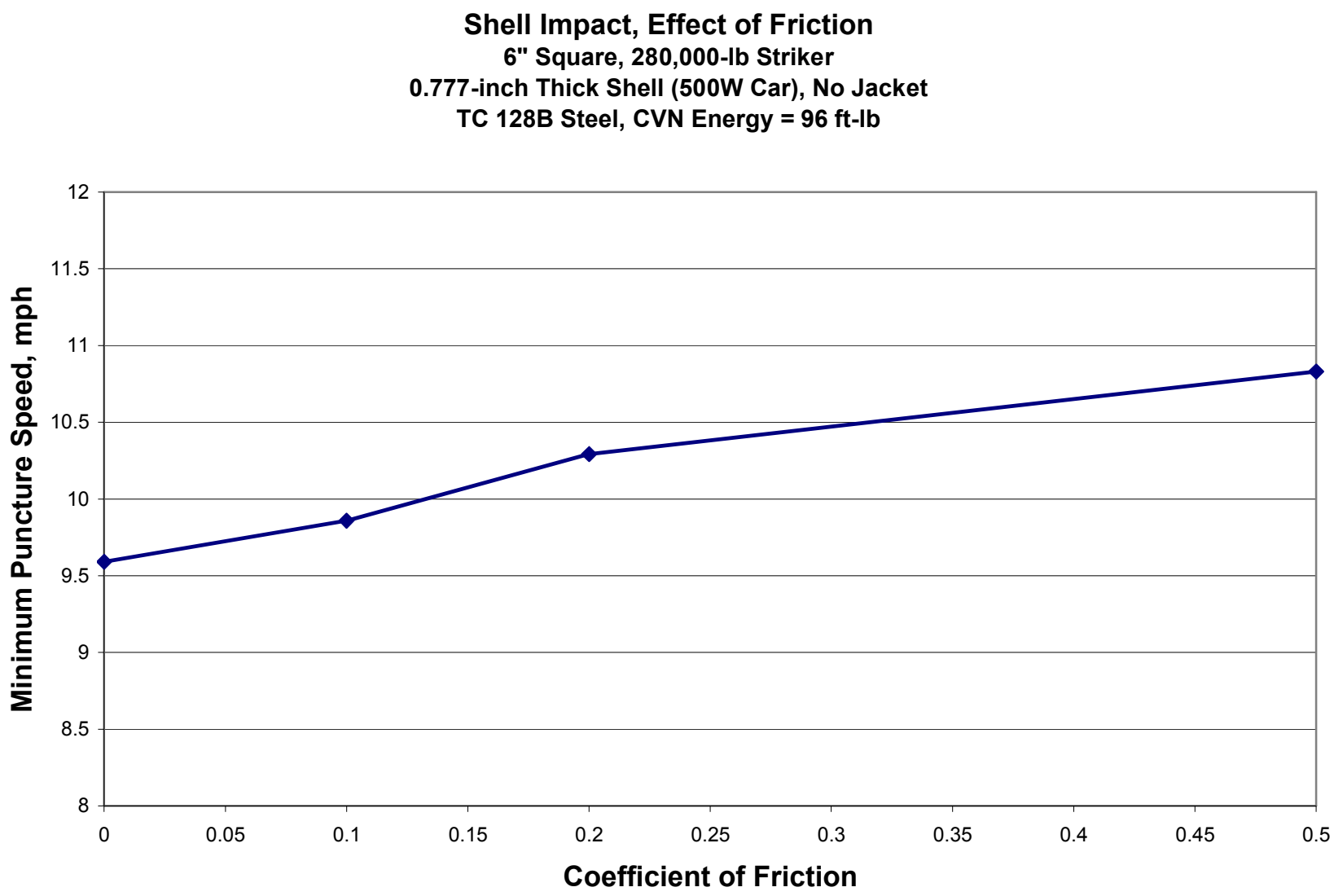

FIGURE 5.8 Effect of friction on minimum puncture speed for a shell impact.

5.2 Calibration to Accident Database

An extensive database of prior rail accidents and resulting lading loss, created and maintained by the RSI-AAR Railroad Tank Car Safety Research and Test Project, has been used in a number of projects over the years. In a recent RSI-AAR project [7], a regression analysis was performed on the database to extract smooth trends for lading loss probability as a function of a number of key variables. Some of these trends are plotted in Figs. 5.9 and 5.10.

These curves show that lading loss probability decreases with section thickness. The addition of a jacket or head shield also reduces lading loss probability. Such trends make intuitive sense. Rail accidents such as derailments are complex and chaotic events. Collisions of varying degrees of severity have occurred in rail accidents over the years, some of which result in lading loss. A given collision that causes lading loss in an unjacketed car may not have resulted in lading loss if the car had a jacket and head shield, if it had a greater section thickness, or if it were made from a higher-toughness steel.

The Phase I report [1] introduced the concept of *puncture intensity*, I, which can be viewed as the driving force for puncture:

$$\text{Puncture Intensity } (I) = \text{ Kinetic Energy} \times f(G_1, G_2, G_3, \cdots) \tag{5.2}$$

The available kinetic energy in the collision $\left(mV^2/2\right)$ is multiplied by a function of geometry factors, G_i, which include the size and geometry of the object that strikes the car, the location of the impact, and the angle of impact. Puncture occurs when the driving force, I, exceeds the puncture resistance, I_R, which depends on material properties, section thickness, etc.

It is possible to describe the puncture intensity statistically by combining the trends inferred from the accident database with finite element simulation of head and shell impacts. Consider, for example, a jacketed tank car with $^9/_{16}$ –inch (0.5625") shell thickness. According to Fig. 5.9, this configuration has a 4% probability of lading loss through the shell in a mainline accident. Stated another way, an impact event in the 96th percentile or greater is required to cause lading loss through the shell in this case. Referring to Eq. (5.2), there are an infinite number of combinations of kinetic energy and geometry factors that will produce a given I value. For the present finite element study, $f(G_i)$ is fixed, so we can quantify puncture intensity in terms of kinetic energy, and substitute puncture energy for I_R. Therefore, the 96th percentile kinetic energy for shell impacts is equal to the puncture energy for a jacketed car with $^9/_{16}$ –inch shell thickness. The puncture energy of a variety of tank car configurations can be determined from finite element simulation, and the corresponding percentiles determined in a similar matter. The results can then be fit to a statistical distribution.

A series of finite element simulations of tank car impacts were performed in order to benchmark to the accident database. The 4 base car configurations in Table 4.1 were subjected to the 6 collision scenarios listed in Table 4.2 (24 simulations total). A Charpy toughness of 50 ft-lb was assumed, which should be reasonably representative of properties of the existing tank car fleet.

The results of the benchmark simulations are given in Figs. 5.11 to 5.14. These results can be combined with Figs. 5.9 and 5.10 to construct a statistical distribution of impact energy in past accidents. Note that the specific collision scenario considered here (6" striker and 280,000 lb weight) is meant to be a surrogate for the infinite range of possibilities, as expressed by Eq. (5.2). To reiterate, $f(G_i)$ is held constant, and energy (for this specific collision scenario) is described statistically in place of the more general parameter, I. Given that $f(G_i)$ is fixed, energy and I should exhibit the same statistical variance.

As was the case in the Phase I project [1], the Weibull model was used to describe the statistical distribution of impact energy:

$$F = 1 - \exp\left[-\left(\frac{E}{\theta} \right)^{\beta} \right] \tag{5.3}$$

where F is cumulative probability and θ & β are fitting constants. For the purpose of plotting and fitting data, Eq. (5.3) can be linearized as follows:

$$\ln\left[-\ln\left(1 - F\right) \right] = \beta \ln\left(E\right) - \beta \ln\left(\theta\right) \tag{5.4}$$

Figures 5.15 and 5.16 are Weibull plots for shell and head impacts, respectively. The Weibull fit for shell impacts is given by

$$F = 1 - \exp\left[-\left(\frac{E}{72.173} \right)^{0.72733} \right] \tag{5.5}$$

The fit for head impacts is as follows:

$$F = 1 - \exp\left[-\left(\frac{E}{28.876} \right)^{0.4526} \right] \tag{5.6}$$

where energy has units of kip-ft. The above expressions can be used to predict the effect of design modifications and improved material properties, as discussed in Section 5.4.

Note that for the Weibull plot of shell impacts (Fig. 5.15), the data for jacketed and unjacketed tanks are consistent with one another. For head impacts, however, the data are more scattered (Fig. 5.16). The most likely explanation for the greater scatter in Fig. 5.16 is uncertainty in the thickness of head jackets and head shields. In Report RA-05-02, jacketed cars without head shields are lumped into one group and jacketed cars *with* head shields are in a second group. In the finite element study, we assumed a 0.112-inch head jacket for the first case and a 0.5-inch head shield (with a standoff) for the latter group. In reality, the thicknesses of head shields and head jackets can vary, and these values are not recorded in the accident database. Given these unknown dimensions, the scatter in Fig. 5.16 is reasonable.

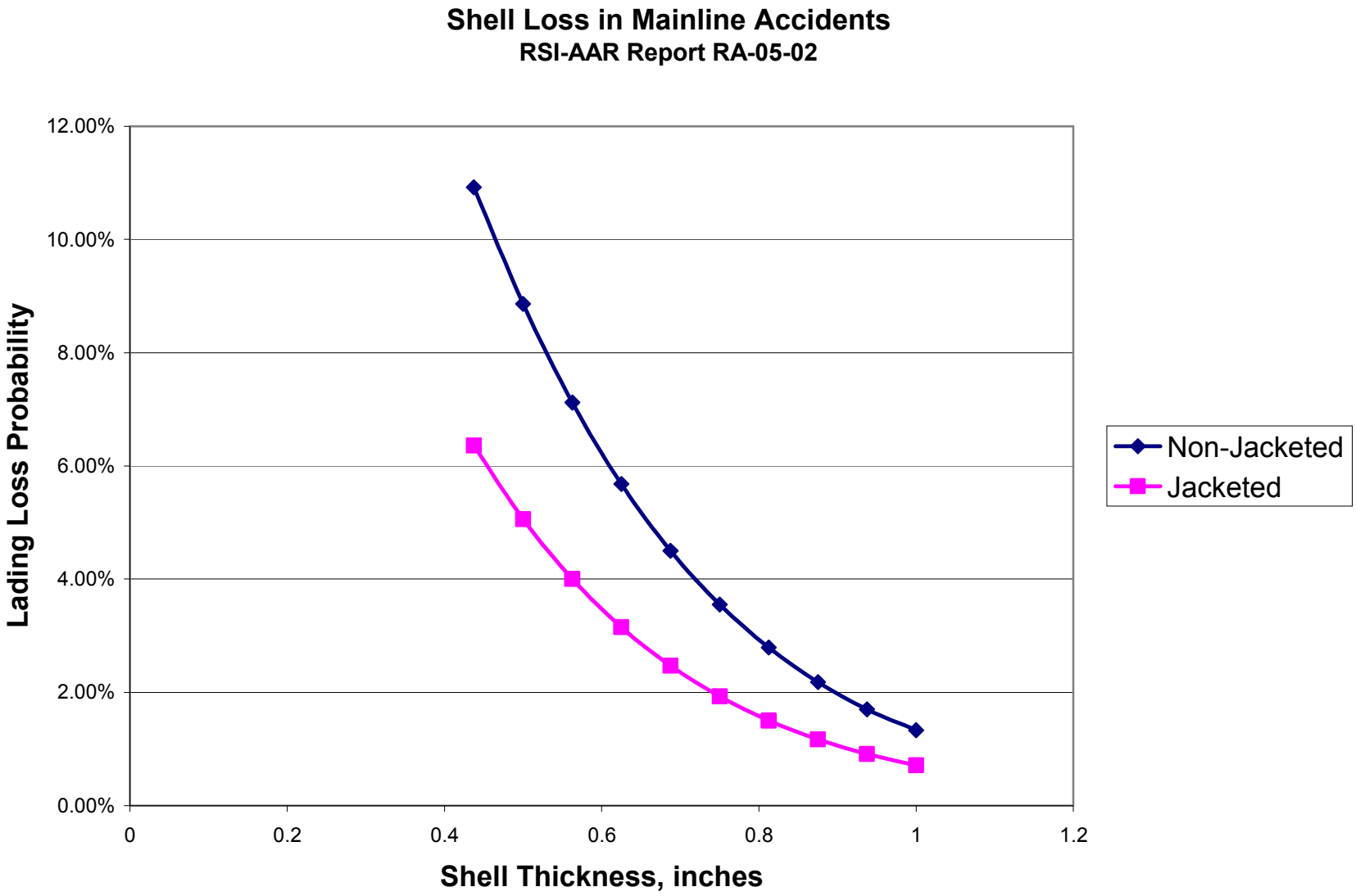

FIGURE 5.9 Effect of shell thickness on lading loss probability, based on regression fits to the RSI-AAR Accident Database. Data taken from RSI-AAR Report RA-05-02 [7].

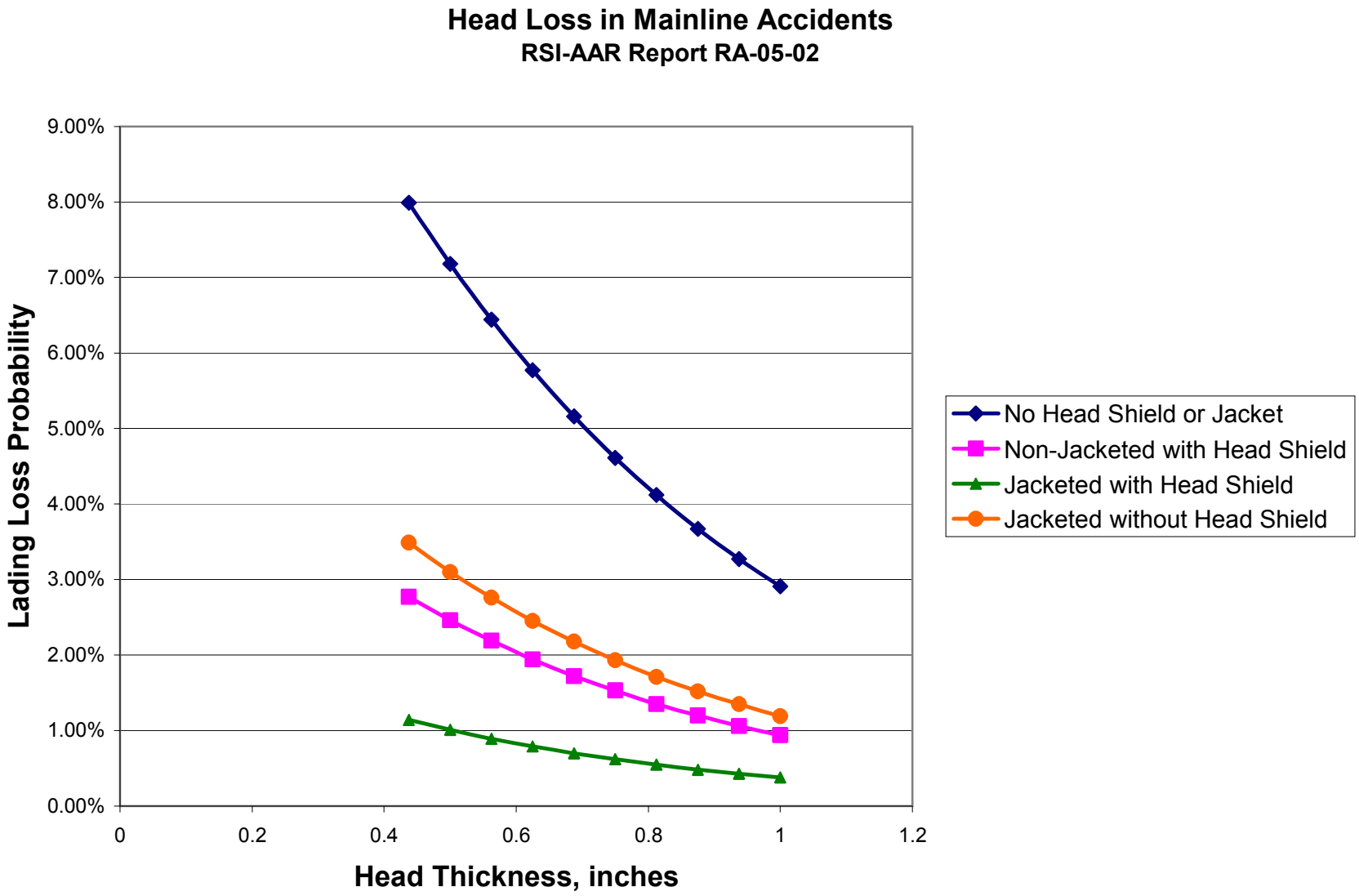

FIGURE 5.10 Effect of head thickness on lading loss probability, based on regression fits to the RSI-AAR Accident Database. Data taken from RSI-AAR Report RA-05-02 [7].

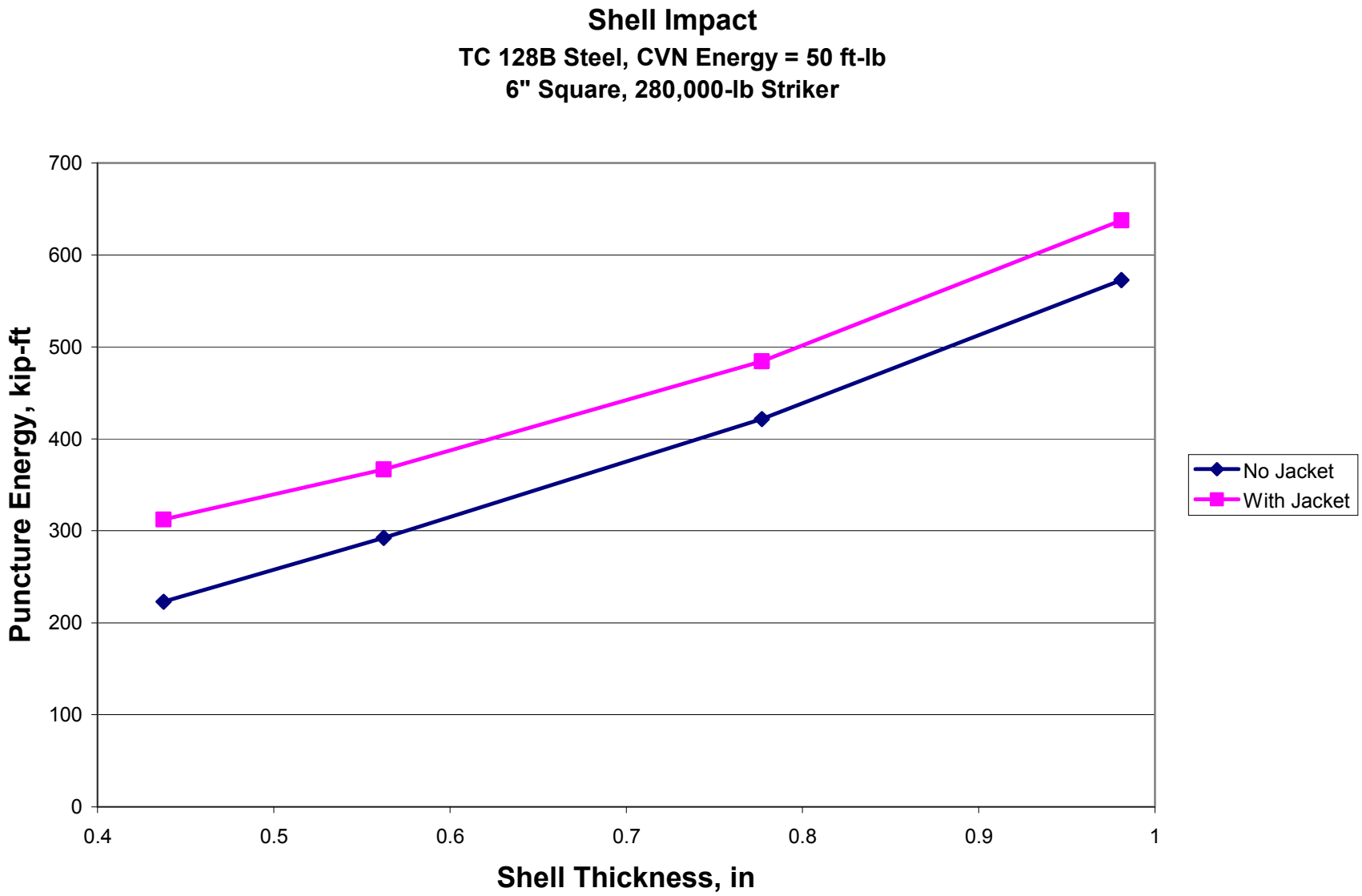

FIGURE 5.11 Effect of shell thickness on puncture energy for a shell impact.

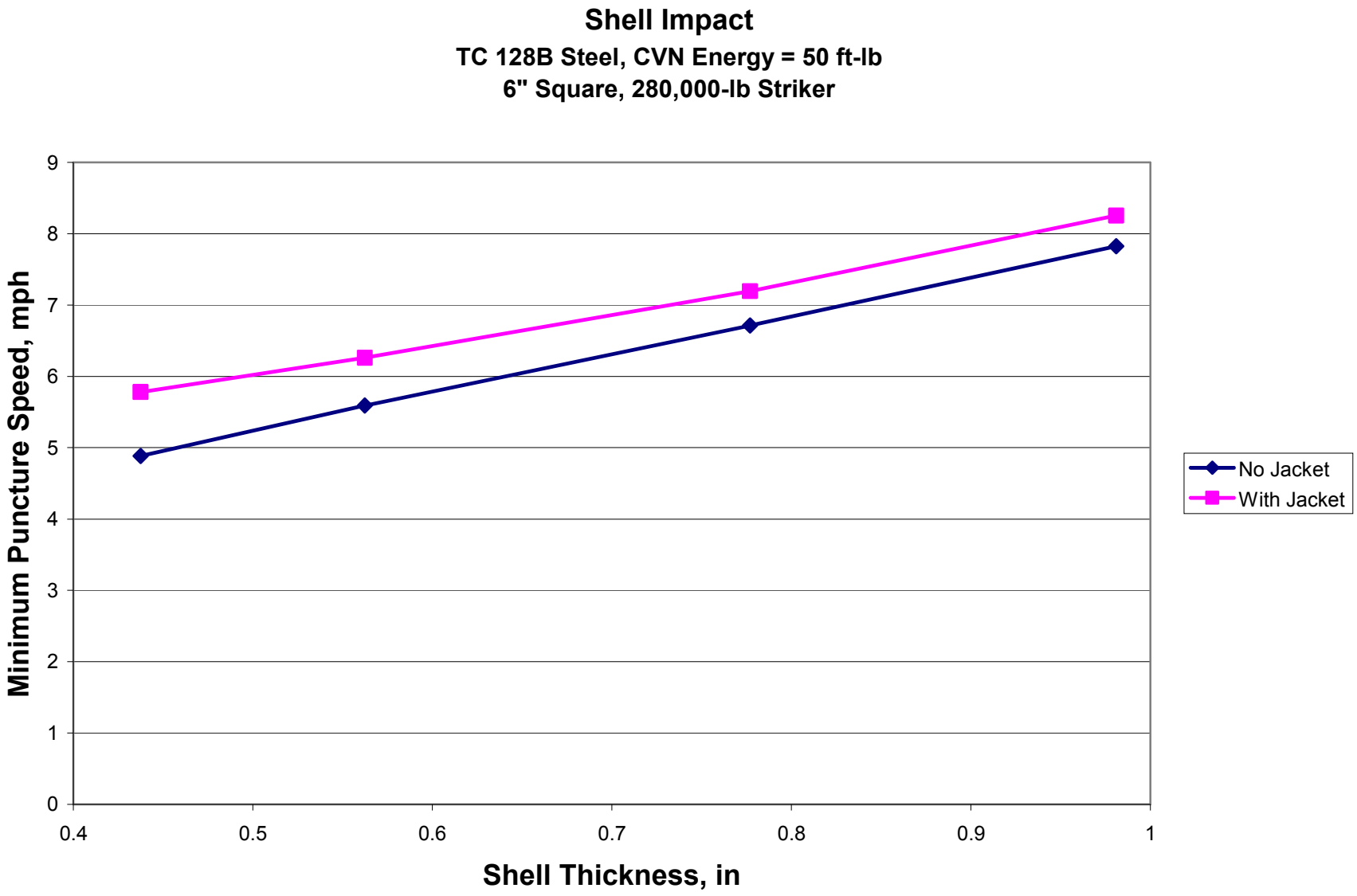

FIGURE 5.12 Effect of shell thickness on minimum puncture speed for a shell impact.

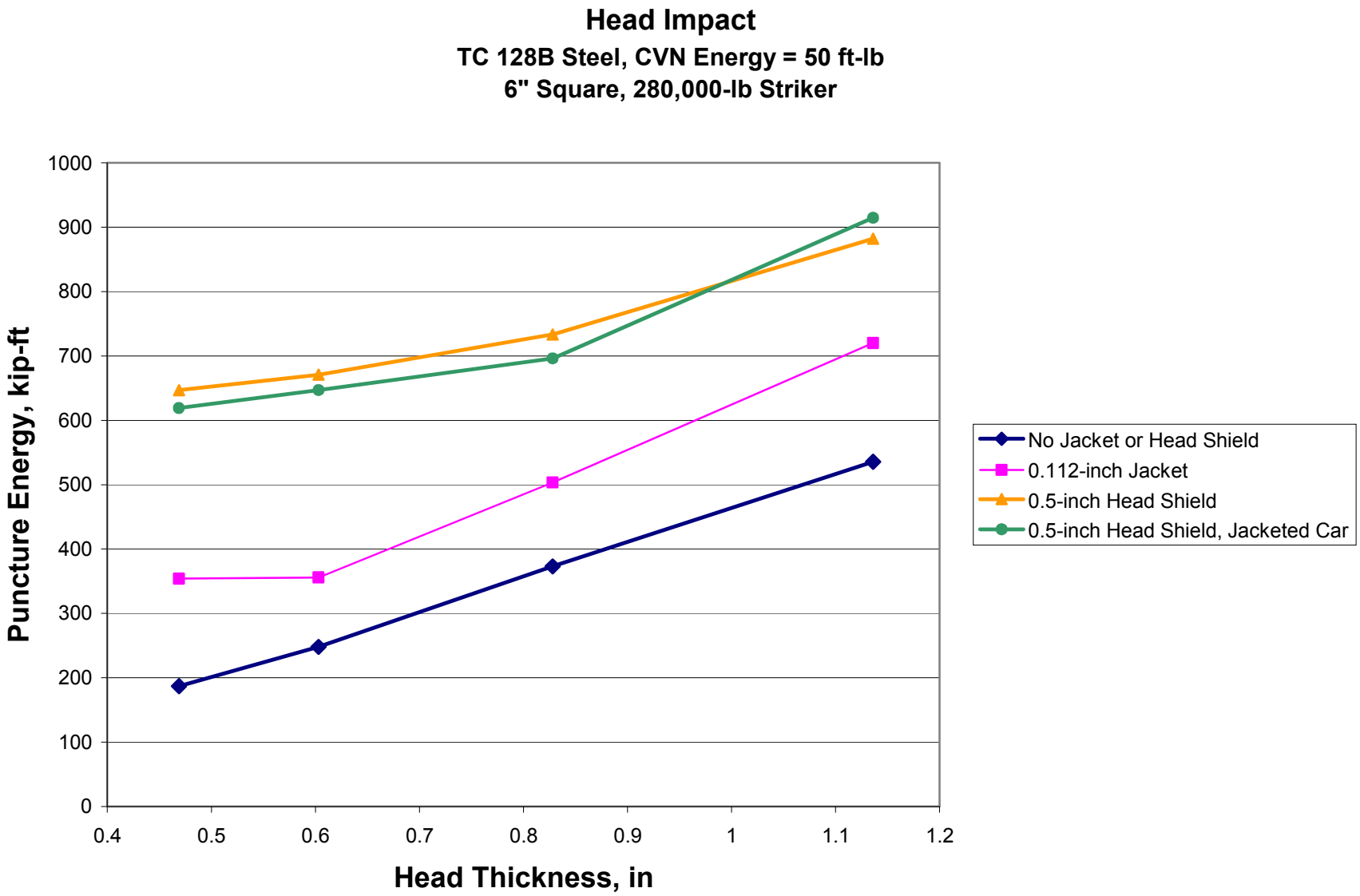

FIGURE 5.13 Effect of head thickness on puncture energy for a head impact.

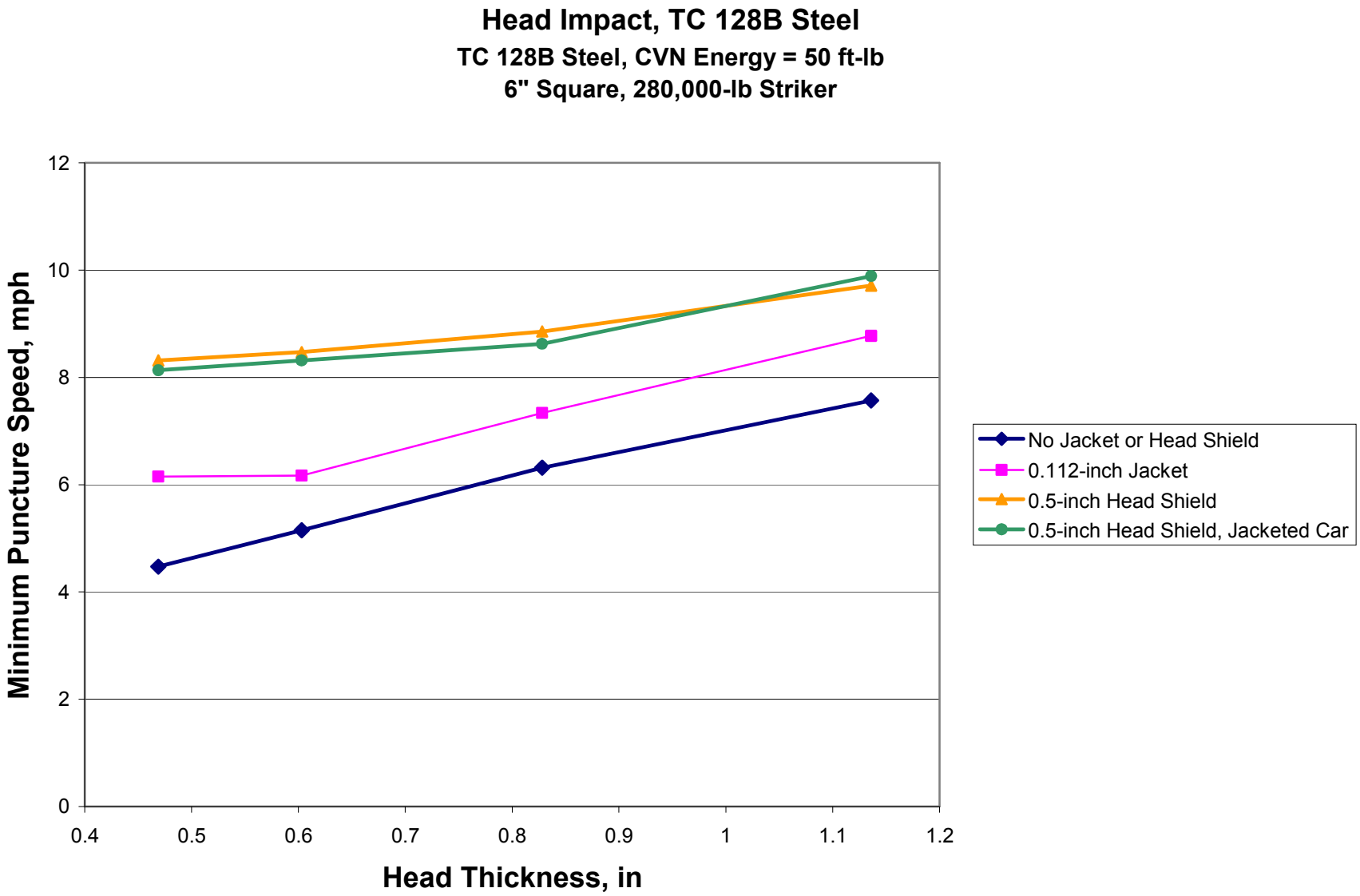

FIGURE 5.14 Effect of head thickness on minimum puncture speed for a head impact.

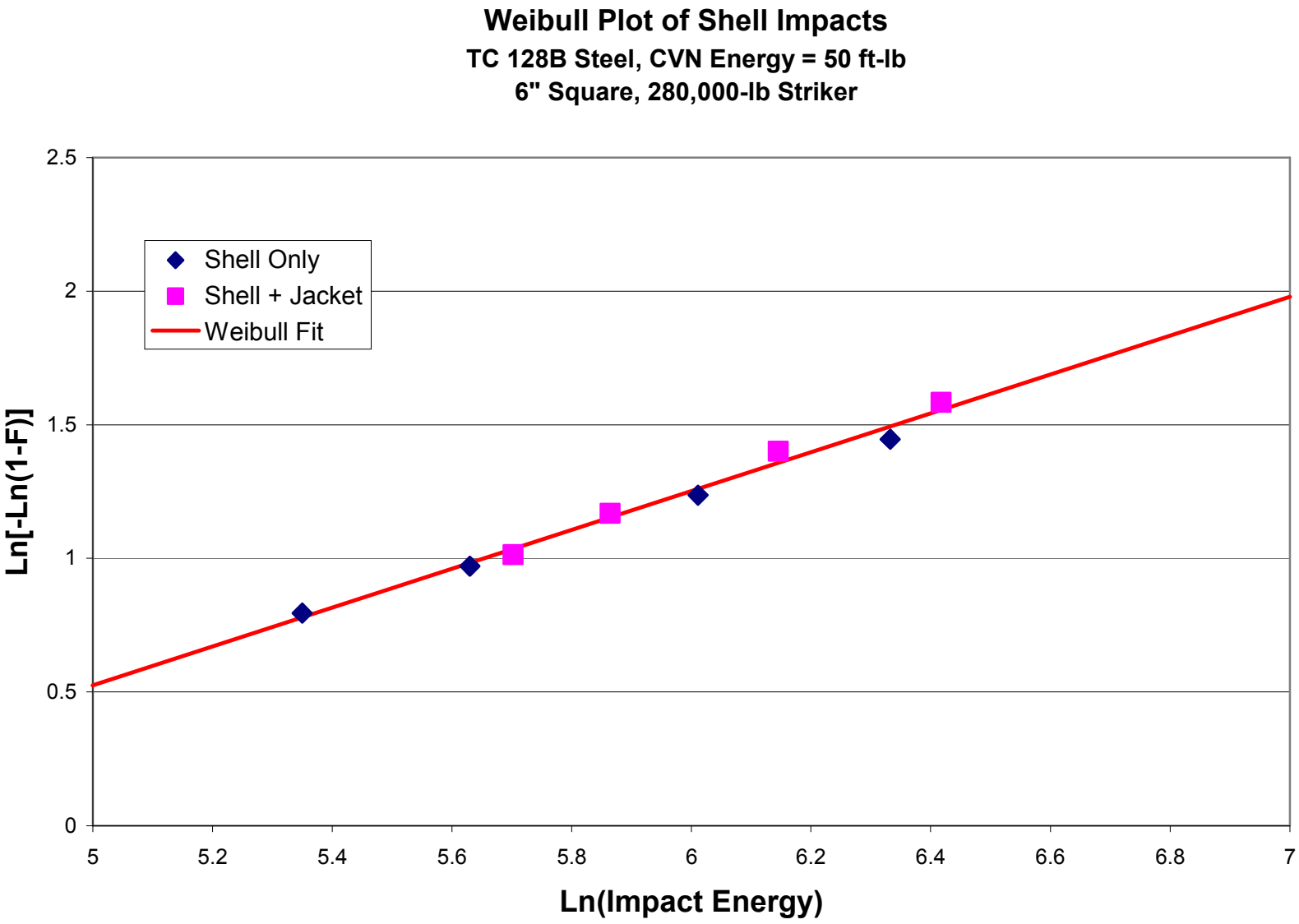

FIGURE 5.15 Weibull fit to shell impact energy, corresponding to the 6-inch striker that weighs 280,000 lb. This plot was constructed from Figs. 9 and 11.

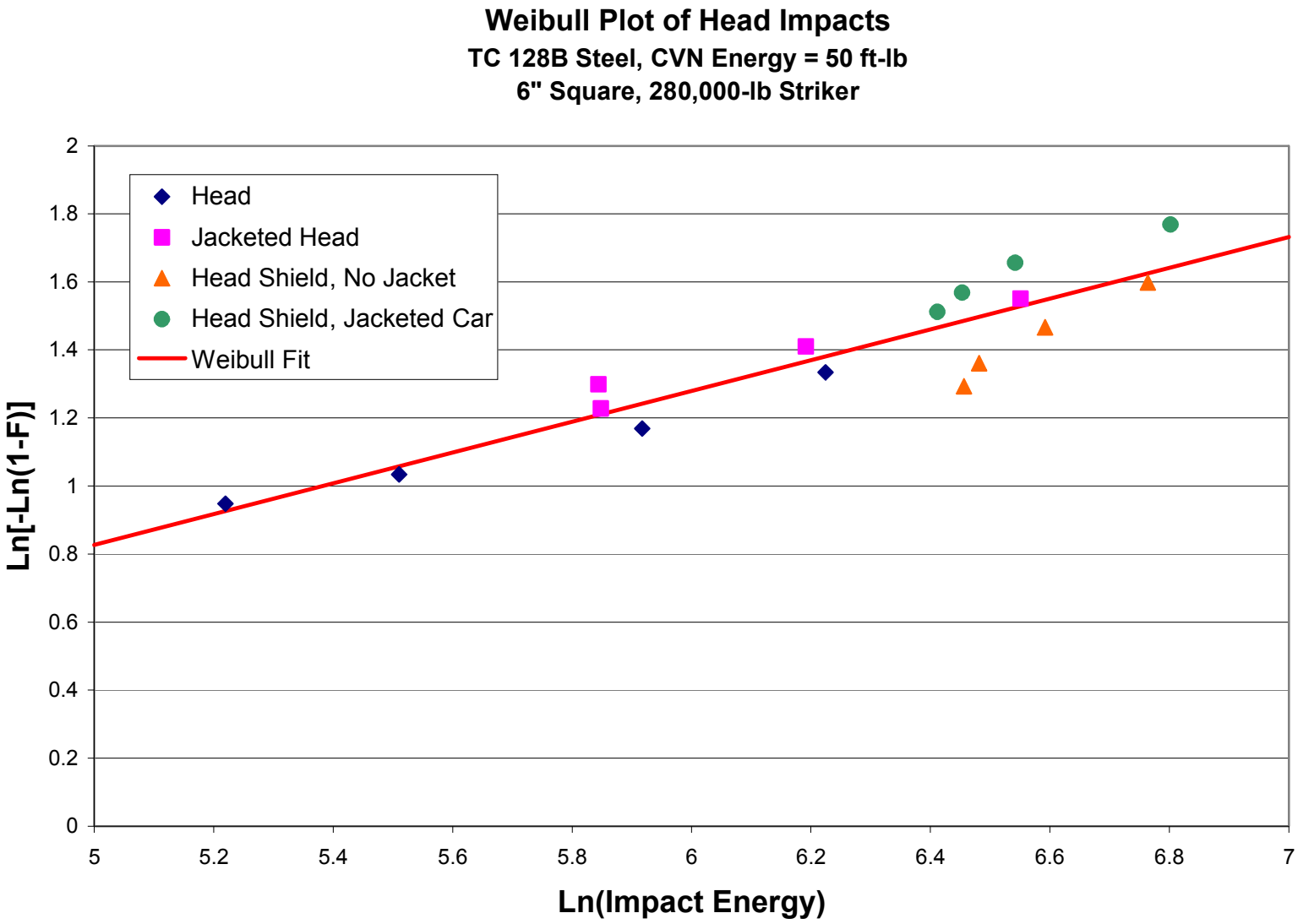

FIGURE 5.16 Weibull fit to head impact energy, corresponding to the 6-inch striker that weighs 280,000 lb. This plot was constructed from Figs. 10 and 12.

5.3 Effect of Material Toughness on Lading Loss Probability

Improvements in toughness should result in improvements in puncture resistance. A series of tank cars impacts were simulated to verify this contention. The effect of improvements in TC 128B steel was evaluated, as well as the effect of switching to modern HSLA steels. Of the HSLA steels tested in this study, HPS 100 exhibits the best toughness. As a result, this steel was evaluated in a series of finite element simulations of tank car impacts.

Figures 5.17 and 5.18 are plots of puncture energy and minimum puncture speed, respectively, versus shell thickness for TC 128B and HPS 100 steel. For the former material, A Charpy energy of 50 ft-lb was assumed, which conforms to the assumed toughness of the existing fleet (Section 5.2). For the HPS 100 steel, a Charpy energy of 185 ft-lb was used in the simulations. These analyses predict more than a two-fold improvement in puncture energy with HPS 100 steel relative to the existing fleet.

Equation (5.5) can be used to predict the effect of material toughness on lading loss probability. Figure 5.19 is a plot of probability of lading loss versus thickness for the two materials. For thicker shells, there is more than a ten-fold reduction in lading loss probability when HPS 100 steel is compared to a 50 ft-lb TC 128B material.

Puncture energy and lading loss probability can also be improved by increasing the toughness of TC 128B steel, as Figs. 5.20 to 5.22 illustrate. Modern low-sulfur steels with sulfide shape control have significantly improved upper-shelf toughness relative to the existing fleet. Thus even in the absence of mandated changes to tank car steel specifications, the overall lading loss probability should improve over time as older cars are retired and new cars are built.

Tables 5.2 and 5.3 show a comparison between the puncture resistance of 50 ft-lb TC 128B steel and 185 ft-lb HPS 100 steel for a chlorine car (105J500W). The six scenarios listed in Table 4.2 were considered. As is the case with Figs. 5.17 to 5.22, the potential improvement is significant, particularly when defined in terms of lading loss probability for shell impacts. An approximately 2:1 improvement in puncture energy is predicted for all six scenarios, but the predicted improvement in lading loss probability is much greater for shell impacts than it is for head impacts.

Note that the six scenarios considered above assumed that the head, shell, jacket, and head shield in a given case were all made from the same material. In reality, the jacket and head shield are not necessarily made from the same material as the head and shell. The assumption of a single material was made for convenience. Simulations that included multiple materials gave anomalous results, and we were unable to resolve this numerical difficulty within the time frame of the project. Given that the jacket has a modest effect on the puncture resistance (e.g., see Fig. 4.15), the assumed toughness properties of the jacket are of relatively minor importance for shell impacts. In the case of head impacts, our results correspond to the scenario in which *both* the head and head shell are made with a tougher steel. If only one of these components is made with a toughness material, the puncture resistance will fall between the extremes of both components made from either a conventional carbon steel or a tough HSLA steel.

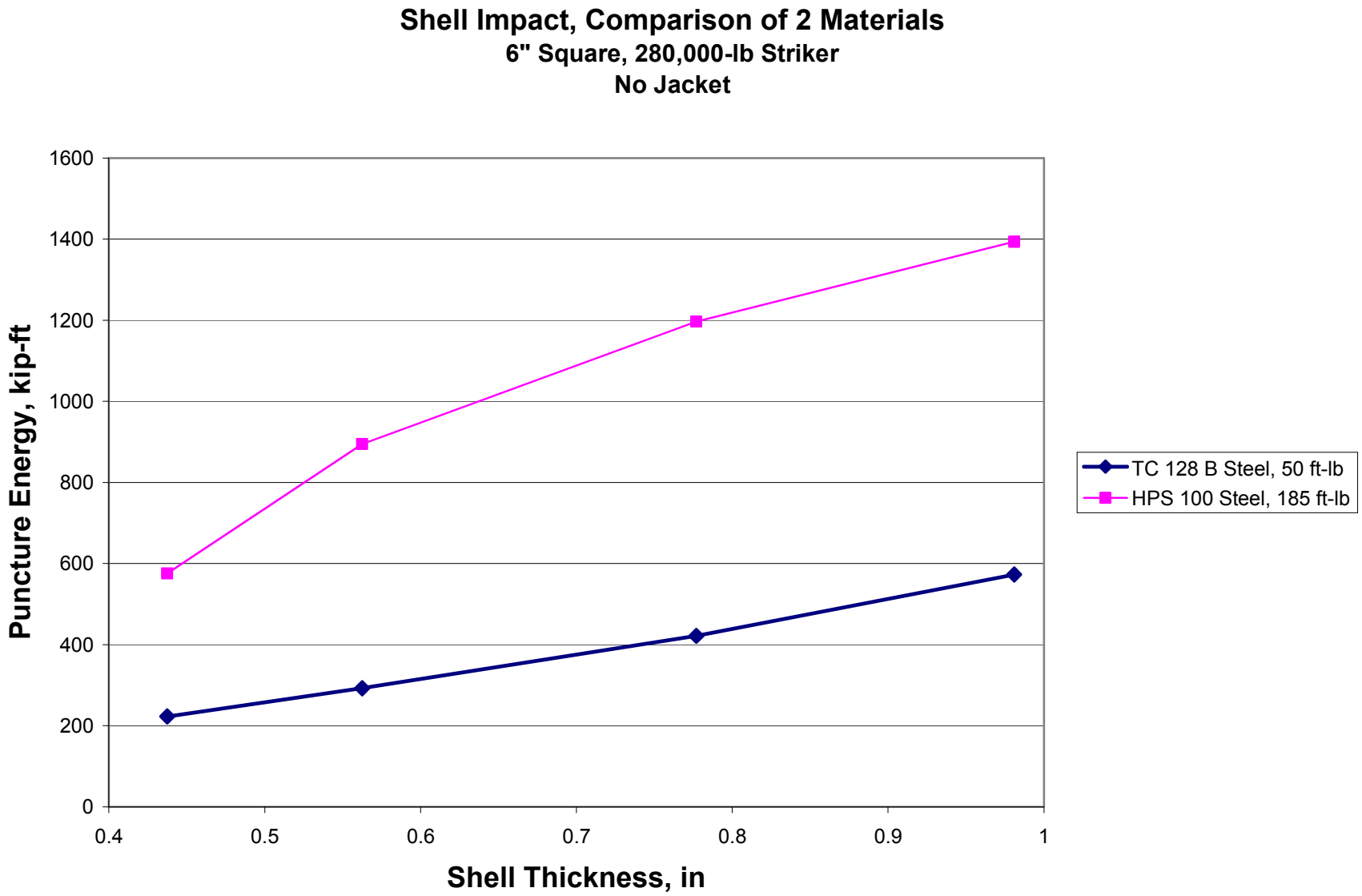

FIGURE 5.17 Effect of shell thickness and material toughness on puncture energy for a shell impact.

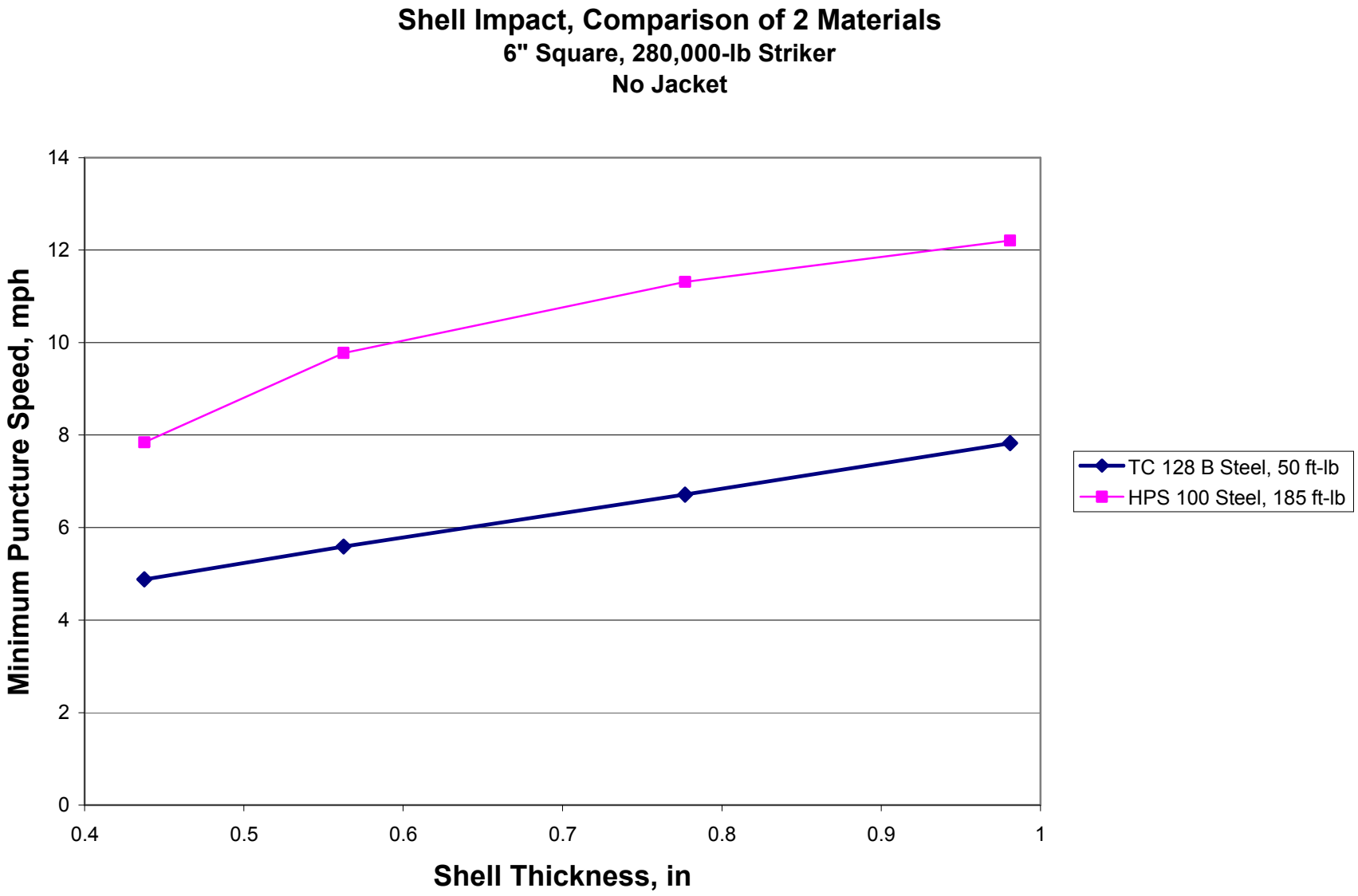

FIGURE 5.18 Effect of shell thickness and material toughness on minimum puncture speed for a shell impact

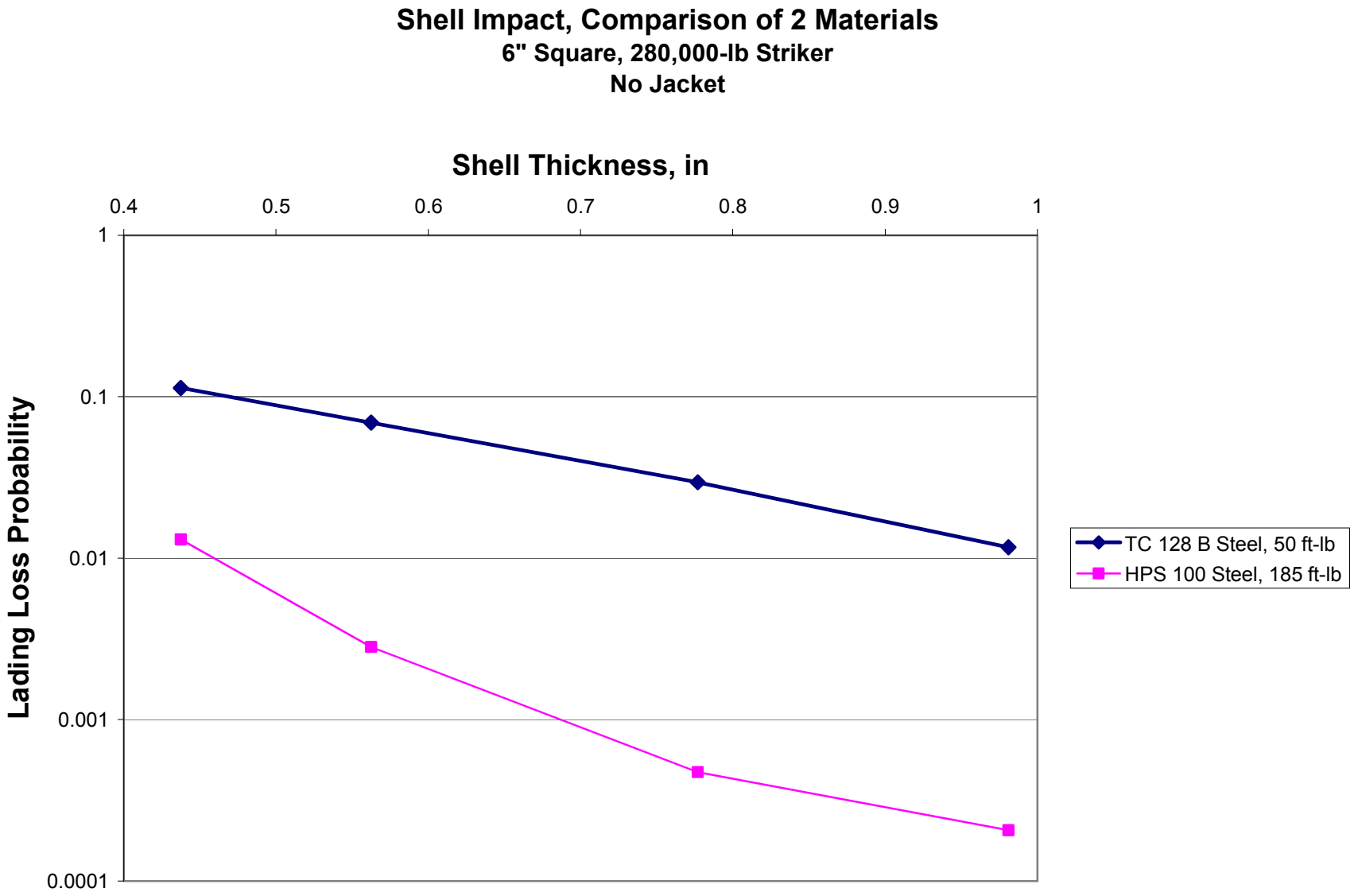

FIGURE 5.19 Effect of shell thickness and material toughness on lading loss probability, as computed from Fig. 5.17 and Eq. (5.5).

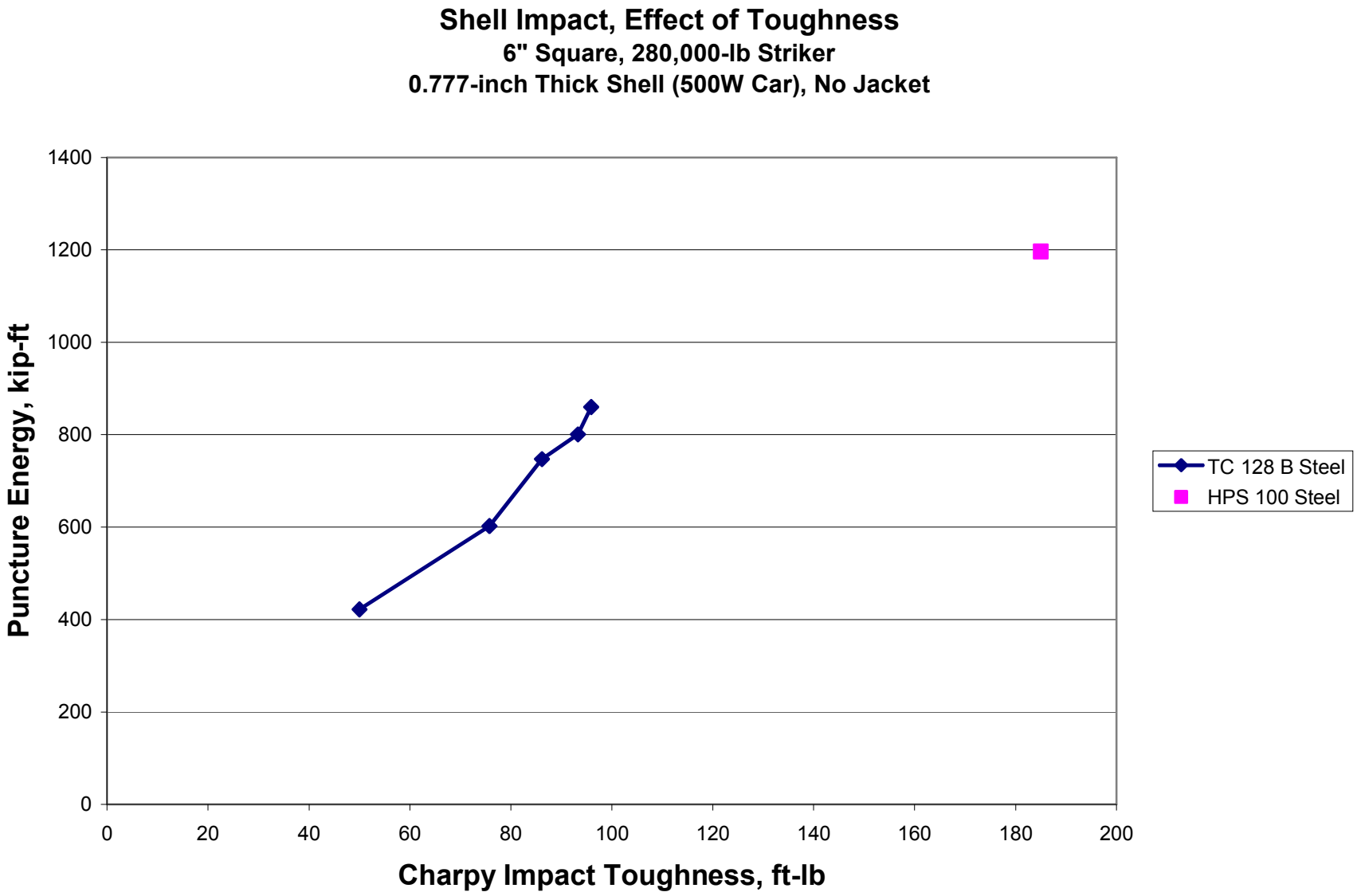

FIGURE 5.20 Effect of toughness on puncture energy for a shell impact.

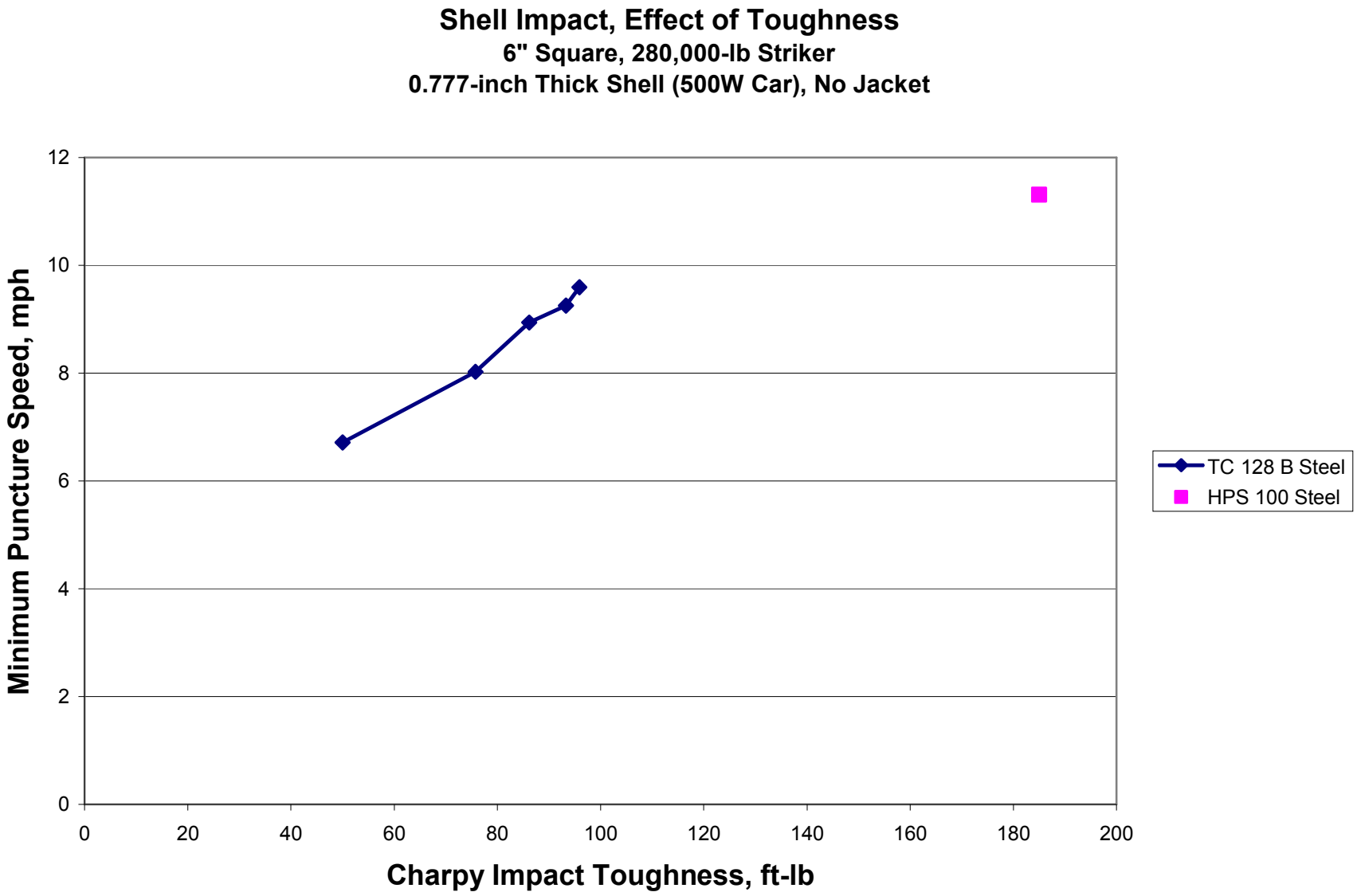

FIGURE 5.21 Effect of toughness on minimum puncture speed for a shell impact.

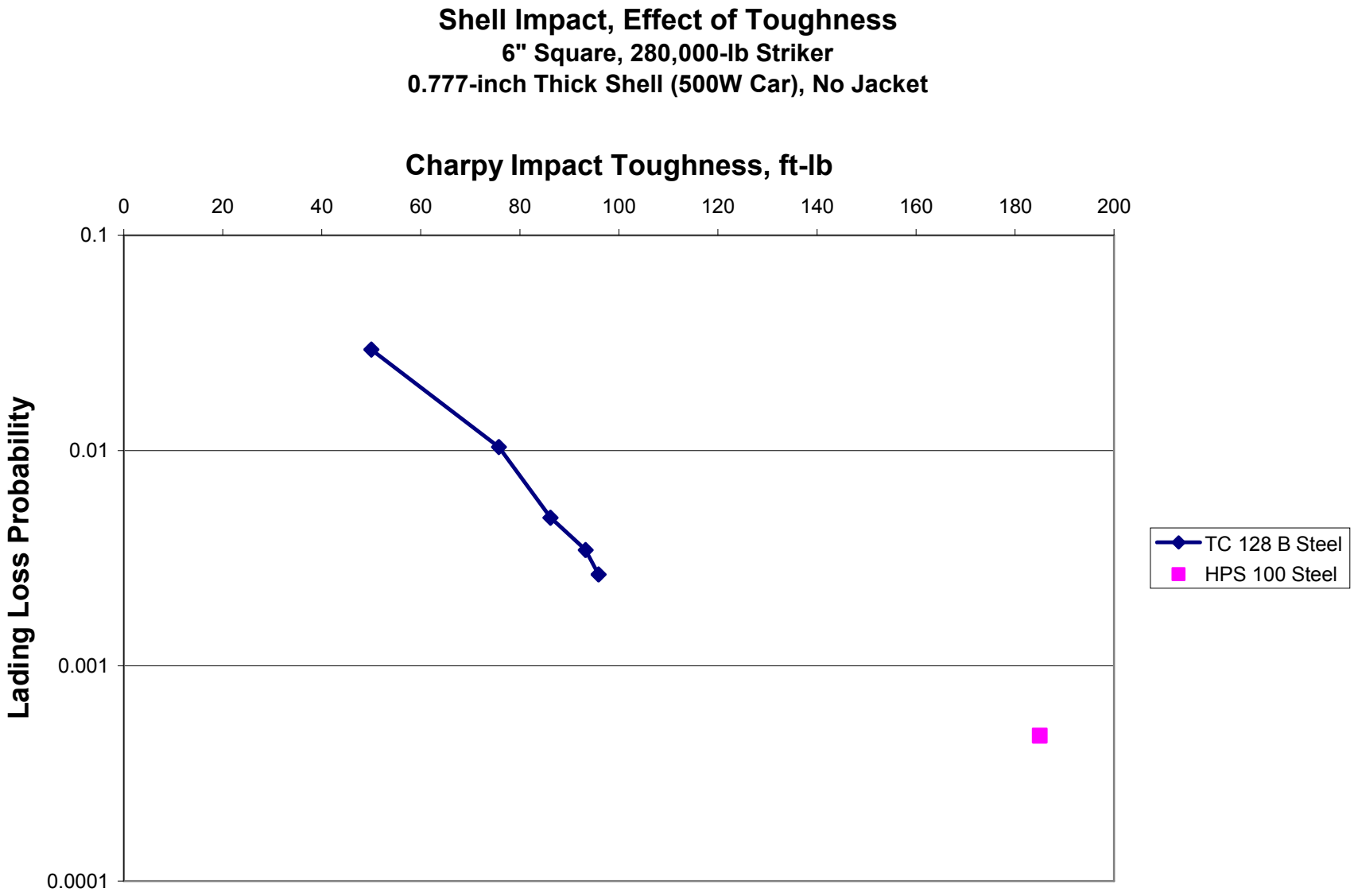

FIGURE 5.22 Effect of material toughness on lading loss probability, as computed from Fig. 5.17 and Eq. (5.5).

TABLE 5.2
Effect of design features and material toughness on puncture resistance in a 105J500W tank car .

Impact Location	Jacket/Head Shield*	Puncture Energy, kip-ft		Minimum Puncture Speed, mph		Estimated Lading Loss Probability	
		TC 128 B 50 ft-lb	HPS 100 185 ft-lb	TC 128 B 50 ft-lb	HPS 100 185 ft-lb	TC 128 B 50 ft-lb	HPS 100 185 ft-lb
Shell	Bare Shell	422	1197	6.7	11.3	2.94×10^{-2}	4.73×10^{-4}
	0.112" Jacket	484	1304	7.2	11.8	2.05×10^{-2}	3.57×10^{-4}
Head	Bare Head	373	691	6.3	8.6	3.13×10^{-2}	1.02×10^{-2}
	0.112" Jacket	503	1009	7.3	10.4	1.98×10^{-2}	4.76×10^{-3}
	0.5" Head Shield, No Standoff	733	1594	8.9	13.1	9.10×10^{-3}	1.31×10^{-3}
	0.5" Head Shield, with Standoff	696	1434	8.6	12.6	1.01×10^{-2}	1.69×10^{-3}

*In these analyses, the jacket and head shield material was assumed to be the same as for the shell and head.

TABLE 5.3
Relative Improvement Computed from Table 5.2

Impact Location	Jacket/Head Shield*	Predicted Improvement from Switching to HPS 100 Steel (185 ft-lbs CVN) from TC 128B Steel (50 ft-lb CVN)		
		Puncture Energy	Minimum Puncture Speed	Lading Loss Probability
Shell	Bare Shell	284%	169%	62 Times Lower
	0.112" Jacket	269%	164%	57 Times Lower
Head	Bare Head	185%	137%	3.1 Times Lower
	0.112" Jacket	201%	142%	4.2 Times Lower
	0.5" Head Shield, No Standoff	217%	147%	6.9 Times Lower
	0.5" Head Shield, with Standoff	206%	147%	6.0 Times Lower

5.4 Benchmarking to Full-Scale Test Results

The Next Generation Rail Tank Car Project, which is organized by Dow, Union Pacific and Union Tank Car, has been working in parallel with this project to study improvements in tank car puncture resistance. The Next Generation Project recently completed a full-scale puncture test of a 105J500W tank car at the Transportation Technology Center, Inc. (TTCI) in Pueblo, Colorado. This was actually the second test performed at TTCI for the Next Generation Project. The first test was preliminary, and did not result in a puncture. One of the authors of this report (SWK) has performed finite element simulations of these tests under the auspices of the Next Generation Project.

The second test was very similar to the collision scenarios assumed in the finite element simulations presented in this report. A bullet car weighing 286,000 lb struck the shell of the target car at the equator and midpoint along the length (as in Fig. 4.1). The striker was 6 in x 6 in, with a 0.5-in chamfer radius, which is identical to the striker used for most of the simulations in the present study. The initial speed of the bullet car was 15.1 mph.

Mechanical testing was performed on the shell material following the test. Table 5.4 lists the measured tensile and Charpy properties.

The second test from the Next Generation Project was simulated in the present study using the procedures outlined in Section 4. Lading mass and friction effects were incorporated into the model, and the actual initial collision speed of 15.1 mph was used. The initial simulation of this test was conducted before material testing was completed, so a Charpy toughness of 50 ft-lb was assumed. The subsequent mechanical testing indicated that the shell material actually had a mean Charpy energy of 106 ft-lb in the transverse direction, so the simulation was repeated with Gurson-Tvergaard coefficients that correspond to this higher toughness.

Figure 5.23 is a plot of energy versus time for the actual and simulated tests. Both simulations match the experiment very well up to the point of puncture, which indicates that the simulations accurately modeled the deformation of the tank car in the impact zone. The initial simulation that assumed a 50 ft-lb Charpy energy significantly under-predicted the puncture energy in the test. When the simulation was repeated with the actual material toughness, however, the prediction matched the experiment to within a few percent. Minimum puncture speeds of 11.1 and 10.6 mph were inferred for the experiment and simulation, respectively.

Figure 5.24 is a photograph of a section of the tank car shell that was removed after the test. When the 6-inch striker penetrated the shell, a small flap of steel rotated inward. A larger opening was created when the fixturing to which the striker was attached penetrated the shell. The events that followed the initial puncture resulted in energy dissipation, which is why the experimental energy v. time trend in Fig. 5.23 has a positive slope after the knee in the curve.

Typical simulations of collision and puncture events do not predict the inward rotation of a flap, as seen in Fig. 5.24. Rather, square piece is punched through the shell, as Figs 4.7 to 4.14 illustrate. This is because compute simulations normally assume perfect symmetry and material homogeneity. In an actual experiment, the collision is not perfectly orthogonal and the material is not perfectly homogeneous. In order to assess the effect of a slight deviation from perfect

symmetry, we performed an additional simulation of the Next Generation Test #2 in which the striker was oriented 2^o from orthogonal to the shell. That is, the striker impacted the mid point of a shell at an angle of 88^o. This caused fracture to initiate on only one side of the striker, which in turn created a flap somewhat like that shown in Fig. 5.24. The puncture energy was not significantly affected by the 2^o offset from perpendicular.

Table 5.4
Measured tensile and fracture toughness properties for Car 3074 in test no. 2

Specimen Orientation	UTS, ksi	YS, ksi	Elong, %	RA, %	CVN, ft-lbs
L	81.7	55.0	34	68	132
	80.8	55.1	34	70	122
	80.7	52.3	32	71	154
average =	**81.1**	**54.1**	**33.3**	**69.7**	**136**
T	81.2	58.9	32	68	104
	81.3	57.4	33	69	110
	81.1	56.9	33	66	103
average =	**81.2**	**57.7**	**32.7**	**67.7**	**106**

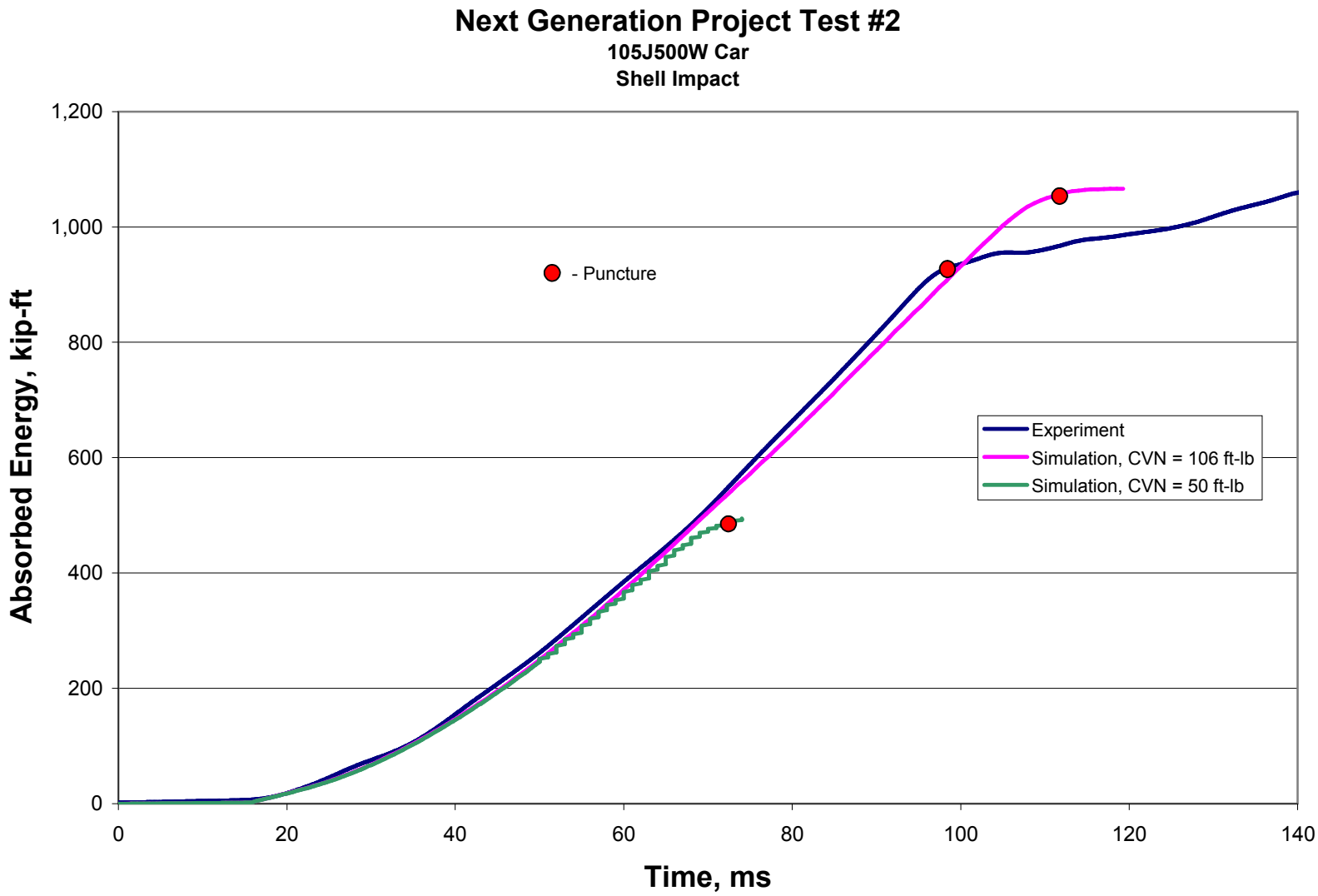

FIGURE 5.23 Comparison of predicted and measured energy curves for Test # 2, performed as part of the Next Generation Project.

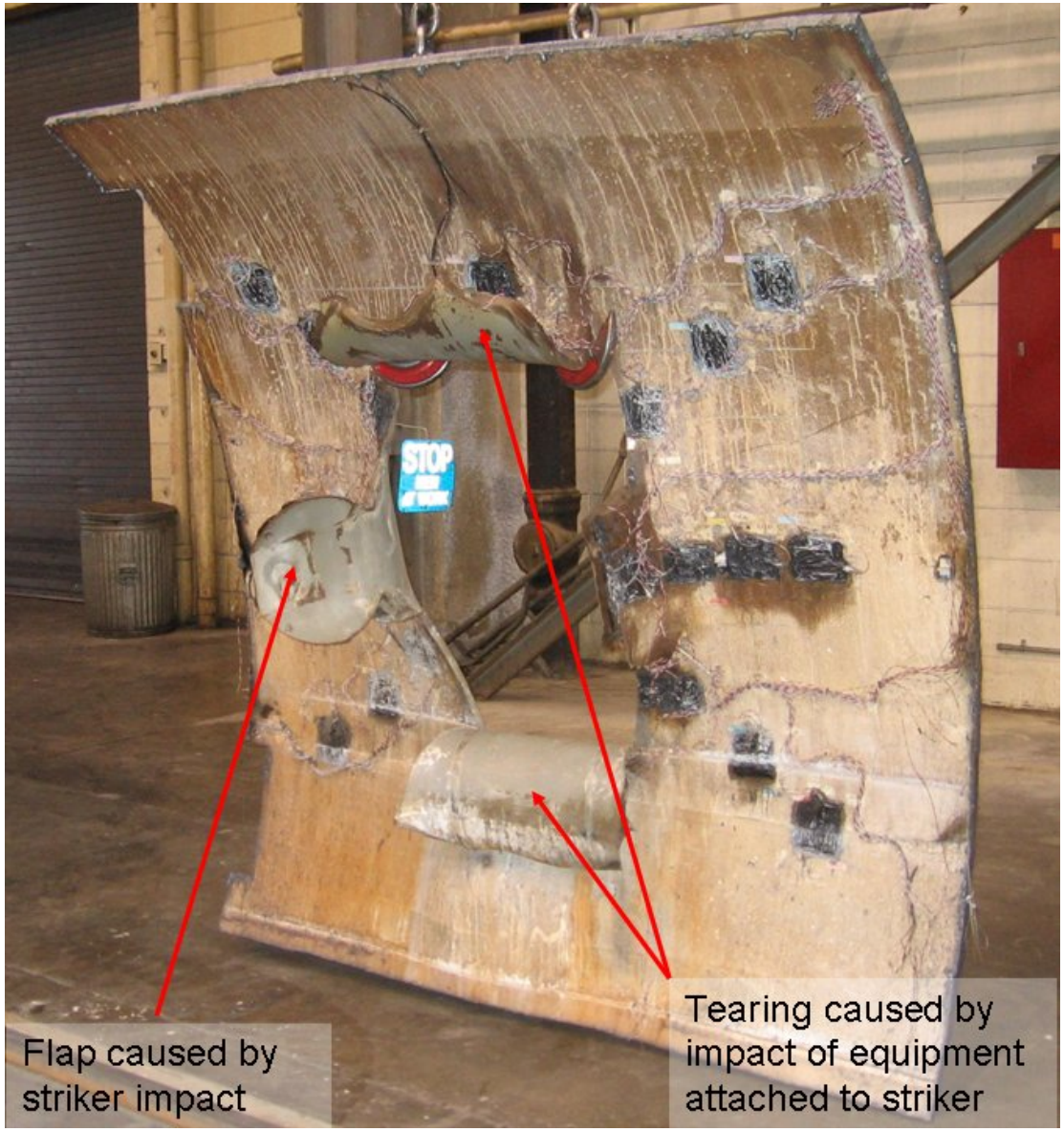

FIGURE 5.24 Experimental Test # 2, performed as part of the Next Generation Project. Cut out of impact zone.

6 DISCUSSION OF RESULTS

Overall, the computer simulation methodology developed in this project appears to be an effective tool for charactering puncture resistance in tank cars as a function of material properties and design parameters. There are some practical implications of this work, as well as a number of unresolved issues. Several of these topics are addressed below.

6.1 Triaxiality and Fracture Models

The Volpe National Transportation Systems Center has been performing simulations of dynamic collision, fracture, and puncture using the Bao-Wierzbicki material model [8-10]. The present project, as stated earlier, uses the Gurson-Tvergaard ductile fracture model. There has been some discussion among individuals associated with Volpe, the Next Generation Project, and this project as to which material model is better suited for simulation of puncture in tank cars. A definitive answer to this question would require an extensive comparative study of the two models, which is beyond the scope of this project. However, some qualitative comparisons are possible.

Both the Gurson-Tvergaard and Bao-Wierzbicki models purport to account for the effect of stress triaxiality on ductility. The former is a continuum damage model that captures the formation and growth of microscopic voids. The Bao-Wierzbicki model is purely empirical. When *any* failure model is incorporated into finite element analysis, where elements are deleted when a failure criterion is reached, the analysis must deal with length scale effects. This can be accomplished either by tuning the model to the specific mesh refinement or by introducing a length scale into the model. We applied the former approach in this study, and Volpe apparently uses the latter approach. When a length scale is introduced into a failure model to avoid mesh dependence, a convergence study should be performed to prove that the results are, in fact, mesh insensitive.

Figure 6.1 schematically compares the two models. The strain at fracture is plotted against the triaxiality ratio, which defined as follows

$$T = \frac{\sigma_m}{\sigma_e} \tag{6.1}$$

where σ_m is the *mean stress*, which is the average of the three principal normal stresses:

$$\sigma_m = \frac{\sigma_1 + \sigma_2 + \sigma_3}{3} \tag{6.2}$$

and σ_e is the von Mises stress, which is given by

$$\sigma_e = \frac{1}{\sqrt{2}}\left[\left(\sigma_1 - \sigma_2\right)^2 + \left(\sigma_1 - \sigma_3\right)^2 + \left(\sigma_2 - \sigma_3\right)^2\right]^{1/2} \tag{6.3}$$

The Gurson-Tvergaard model, which is based on growth of microvoids, predicts that the strain at fracture monotonically increases with decreasing triaxiality. According to the Bao-Wierzbicki model, the ductility decreases between $T = {}^1/_3$ and $T = 0$, where $T = {}^1/_3$ corresponds to uniaxial tension. The Gurson-Tvergaard model can be tuned to match the Bao-Wierzbicki model for triaxiality greater than or equal to ${}^1/_3$, but the two models obviously diverge for $T < {}^1/_3$. Thus a critical issue as to the appropriateness of either or both models is whether puncture initiates by tensile fracture, where $T > {}^1/_3$, or if puncture is shear dominated, and $T < {}^1/_3$.

Figure 6.2 shows the time history of triaxiality of elements at or near the fracture origin in BFCM specimens and the simulation for the Next Generation Project test #2. In all cases, $T > {}^1/_3$, which indicates that either material model might be suitable to predict puncture. Note that the triaxiality decreases with increasing thickness in the BFCM specimens, and that the triaxiality in the thinnest specimens is most representative of the stress state in the tank car prior to puncture.

Although the low-triaxiality regime is apparently not important in puncture events, there are other important differences in the two models. For a given material, the two models can be tuned to give identical predictions in the tensile fracture regime. However, the two models appear to predict different levels of sensitivity to Charpy toughness. The Gurson-Tvergaard model predicts a strong relationship between Charpy toughness and puncture resistance, as Fig. 5.23 illustrates. The Volpe studies have not included simulations of Charpy tests, so the precise effect of toughness on puncture resistance, as predicted by the Bao-Wierzbicki model, has not been quantified. However, there is limited indirect evidence that Bao-Wierzbicki failure locus (Fig. 6.1) is not a strong function of upper shelf toughness. Further work is needed to understand which model provides more accurate predictions over a range of materials.

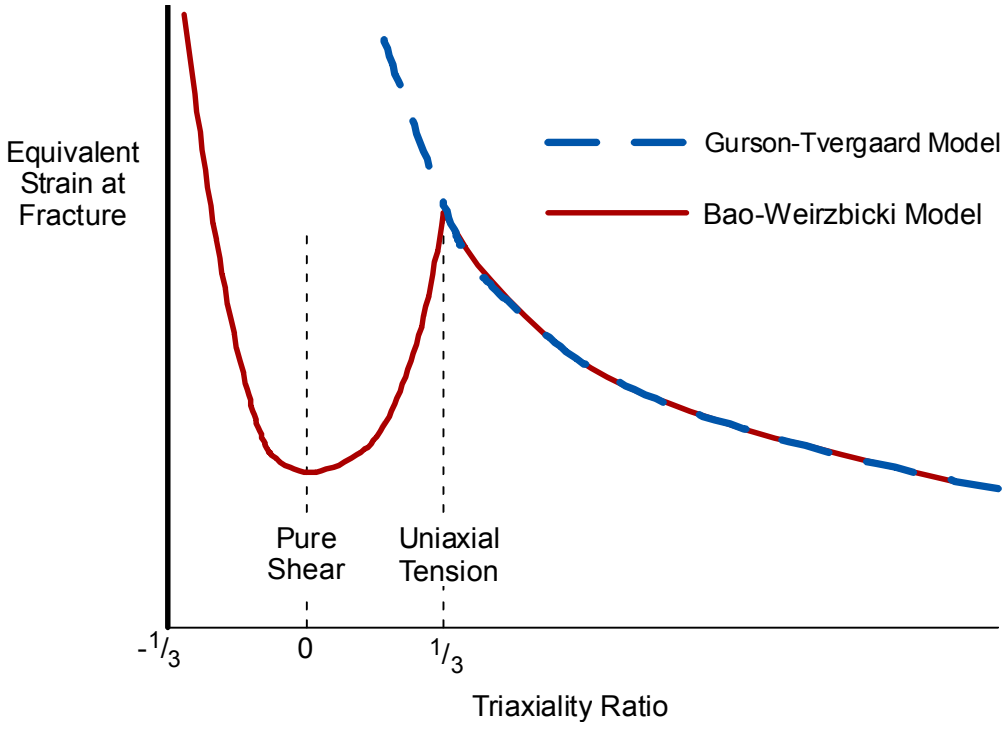

FIGURE 6.1 Schematic comparison of two ductile fracture models.

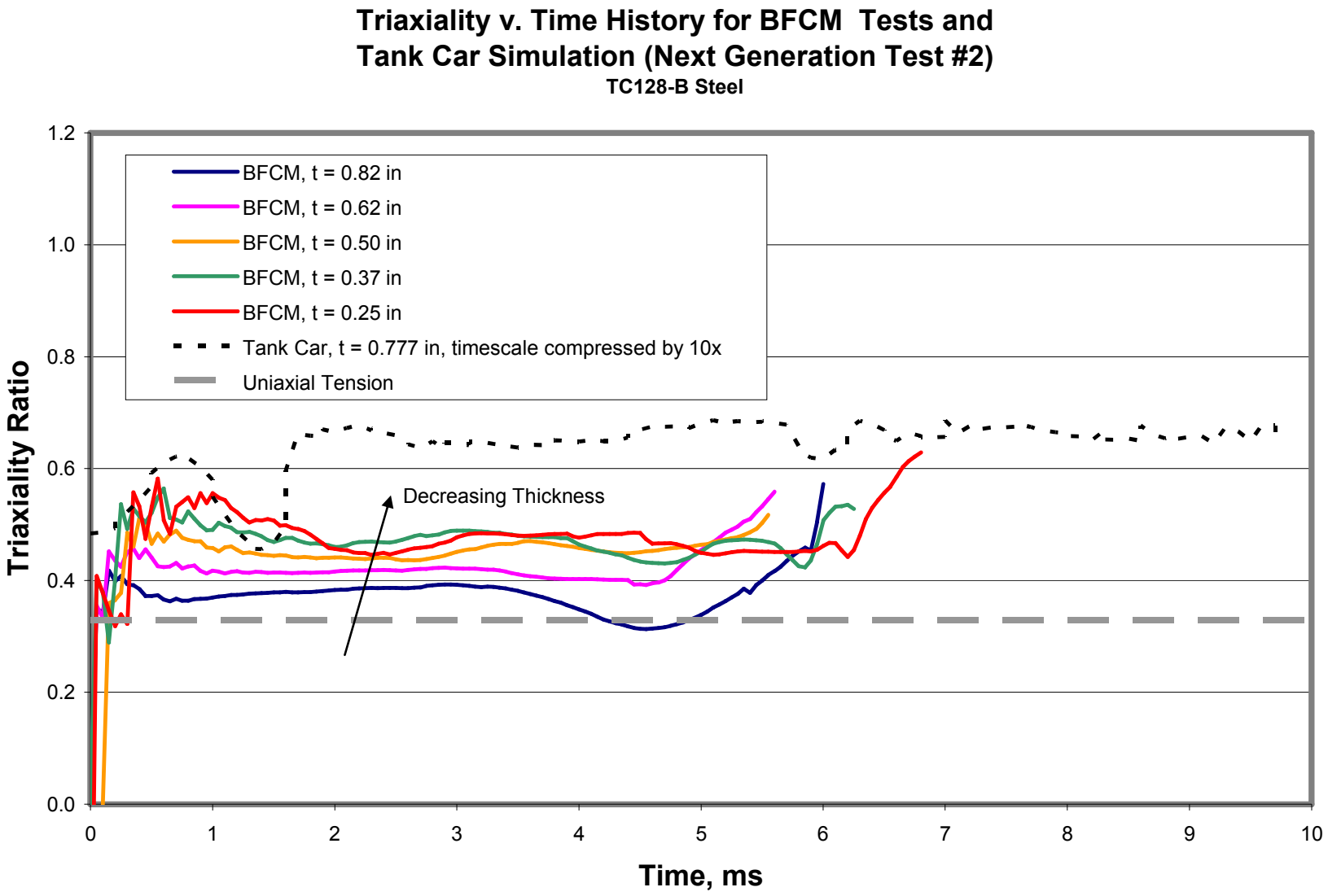

FIGURE 6.2 Triaxiality at the fracture origin in BFCM specimens and the Next Generation Project test #2.

6.2 Effect of an Energy-Absorbing Insulation Layer

At the request of The Chlorine Institute, we estimated the increase in energy absorption resulting from a layer of metal foam between the tank shell and jacket. Figure 6.3 illustrates the concept of an energy-absorbing insulation layer. When a jacketed car is impacted, there are three stages. In the first stage, the jacket and insulation layer collapse into the shell. For a conventional tank car design, minimal energy is absorbed in Stage 1, as Fig. 5.23 indicates. An energy-absorbing material, such as metal foam, could provide energy dissipation in Stage 1. In Stages 2 and 3, which involve deformation and puncture of the shell, respectively, the behavior during would not likely be affected by the insulation layer. Thus the overall increase in puncture energy would be governed by the additional energy absorption during Stage 1.

Metal foam is a product designed for acoustic and thermal insulation. It also has good energy absorption in crushing applications such as in automobiles in which a hollow compression member is filled with metal foam. During a crash event, the compression member and the metal foam crushes, thereby fully engaging the foam's crushing-absorption capabilities. However, for tank cars, the primary resisting mechanism is flexure & catenary tension, which does not directly engage the foam's crushing-absorption capabilities.

We estimated the energy absorption by examining the crushing of metal foam between the jacket and shell within the striker foot-print. Using this rough estimate, we inferred the increase in energy absorption due to installation of metal foam. We considered an aluminum metal foam product, *Alporas* produced by Shinko Wire Company, which is intended for structural energy absorption.

We assumed metal foam replaces the 4 inch insulation layer between the shell and the jacket. The energy required to crush the metal foam underlying the striker impact area (6 in x 6 in) is 2 kip-ft or approximately 0.2% of the puncture energy for in the Next Generation Project test #2. In a puncture event, the zone of crushed foam will be larger than the striker footprint and energy will also be absorbed by flexure of the foam. Therefore, the additional energy absorption due to metal foam installation might range from 1 to 5% of the total puncture energy in the absence of metal foam. Therefore, this particular metal foam product likely will not significantly increase energy absorption during tank car collisions.

We have not simulated or performed rigorous calculations of jacketed tank cars with metal foam in this project. Simulations or full-scale testing might reveal secondary resisting mechanisms that are not apparent at present.

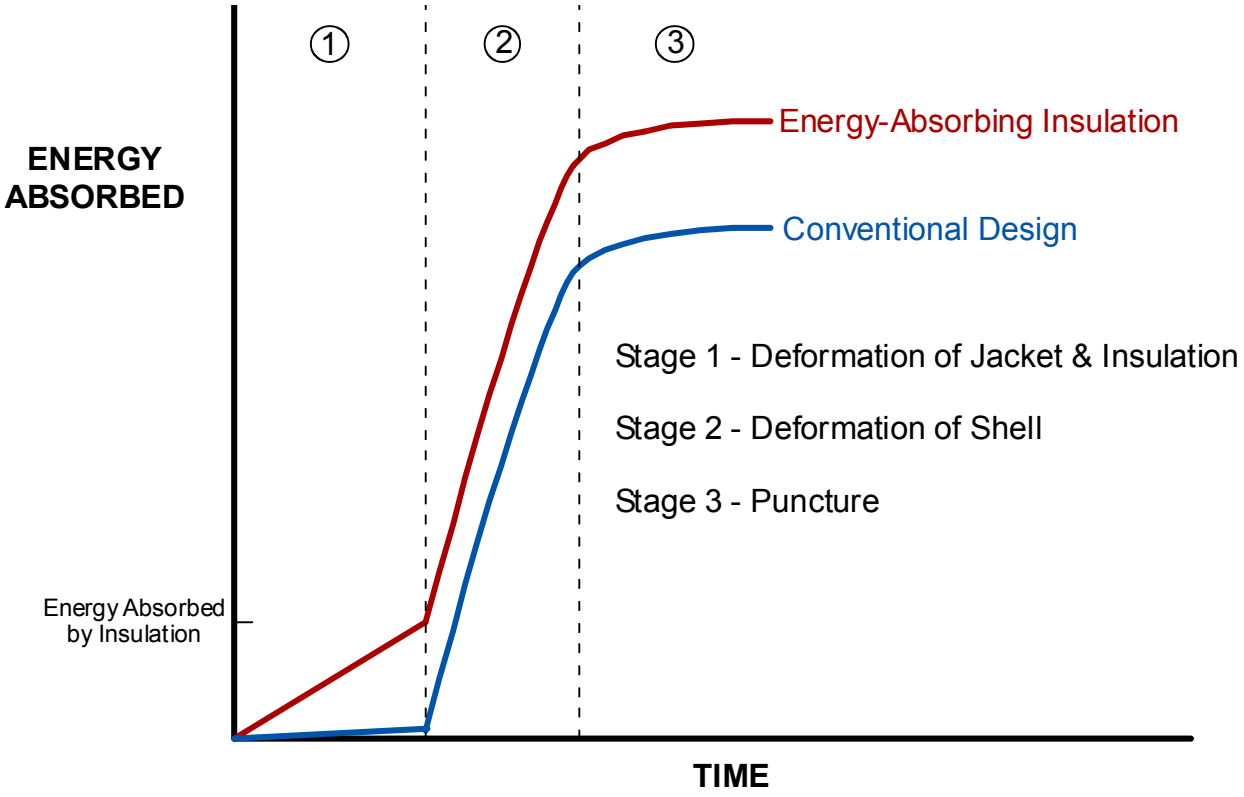

FIGURE 6.3 Effect of an energy-absorbing insulation layer on puncture resistance of a jacketed tank car.

6.3 Developing a Performance Standard

In order to develop a performance standard for new tank car designs, there are two key questions that must be answered:

1. How is performance defined and quantified?
2. What level of performance is "good enough"?

The second question must be addressed by the appropriate regulatory bodies, which may include both Government and private-sector entities. We can, however, recommend suitable approaches for quantifying performance with respect to puncture resistance. Moreover, we can provide estimates of the improvements that can be realized with existing designs combined with advanced steels.

Puncture resistance can be defined in at least three ways:

1. The puncture energy for a given collision scenario.
2. The minimum puncture velocity for a given collision scenario.
3. The probability of lading loss by puncture in an accident.

When comparing various design and/or material alternatives, each of the above criteria will give a different answer as to the relative benefit of a given alternative. For example, if the

performance standard dictates that new tank cars must have twice the puncture resistance of traditional designs made from TC 128 B steel, then the standard must also specify whether this 2-fold improvement is measured by puncture energy, puncture velocity, or lading loss probability.

When a performance standard is based on puncture energy or velocity, the precise collision scenario must also be defined because the energy necessary for puncture is not a fixed quantity for a given tank car. For example, Fig. 5.3 shows that puncture energy is sensitive to the size of the object that strikes the shell or head. When using puncture energy as a performance criterion, it is best to consider *relative* effects. That is, one can determine the relative improvement in puncture energy in a proposed tank car configuration compared to the existing fleet, given the same collision scenario. The implicit assumption of such a comparative exercise is that the same relative improvement in puncture energy will apply to other collision scenarios.

The concept of *puncture intensity* was introduced in the Phase I report [1] and is described in Section 5.2 of the present report. Puncture intensity, *I*, provides a means to normalize an infinite variety of collision scenarios into a single parameter. In Eq. (5.2), *I* is defined as the available kinetic energy in the collision times an unspecified function of other variables. Puncture occurs at a critical puncture intensity, I_R, which characterizes the resistance to puncture of a given tank car. When comparing two tank cars with differing designs and/or materials of construction, the ratio of puncture resistance of the two cars is equal to the ratio of puncture energies because the unknown function on the right-hand side of Eq. (5.2) cancels in the ratio.

The puncture intensity concept makes it possible to relate a specific known and controlled collision scenario (e.g. the Next Generation Project test #2) to the large number of unknown and uncontrolled collision scenarios in the RSI-AAR accident database. Since puncture intensity scales with puncture energy, the exemplar collision event (where the unknown function in Eq. (5.2) is held constant) serves as a surrogate for the population of unknown collision events in past rail accidents. If we assume that past rail accidents are representative of future accidents, then we can predict the probability of lading loss of a proposed tank car if and when it is involved in a rail accident. The procedure for calibrating an exemplar collision scenario to the accident database is described in Section 5.2.

Figure 6.4 illustrates the application of a performance standard based on lading loss probability. A tank car that meets this standard exhibits an increased puncture energy in a given collision event, which translates to a particular lading loss probability. Note that a performance standard based only on puncture energy is of limited value. Unless the standard is connected to lading loss probability, it provides no information about the expected reduction in releases compared to the existing fleet. The performance standard may be expressed in terms of a specific collision scenario. Consider a hypothetical example: “the tank car must survive a 25 mph impact by a bullet car weighing 286,000 lb with a 6-inch x 6-inch chamfered striker.” A proposed modification in design or material of construction could be compared against this standard with computer simulation or full-scale testing. However, any such standard based on a specific scenario should be related to a maximum acceptable lading loss probability.

Table 5.3 illustrates the potential improvement in puncture resistance in chlorine cars that would come from constructing them out of HPS 100. Note that this comparison assumed a 185 ft-lb Charpy energy for HPS 100 and 50 ft-lb for the existing fleet that is made from TC 128B steel.

As we have seen in the Charpy tests performed on modern, low-sulfur heats of TC 128B steel, the toughness can be considerably higher than 50 ft-lb. However, older vintages of TC 128B steel can have upper shelf Charpy values as low as 20-30 ft lb. Thus 50 ft-lb is a reasonable estimate of the aggregate toughness of the existing fleet.

The comparison in Table 5.3 shows a 2- to 3-fold improvement in puncture energy. The corresponding effect on lading loss depends on whether the car is subject to a head impact or shell impact. With the latter, approximately a 60-fold reduction is expected if the chlorine cars are built with the current design and high-toughness steel. For head impacts, only a 6-fold improvement is predicted.

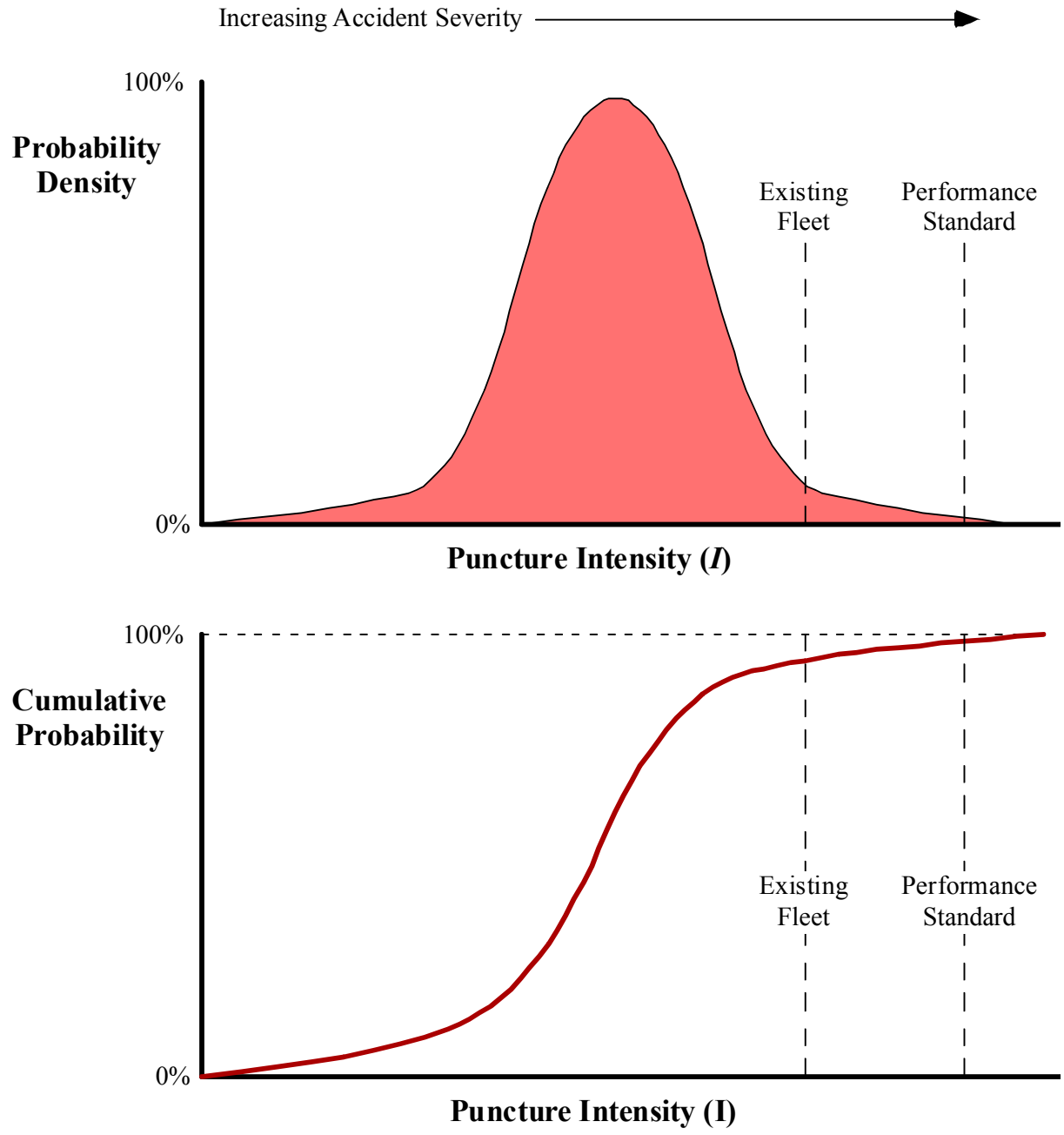

FIGURE 6.4. Relationship between improved puncture energy and reduced lading loss probability.

7 CONCLUSIONS

1. Computational procedures were developed to simulate collision and puncture in tank cars. The methodology was used to quantify the effect of variables such as wall thickness, material toughness, internal pressure and striker size. Over 100 simulations of tank car collision events were performed.

2. The simulations were benchmarked against laboratory experiments and a full-scale test on a retired tank car. The simulation matched the puncture energy of the full-scale test to within a few percent. The simulations of laboratory impact tests largely matched experimental data, but there were some slight discrepancies in a few cases.

3. Further work is necessary to compare the material model used in this study with an alternative model that has been adopted by the Volpe National Transportation Systems Center.

4. The puncture intensity parameter, which was introduced in the Phase I study, provides a means to calibrate the collision simulations to the AAR-RSI accident database, which in turn enables us to predict the effect of design modifications and material substitutions on the probability of lading loss in future rail accidents.

5. The analyses indicated that fabricating chlorine cars with ultra high toughness steels would result in a 2- to 3-fold improvement in puncture energy, assuming the existing design parameters. For shell impacts, this translates to a 60-fold decrease in lading loss probability in an accident. For head impacts, a 6-fold decrease in lading loss probability was predicted.

8 REFERENCES

1. Anderson, T.L. and Kirkpatrick, S.W., "Quantifying and Enhancing Puncture Resistance in Railroad Tank Cars Carrying Hazardous Materials. Phase I: Preliminary Study." Transportation Issues Team, the Chlorine Institute, Arlington, VA, September 2006.

2. Gurson, A.L., "Continuum Theory of Ductile Rupture by Void Nucleation and Growth: Part 1—Yield Criteria and Flow Rules for Porous Ductile Media." *Journal of Engineering Materials and Technology*, Vol. 99, 1977, pp. 2-15.

3. Tvergaard, V., "On Localization in Ductile Materials Containing Spherical Voids." *International Journal of Fracture*, Vol. 18, 1982, pp. 237-252.

4. Tvergaard, V., "Material Failure by Void Growth to Coalescence." *Advances in Applied Mechanics*, Vol. 27, 1990, pp. 83-151.

5. Chu, C.C. and Needleman, A., "Void Nucleation Effects in Biaxially Stretched Sheets." *Journal of Engineering Materials and Technology*, Vol. 102, 1980, pp. 249-256.

6. Faleskog, J., Gao, X., and Shih, C.F., "Cell Model for Nonlinear Fracture Analysis – I. Micromechanics Calibration." International Journal of Fracture, Vol. 89, 1998, pp. 355-373.

7. Treichel, T.T., Hughes, J.P., Barkan, C.P.L., Sims, R.D., Phillips, E.A., and Saat, M.R., "Safety Performance of Tank Cars in Accidents: Probabilities of Lading Loss." Report 05-02, RSI-AAR Railroad Tank Car Safety Research and Test Project, 2006.

8. Bao, Y., Wierzbicki, T., "On Fracture Locus in the Equivalent Strain and Stress Triaxiality Space," *International Journal of Mechanical Sciences,* 2004, pp. 81-98.

9. Yu, H., Jeong, D.Y., Gordon, J.E., and Tang, Y.H., "Analysis of Impact Energy to Fracture Unnotched Charpy Specimens Made from Tank Car Steel." Proceedings of the 2007 ASME Rail Transportation Division Fall Technical Conference, RTDF2007-46038.

10. Tang, Y.H., Yu, H., Gordon, J.E., Priante, M., Jeong, D.Y., Tyrell, D.C., and Pearlman, A.B.., "Analysis of Full-Scale Tank Car Shell Impact Tests." Proceedings of the 2007 ASME Rail Transportation Division Fall Technical Conference, RTDF2007-46010.

9 APPENDICES

9.1 Appendix A – Summary of Literature

When the original Phase II proposal was submitted, the Transportation Issues Team requested that a literature search be added to the work scope. The results of this literature search are summarized below.

Note that this report is *not* a literature *review*, which entails an extensive treatise and critique of relevant published work. Rather, this is a literature *summary*, which catalogs and categorizes the available literature. Brief comments on the ramifications of published work to the Phase II project are provided herein.

A total of 119 references were collected and examined for relevant information. The complete bibliography is provided at the end of this appendix. References were numbered as they were collected, so the ordering has no particular relevance. Each reference was assigned a category that corresponded to the primary focus of the report or article.

9.1.1 Tank Car References

The group of references outlined below pertain specifically to the performance of railroad tank cars. The bulk of the references are reports from private organizations such as AAR and government agencies such as FRA, DOT, and the NTSB.

9.1.1.1 Damage Assessment & Characterization

References: 1, 2, 7, 40, 41, 65

This series of reports and articles discuss the appropriate way to characterize rail car damage following accidents.

9.1.1.2 Experiments and Semi-Empirical Models for Puncture

References: 3, 4, 6, 8, 9, 11, 36, 52, 53, 55

This group of references includes several reports that contain the results of head puncture tests. A semi-empirical model for puncture velocity was developed from these test data. This information will be used as a reality check for the computer models.

9.1.1.3 Risk Assessment

References: 5, 10, 12, 19, 21, 26, 27, 38, 49, 57, 62

These articles and reports address the factors that contribute to risk of release of hazardous cargo from tank cars. This subject matter provides a global perspective on risk, including variables such as human factors, environmental factors, as well as the design of individual tank car components.

9.1.1.4 Computer Modeling

References: 13, 24, 35, 48

Published work on computer modeling of collision and puncture in tank cars is limited. Only a handful of organizations, such as VOLPE, ARA, and HLA, appear to be involved in this type of work.

9.1.1.5 Design and Regulation

References: 14, 17, 18, 20, 34, 37, 67

This group of references includes DOT documents, public testimony, and committee correspondence.

9.1.1.6 Accident Reports

References: 16, 22, 42, 45, 46, 47

This set includes NTSB reports on recent rail accidents, such as Minot and Graniteville.

9.1.1.7 Properties of Tank Car Steels

References: 23, 25, 28, 29, 30, 31, 32, 33, 50, 51, 59, 60, 61

The properties of existing and proposed tank car steels have been extensively studied over the past 30 years. The primary focus has been on improving the resistance to brittle fracture. The upper-shelf toughness, which is related to puncture resistance, has largely been ignored in prior studies on tank car steel.

9.1.2 Relevant Research in Non-Rail Applications

In addition to tank cars, there are other structural applications in which collision, puncture, and fracture are of concern. Examples include marine structures and aerospace structures. A significant amount of research has been performed on constitutive model development and computer simulation.

9.1.2.1 Constitutive Model Development

References, Gurson-Tvergaard and Related Models: 70, 87, 91, 93, 96, 97, 98, 101

References, Other Models: 69, 75, 78, 82, 94, 95, 100, 106, 107

The Gurson-Tvergaard (GT) model is, by far, the most widely referenced model for ductile rupture. It is a physically-based damage model that represents a porous material (i.e., a ductile metal with microvoids) as a smeared continuum. This model was chose for the Phase II simulation work.

A variety of other constitutive models have been published. Most are not suitable for the Phase II work for a variety of reasons:

- Some of the published failure models are highly theoretical and esoteric (e.g., models of fracture at the atomic level), so they are not suitable for computer simulation of full-scale structures.
- Lesser-known models do not have a proven track record and they are not implemented in commercial explicit finite element software such as ABAQUS and LS-DYNA.
- Several articles in the list of references pertain to failure models in composites. While such models may prove useful in the Next Generation project, they are not relevant to the Phase II work.

There are alternatives to the GT model that could have been applied in the Phase II work. However, we did not find a model that has clear advantages over GT. For example, the Johnson-Cook model appears to be the second-most widely referenced approach. Reference 68 describes a modified Johnson-Cook model that accounts for adiabatic heating at very high strain rates. Such an approach is appropriate for ballistic impact modeling. Tank car collisions do not experience sufficiently high strain rates to result in significant adiabatic heating of the steel.[2]

[2] The "bow-tie" specimens tested in the BFCM at Southwest Research Institute did experience significant heating, but videos clearly show that this heating occurred as a result of the striker rubbing on the fracture surface after the specimen failed.

9.1.2.2 Impact/Puncture/Fracture Simulation

References, Gurson-Tvergaard and Related Models: 71, 72, 76, 85, 86, 88, 90, 92, 102, 104, 109, 110, 114

References, Other Models: 68, 73, 74, 77, 79, 80, 81, 83, 84, 89, 99, 103, 103, 108, 112, 113, 115, 116, 117, 118, 119

The bibliography contains a roughly equally-divided number of simulations with the GT model versus other approaches. The most common failure criterion in these simulations, aside from the GT model, is a critical fracture strain or some variation thereof. Critical strain as a failure criterion suffers from two key disadvantages:

- Fracture strain is sensitive to the stress state, particularly the degree of stress triaxiality. Consequently, a failure strain inferred from a tensile test is not applicable to a more complicated load case.
- A strain-based criterion does not enable one to quantify the effect of material toughness on puncture resistance.

As is the case with other failure models that are applied to a simulation involving element deletion, critical fracture strain in a simulation is mesh-dependent. In other words, if the mesh refinement is varied in a series of simulations where an element is deleted when it reaches the assumed fracture strain, the results will change with element size. Simulations that use the GT ductile fracture model are also mesh dependent, so it important to calibrate the model to the particular mesh that is used for the analysis.

NASA has studied puncture resistance of the outer skin of the International Space Station to ensure that it can withstand collisions by small debris. However, they use a fracture mechanics model to quantify puncture resistance. This approach is not suitable for the Phase II work. A fracture mechanics-based failure model assumes propagation from a pre-existing crack. The predictions are highly sensitive to the assumed initial crack size. Puncture normally involves the creation of an opening in the absence of a significant pre-existing flaw.

9.1.3 Conclusions

While the GT model is not universally used to characterize and predict ductile rupture in metals, there is certainly a consensus behind this model. It has the advantage of being physically based, so there is a high likelihood that laboratory data can be reliably transferred to structural applications using the GT material model.

There is ample precedent in the published literature for using the GT model in dynamic simulations of puncture and rupture. Some of the common alternative criteria, such as critical failure strain, are over-simplified and do not recognize the inherent mesh dependence of simulations that involve element deletion.

9.1.4 Bibliography

1. Pieratt, K. Scott, Jeffrey C. Davis, and Peter Conlon, "Damage Assessment of Railroad Tank Cars Involved in Accidents: Phase I Literature Search and Evaluation", DOT/FRA/ORD-06/12 (December 2005)

2. Kloop, Richard W., Steven W. Kirkpatrick, and Donald A. Shockey, "Damage Assessment of Railroad Tank Cars Involved in Accidents: Phase II Modeling and Validation", DOT/FRA/ORD-02/04 (December 2002)

3. Jeong, D.Y., Y.H. Tang, A.B. Pearlman, "Evaluation of Semi-Empirical Analyses for Railroad Tank Car Puncture Velocity, Part I: Correlations with Experimental Data", DOT/FRA/ORD-01/21.1 (November 2001)

4. Jeong, D.Y., Y.H. Tang, A.B. Pearlman, "Evaluation of Semi-Empirical Analyses for Railroad Tank Car Puncture Velocity, Part II: Correlations with Engineering Analysis", November 2001, DOT/FRA/ORD-01/21.1

5. Raj, Phani K., Clayton K. Turner, "Hazardous Material Transportation in Tank Cars: Analysis of Risks", FRA/ORD-92/34 (15 May 1993)

6. Coltman, Michael, Morrin E. Hazel Jr., "Chlorine Tank Car Puncture Resistance Evaluation", DOT/FRA/ORD-92/11 (July 1992)

7. Reuter, W.G., J.D. Mudlin, B.L. Harris, et al, "Evaluation of Damaged Tank Car Structural Integrity", DOT/FRA/ORD-88/02 (January 1988)

8. Larson, William G., "Aluminum/Cold Temperature Tank Car Puncture Resistance Tests: Data Report", DOT/FRA/ORD-92/29 (August 1992)

9. Lishaa, M.A., C.C. Dai, M. Giltrud, J.C.S. Yang, "Puncture Resistance of Scale Model Aluminum Tank Car Heads", DOT/FRA/ORD-87/06 (June 1987)

10. Hagopian, John H., "Event Probabilities and Impact Zones For Hazardous Materials Accidents On Railroads", DOT/FRA/ORD-83/20 (November 1983)

11. Peters, D.A., B.A. Szabo, W.B. Diboll, "Tank Car Head Puncture Mechanisms", FRA-OR-76/269 (April 1980)

12. Adams, D.E., W.A. Bullerdiek, J.S. Patten, F.A. Vassallo, "Rail Hazardous Material Tank Car Design Study", FRA/ORD-75/45 (April 1975)

13. Hohenemser, K.H., W.B. Diboll, S.K. Yin, B.A. Szabo, "Computer Simulation of Tank Car Head Puncture Mechanisms Classification Yard Accidents", FRA-ORD&D-75-23 (February 1975)

14. 49 CFR Part 171, et al., "Crashworthiness Protection Requirements for Tank Cars; Detection and Repair of Cracks, Pits, Corrosion, Lining Flaws, Thermal Protection Flaws and Other Defects of Tank Car Tank; Final Rule", Federal Register (21 September 1995)

15. Mok, G.C., L.E. Fischer, S.S. Murty, M.C. Witte, "Shipping Container Response to Three Severe Railway Accident Scenarios", 1998 Joint Pressure Vessels and Piping Conference, San Diego, CA, ASME (April 1998)

16. National Transportation Safety Board, "Collision of Union Pacific Railroad Train MHOTU-23 With BNSF Railway Company Train MEAP-TUL-126-D With Subsequent Derailment and Hazardous Materials Release Macdona, Texas June 28, 2004", NTSB/RAR-06/03 (6 July 2006)

17. Barkan, Christopher P.L., Satis V. Ukkusuri, S. Travis Waller, "Optimizing the design of railway tank cars to minimize accident-caused releases", Computers & Operations Research, (2005 Elsevier Ltd)

18. Saat, Mohd Rapik, Christopher P.L. Barkan, "Release Risk and Optimization of Railroad Tank Car Safety Design", Transportation Research Record: Journal of the Transportation Research Board (2005)

19. Saat, Mohd Rapik, Christopher P.L. Barkan, "Release Risk as Metric for Evaluating Tank Car Safety Performance", Saat & Barkan 05-1826

20. Boardman, Joseph H., "Written Statement of Joseph H. Boardman, Administrator, Federal Railroad Administration, U.S. Department of Transportation, before the Subcommittee on Railroads, Committee on Transportation and Infrastructure, U.S. House of Representatives" (13 June 2006)

21. Saat, Mohd Rapik, Christopher P.L. Barkan, "The Effect of Rerouting and Tank Car Safety Design on the Risk of Rail Transport of Hazardous Materials", Railroad Engineering Program Abstract

22. Hersman, Deborah A.P., "Tank Car Safety", The Chlorine Institute, Inc. 2006 Fall Meeting (25 September 2006)

23. "Evaluation of New Steels For Tank Cars", Report RA-03-7-53, Railroad Tank Car Safety Research and Test Project, (29 April 1997)

24. Anderson, Ted L., Steven W. Kirkpatrick, "Quantifying and Enhancing Puncture Resistance in Railroad Tank Cars Carrying Hazardous Material Phase I: Preliminary Study", (5 July 2006)

25. Hicho, George E., Donald E. Harne, "Mechanical Properties and Fracture Toughness of AAR TC128 Grade B Steel in the Normalized, and Normalized and Stress Relieved Conditions", NISTIR 4660 Report No. 24

26. Treichel, T.T., J.P. Hughes, C.P.L. Barkan, et al, "Safety Performance of Tank Cars in Accidents: Probabilities of Lading Loss", Railroad Supply Institute, (January 2006)

27. Treichel, T.T., "Supplemental Information on the Accident History of Chlorine Tank Cars, 500 psi Tank Cars, and 600 psi Tank Cars Through 2003", Railroad Supply Institute, (February 2006)

28. "Phase 03 Data Display Report on Results of Tests on Mill Plate Samples and Samples Removed From Tank Car Involved in Accidents", Railroad Tank Car Safety Research and Test Project , RA-03-3-13 (19 April 1972)

29. "Evaluation of New Steels For Tank Cars Phase II", Railroad Tank Car Safety Research and Test Project, RA-03-9-59, (2 May 1991)

30. Hughes, J.P., C.F. Heuer, T.L. Anderson, "Fracture Behavior of Tank Car Steels in Accidents From 1981 Through 1994", RA-03-6-62 (December 1998)

31. Sims, Roger D., Joseph P. Hughes, "Steels for Tank Cars", Sims Professional Engineers

32. Eiber, R.J., L.L. Olson, "Final Phase 03 Report Material Study On Steels Used In Current And Former Tank Car Construction And From Cars Involved In Accidents", RA-03-5-33 (21 August 1975)

33. Pellini, W.S., R.J. Eiber, L.L. Olson, "Phase 03 Report On Fracture Properties Of Tank Car Steels: Characterization And Analysis", RA-03-4-32 (20 August 1975)

34. Reiner, Frank, "The Chlorine Institute statement of Frank Reiner"

35. Kirkpatrick, S.W., R.W. Klopp, "Hazard Assessment for Pressure Tank Cars Involved in Accidents"

36. Jeong, D.Y., Y.H. Tang, et al, "Engineering Analyses for Railroad Tank Car Head Puncture Resistance", IMECE2006-13212, Proceedings of IMECE2006 (November 2006)

37. "Next Generation Rail Tank Car" Stakeholder Engagement Presentation #1 (Fall 2006)

38. Raj, Phani K., "Hazardous Materials Transportation in Tank Cars: Analysis of Risks - Part II", FRA/ORD-95/03 (31 December 1994)

39. "Railway Investigation Report Number R05H0011" Ottawa Central Railway (2 May 2005)

40. Gipson, G.S., B.W. Yeigh, "Scaling Issues Related to Modeling of Railroad Car Damage I - Derailment, Plastic Deformation, Rupture, and Impact", Mathematical and Computer Modeling (August 2005)

41. Gipson, G.S., B.W. Yeigh, "Scaling Issues Related to Modeling of Railroad Car Damage II - Explosions, Fires, and Safety Valves", Mathematical and Computer Modeling , (August 2005)

42. National Transportation Safety Board Notation 7710A, Railroad Accident Report, "Collision of Norfolk Southern Freight Train 192 with Standing Norfolk Southern Local Train P22 with Subsequent Hazardous Materials Release at Graniteville, South Carolina", (January 6, 2005)

43. Boardman, Joseph H. , "National Transportation Safety Board Safety Recommendation", (July 20, 2006)

44. Boardman, Joseph, H., "U.S. Department of Transportation, before the Subcommittee on Railroads, Committee on Transportation and Infrastructure, U.S. House of Representatives", (June 13, 2006)

45. National Transportation and Safety Board, "Derailment of Canadian Pacific Railway Freight Train 292-16 and Subsequent Release of Anhydrous Ammonia Near Minot, North Dakota", Railroad Accident Report, NTSB/RAR-04/01, PB2004-916301 Notation 7461A (January 18, 2002)

46. Watson, David E., Kendall R. Tarter, James Johnson, "National Transportation Safety Board, Derailment with Hazardous Material Released Canadian Pacific Railway Minot, North Dakota, DCA-02-MR-002 Factual Report" (January 18, 2002)

47. National Transportation Safety Board, "Materials Laboratory Factual Report, Report No. 02-58" (January 18, 2002)

48. Dalrymple, Thomas, Steven W. Stahl, H. Keith Hunt, "Puncture Resistance of Non-Pressure Tank Cars, An Analytical Approach to Develop Equivalent Puncture Resistance for 286K GRL Tank Cars, HLA Engineering Report No. 99320-0", (June 2000)

49. Treichel, T.T., J.P. Hughes, C.P. Barkan , et al, "Safety Performance of Tank Cars In Accidents: Probabilities of Lading Loss", (January 2006)

50. Eiber, R. J., L.L. Olson, "Final Phase 03 Report Material Study on Steel Used in Current and Former Tank Car Construction and from Cars Involved in Accidents", (August 21, 1975)

51. Oppenheimer, R. B., Berry Harris Jr., A.L., et al, "Phase 03 Report on Fracture Properties of Tank Car Steels Characterization and Analysis", (August 20, 1975)

52. Belport, Steven M., "Evaluation of the Puncture Resistance for Stainless Steel and Carbon Steel Tank Heads P-39-114", (June 1993)

53. Oppenheimer, R. B., Berry Harris Jr., A.L., et al, "RA-05-1-17, "Final Phase 05 Report on Tank Car Head Study", (July 14, 1972)

54. Coyl, C.E., "RA-05-2-29 Phase 05 Report on June 9, 1974 Accident Involving Head Shields" (August, 28, 1974)

55. Brinkerhoff, J.D., W. J. Harris, C.E. Coyl, et al, "Report RA-05-3-35 (AAR R-197) Phase 05 Report on Head Shield Fatigue Tests", (November 10, 1975)

56. Coltman, Michael, Morrin E. Hazel Jr., “Chlorine Tank Car Puncture Resistance Evaluation” (July 1992)

57. Unger, J. J., G.H. Way Jr., S.H. Bonster, “Report RA-09-7-60 (AAR R) Bottom Discontinuity Protection Effectiveness on DOT 111A Stub Sill Tank Cars” (June 9, 1992)

58. Krick, K.A., G.H. Way Jr., S. H. Bosner, et al “Analysis of Aluminum Tank Cars Damaged in Accidents 1965 through 1986 Documentation Report RA-20-1-57-AAR R-749”, (March 5, 1990)

59. Steele, Roger K., “Steel Alloys with Lower Bainite Microstructures for Use in Railroad Cars and Track”, (January 2002)

60. Pellini, William S., “AAR-RPI Project for Analytical Selection of New Tank Car Steels of Improved Weldability and Fracture Properties”, (May 1985)

61. Pellini, William S., “Feasibility Analysis for Tank Car Applications of New Micro-. lloyed and Controlled Rolled Steels – Description of Fracture Properties and Comparisons with Steel in Present Use, Report No. R-543”, (April 1983)

62. Kruizenga, J.R., W.J. Harris Jr., C.E. Coyl, “Report on Effectiveness of Shelf Couplers, Head Shields and Thermal Shields”, (May 15, 1981)

63. Gustafsen, B.A., W.J. Harris Jr., C.E. Coyl, et al, “Supplement to Report RA-02-3-44 (AAR R-482) Phase 02 Report on Effectiveness of Shelf Couplers, Head Shields and Thermal Shields”, (August 20, 1981)

64. Bonser, S. H., W.J. Harris Jr., A.F. Barber, et al, “Report RA-02-5-51 (AAR R-610) Effectiveness of Shelf Couplers, Head Shields and Thermal Shields on DOT 112 (114) and 105 Tank Cars”, (June 13, 1985)

65. McCarthy, J.F., G.H. Way Jr., S.H. Bonser, et al “Report RA-02-6-55 (AAR R-709) Analysis of Tank Cars Damaged in Accidents 1965 through 1986 Documentation Report”, (January 30, 1989)

66. Heuer, C.F., W.R. Warke, T.L. Anderson, “Metallurgy, Properties and Commercial Availability of Micro-Alloyed Plate Steels Report RA-03-6-63 (AAR R-938)”, (October 2000)

67. Bonser, S. H., G.H. Way Jr., P.H. Croft, et al, “Report RA-03-8-54 (AAR R-668) Tank Car Design Basis – Yield vs. Tensile”, (October 22, 1987)

68. Borvik, T., O.S. Hopperstad, T. Berstad, et al, “A Computational Model of Viscoplasticity and Ductile Damage for Impact and Penetration”, (April 2001)

69. Rashid, K., Abu Al-Rub, George Z. Voyiadjis, “Finite Strain Plastic-damage Model for High Velocity Impact using Combined Viscosity and Gradient Localization Limiters: Part I Theoretical Formulation”, (October 2006)

70. Chen, Jian, Huang Yuan, "A Micro-Mechanical Damage Model Based on Gradient Plasticity: Algorithms and Applications", (2002)

71. Bronkhorst, C.A., E.K. Cerreta, Q. Xue, et al, "An Experimental and Numerical Study of Localization Behavior of Tantalum and Stainless Steel" (2006)

72. Chen, Yu, Steve Lambert, "Analysis of Ductile Tearing of Pipeline-Steel in Single Edge Notch Tension Specimens" (2003)

73. Pedro, M.A. Areias, Ted Belytschko, "Analysis of Finite Strain Anisotropic Elastoplastic Fracture in Thin Plates and Shells" (October 2006)

74. Baaser, H., D. Gross, "Analysis of Void Growth in a Ductile Material in Front of a Crack Tip", (2002)

75. Harstad,E. N., P.J. Maudlin, J.B. McKirgan, "Anisotropic Failure Modeling for HY-100 Steel", (2002)

76. Tsuta, Toshio, Yajum Yin, Takeshi I Wamoto, "Micro Damage Evolution Analysis of Target Impacted by Projectile", (2003)

77. . Mullin, Scott A., Herve Couque, Burtron G. Cour-Palais, et al, "Bursting of Shielded Pressure Vessels Subject to Hypervelocity Impact", (1997)

78. Garion, Cedric, Blazej Skoczen, "Combined Model of Strain-induced Phase Transformation and Orthotropic Damage in Ductile Materials at Cryogenic Temperatures", (October 2003)

79. Naar, Hendrik, Pentti Simonsen Kujala, Cerup Bo, et al, "Comparison of Crashworthiness of Various Bottom and Side Structures", (April 2001)

80. Grujicic, M., B. Pandurangan, K. L. Koudela, et al, "A Computational Analysis of the Ballistic Performance of Light-Weight Hybrid Composite Armors", (January 2006)

81. Biner, S.B., "Ductile of Bulk Metallic Glasses and their Composite with Ductile Reinforcements: A Numerical Study", (August 2005)

82. Kuroda, M., A. Uenishi, H. Yoshida, et al,, "Ductility of Interstitial-Free Steel Under High Strain Rate Tension: Experiments and Macroscopic Modeling with Physcially-based Consideration", (August 2005)

83. Dally, J.W., "Dynamic Failure Mechanics of Modern Materials – A Summary of the First Discussion Session", (1995)

84. Ben-Dor, G., A. Dubinsky, T. Elperin, "Effect of Air Gaps on Ballistic Resistance of Targets for Conical Impactors", (1998)

85. Kwon, Y.W., P.M. McDermott, "Effects of Void Growth and Nucleation on Plastic Deformation of Plates with Fluid-Structure Interaction", (2001)

86. Dutta, B.K., M.K. Sahu, M.K. Samal, et al, "Evaluation of Materials Jr and Fracture Toughness Transition Curves using Micro-Mechanical Modeling", (2004)

87. Pardoen, T., J.W. Hutchinson, "An Extended Model for Void Growth and Coalescence", (2000)

88. Skallerud B., Z.L. Zhang, "Finite Element Modeling of Cracked Inelastic Shells with Large Deflections: Two-dimensional and Three-dimensional Approaches", (August 1999)

89. Tsai, J.H., A. Patra, R. Wetherhold, "Finite Element Simulation of Shaped Ductile Fiber Pullout Using a Mixed Cohesive Zone/Friction Interface Model", (March 2004)

90. Lassance, D., F. Scheyvaerts, T. Pardoen, "Growth and Coalescence of Penny-Shaped Voids in Metallic Alloys", (February 2006)

91. Corigliano, Alberto, Stephano Mariani, et al, "Identification of Gurson – Tvergaard Material Model Parameters via Kalman Filtering Technique. I. Theory", (2000)

92. Cerup Simonsen, Bo, Shaofan Li , " Mesh-Free Simulation of Ductile Fracture", (2004)

93. Mariani, Stafano, Alberto Corigliano, "Anisotrpic Behavior of Porous, Dictile Media", (April 2000)

94. Garion, C., B. Skoczen, "Anisotropic Constitutive Model of Strain-Induced Phenomena in Stainless Steels at Crygenic Temperatures", (2004)

95. Mir, A.A., D.C. Barton, T.D. Andrews, et al, "Anisotropic Ductile Failure in Free Machining Steel at Quasi-Static and High Strain Rates", (2005)

96. Pardoen, T., J.W. Hutchinson, "Micromechanics-Based Model for Trends in Toughness of Ductile Metals", (2003)

97. Chen, Bin, Xiang-He Penge, Jing-Hong Fan, et al, "Microscopically Based New Damage Constitutive Model with Applications", (2000)

98. Khoo, H.A., T.M. Hrudey, J.J.R. Cheng, “Microvoid Damage Model with Material Dilation for Ductile Fracture”, October 2006)

99. Dabboussi, W., J.A. Nemes, “Modelling of Ductile Fracture Using the Dynamic Punch Test”, (2005)

100. Hao, Su, Wing Kam Liu, Brian Moran, et al, “Multi-scale Constitutive Model and Computational Framework for the Design of Ultra-High Strength, High Toughness Steels”, (December 2003)

101. Jackiewicz, J., “Numerical Formulations for Nonlocal Plasticity Problems Coupled to Damage in the Polycrystalline Microstructure”, (February 2006)

102. Chen, Yu, Steve Lambert, “Numerical Modeling of Ductile Tearing for Semi-Elliptical Surface Cracks in Wide Plates”, (September 2004)

103. Brooker, Daniel C., “Numerical Modeling of Pipeline Puncture Under Excavator Loading. Part I. Development and Validation of a Finite Element Material Failure Model for Puncture Simulation”, (August 2003)

104. Pardoen, T.,“Numerical Simulation of Low Stress Triaxiality Ductile Fracture”, (July 2006)

105. Borvik,T., O.S. Hopperstad, T. Berstad, et al, “Perforation of 12mm Thick Steel Plates by 20mm Diameter Projectiles with Flat, Hemispherical and Conical Noses Part II: Numerical Simulations”, (June 2001)

106. Garion, C., B.T. Skoczen,“Plastic Strain Induced Damage Evolution and Martensitic Transformation in Ductile Materials Cryogenic Temperatures”, (2002)

107. Yin, Yajum, Qinshan Fan, Bo Wang, “Preliminary Examination of the Modified Lower-Bound Meso-Damage Consatitutive Model for Porous Materials”, (2000)

108. Liang, Cho-Chung , Ming-FangYang, Pin-Wen Wu, et al, “Resistant Performance of Perforation of Multi-Layered Targets Using an Estimation Procedure with Marine Application”, (November 2004)

109. Becker, R., "Ring Fragmentation Predictions Using the Gurson Model with Material Stability Conditions as Failure Criteria", (October 2001)

1. 110. Gullerud, Anre S., Xiaosheng Gao, Robert H. Dodds Jr., R. Haj-Ali, "Simulation of Ductile Crack Growth Using Computational Cells: Numerical Aspects", (December 1999)

111. Dikshit, S. H., V.V. Kutumabarao, G. Sundararajan, "The Influence of Plate Hardness on the Ballistic Penetration of Thick Steel Plates", (1995)

112. Walters, William P., Cyrill L. Williams, "The Influence of Armor Material Parameters on the Penetration by Long-Rod Projectiles", (July 2006)

113. Logan, Roger W., Frank J. Tokarz, "Overview of Crash and Impact Analysis at Lawrence Livermore National Laboratory", (1993)

114. Kamel, A. K., M.J. Worswick, D. Nandlall, "Effect of Nonlocal Damage Treatment on Dynamic Fracture Predictions", (1998)

115. De Rosset, William S.,"Role of the Computer in Examining Structures Under Extreme Loading Conditions", (1997)

116. Schafer, Frank K. Schneider, Eberhard E., Lambert, Michal, "Hypervelocity Impacts on Cylindrical Pressure Vessels – Experimental Results and Damage Classification" (1997)

117. Munz, Thomas W., Rix, Karsten S., William, Kaspar J., "Computational Simulation of Dynamic Impact Problems" (1996)

118. Zukas , J.A., and Gaskill, B., "Impact Effects in Thin-Walled Structures" (1996)

119. Trinh, Khanh V., Revelli,Vera D., Diegert, Kathleen D., "Dynamic Penetration Resistance of Think Metallic Shells", (1995)

9.2 Appendix B – Tabulated Results for Tank Car Simulations.

tank car model	FEM #	config		material props		friction	mesh size	pressure	lading	striker			absorbed energy		equiv velocity	
		shell only / jacketed / shield	impact	material	charpy value					size	initial velocity	weight if ≠ 280k	final	at leak	final	at leak
					ft-lb		mm	psi		in.	mph	kip	kip*ft	kip*ft	mph	mph
100W	6	shell only	broadside	TC128-B	50		5.0	55.0	none	6	40.0		223	211	4.9	4.7
100W	7	jacketed	broadside	TC128-B	50		5.0	55.0	none	6	40.0		312	300	5.8	5.7
100W	8	shell only	head	TC128-B	50		5.0	55.0	none	6	40.0		187	185	4.5	4.4
100W	10	jacketed	head	TC128-B	50		5.0	55.0	none	6	40.0		354	347	6.2	6.1
100W	11	jacket+shield	head	TC128-B	50		5.0	55.0	none	6	40.0		619	609	8.1	8.1
100W	12	shell only	broadside	HPS-100	185		5.0	55.0	none	6	40.0		575	543	7.8	7.6
100W	13	shield	head	TC128-B	50		5.0	55.0	none	6	40.0		647	636	8.3	8.2
300W	10	shell only	broadside	TC128-B	112		2.5	300.0	none	6	40.0		302	297	5.7	5.6
300W	11	shell only	broadside	TC128-B	112		2.5	150.0	none	6	40.0		409	400	6.6	6.5
300W	12	shell only	broadside	TC128-B	86		2.5	71.4	none	6	40.0		505	481	7.3	7.2
300W	15	shell only	head	TC128-B	86		2.5	71.4	none	6	40.0		441	429	6.9	6.8
300W	16	shell only	broadside	TC128-B	86		2.5	71.4	none	6	30.0		552	536	7.7	7.6
300W	17	shell only	broadside	TC128-B	86		2.5	71.4	none	6	20.0		545	537	7.6	7.6
300W	18	jacketed	broadside	TC128-B	91		5.0	71.4	none	6	40.0		611	579	8.1	7.9
300W	20	shell only	broadside	TC128-B	50		5.0	71.4	none	6	40.0		292	279	5.6	5.5
300W	21	jacketed	broadside	TC128-B	50		5.0	71.4	none	6	40.0		367	352	6.3	6.1
300W	22	shell only	head	TC128-B	50		5.0	71.4	none	6	40.0		248	247	5.1	5.1
300W	24	jacketed	head	TC128-B	50		5.0	71.4	none	6	40.0		356	345	6.2	6.1
300W	25	jacket+shield	head	TC128-B	50		5.0	71.4	none	6	40.0		647	635	8.3	8.2
300W	26	shell only	broadside	HPS-100	185		5.0	71.4	none	6	40.0		894	823	9.8	9.4
300W	27	shield	head	TC128-B	50		5.0	71.4	none	6	40.0		671	653	8.5	8.4
300W	28	shell only	broadside	TC128-B	86		2.5	71.4	none	6	40.0		636		8.2	
300W	29	shell only	broadside	TC128-B	86		2.5	71.4	none	6	30.0		781		9.1	
300W	30	shell only	broadside	TC128-B	86		2.5	71.4	none	6	20.0		896		9.8	
300W	31	shell only	broadside	TC128-B	86		2.5	71.4	none	6	40.0		402		6.6	
300W	32	shell only	broadside	TC128-B	86		2.5	71.4	none	6	30.0		530		7.5	
300W	33	shell only	broadside	TC128-B	86		2.5	71.4	none	6	20.0		796		9.2	

tank car model	FEM #	config		material props		friction	mesh size	pressure	lading	striker			absorbed energy		equiv velocity	
		shell only / jacketed / shield	impact	material	charpy value					size	initial velocity	weight if ≠ 280k	final	at leak	final	at leak
					ft-lb		mm	psi		in.	mph	kip	kip*ft	kip*ft	mph	mph
500W	17	shell only	broadside	TC128-B	112		2.5	250.0	none	6	40.0		603	595	8.0	8.0
500W	18	shell only	broadside	TC128-B	112		2.5	125.0	none	6	40.0		898	898	9.8	9.8
500W	19	shell only	broadside	TC128-B	112		2.5	62.5	none	6	40.0		1,300	1,300	11.8	11.8
500W	20	shell only	broadside	TC128-B	112		2.5	31.3	none	6	40.0		2,084	2,011	14.9	14.7
500W	21	shell only	broadside	TC128-B	112		2.5	0.0	none	6	40.0		2,436	2,436	16.1	16.1
500W	22	shell only	broadside	TC128-B	86		2.5	115.2	none	6	40.0		793	754	9.2	9.0
500W	23	shell only	head	TC128-B	86		2.5	115.2	none	6	40.0		614	603	8.1	8.0
500W	24	shell only	head	TC128-B	86		2.5	500.0	none	6	40.0		334	326	6.0	5.9
500W	25	shell only	head	TC128-B	86		2.5	250.0	none	6	40.0		443	430	6.9	6.8
500W	26	shell only	head	TC128-B	86		2.5	88.7	none	6	40.0		671	658	8.5	8.4
500W	27	shell only	head	TC128-B	86		2.5	31.3	none	6	40.0		822	799	9.4	9.2
500W	28	shell only	head	TC128-B	86		2.5	0.0	none	6	40.0		1,044	994	10.6	10.3
500W	29	shell only	broadside	TC128-B	114		5.0	88.7	none	6	40.0		795	765	9.2	9.0
500W	30	shell only	broadside	TC128-B	76		5.0	115.2	none	6	40.0		603	583	8.0	7.9
500W	31	shell only	broadside	TC128-B	93		5.0	115.2	none	6	40.0		800	784	9.3	9.2
500W	32	shell only	broadside	TC128-B	96		5.0	115.2	none	6	40.0		860	834	9.6	9.4
500W	33	shell only	broadside	TC128-B	86		5.0	115.2	none	6	40.0		747	719	8.9	8.8
500W	34	shell only	broadside	TC128-B	126		5.0	125.0	none	6	40.0		1,076	1,052	10.7	10.6
500W	35	shell only	broadside	TC128-B	118		5.0	125.0	none	6	40.0		1,035	991	10.5	10.3
500W	36	shell only	broadside	TC128-B	92		5.0	115.2	none	6	40.0		673	647	8.5	8.3
500W	37	shell only	broadside	TC128-B	92		5.0	115.2	none	12	40.0		2,187	2,029	15.3	14.7
500W	38	jacketed	broadside	TC128-B	92		5.0	115.2	none	6	40.0		937	920	10.0	9.9
500W	40	shell only	broadside	TC128-B	92		5.0	115.2	none	15	40.0		3,214	2,837	18.5	17.4
500W	41	shell only	broadside	TC128-B	96	0.5	5.0	115.2	none	6	40.0		1,097	1,047	10.8	10.6
500W	42	shell only	broadside	TC128-B	50		5.0	115.2	none	6	40.0		422	408	6.7	6.6
500W	43	jacketed	broadside	TC128-B	50		5.0	115.2	none	6	40.0		484	467	7.2	7.1
500W	44	shell only	head	TC128-B	50		5.0	115.2	none	6	40.0		373	371	6.3	6.3

tank car model	FEM #	config		material props		friction	mesh size	pressure	lading	striker			absorbed energy		equiv velocity	
		shell only / jacketed / shield	impact	material	charpy value					size	initial velocity	weight if ≠ 280k	final	at leak	final	at leak
					ft-lb		mm	psi		in.	mph	kip	kip*ft	kip*ft	mph	mph
500W	44	shell only	head	TC128-B	50		5.0	115.2	none	6	40.0		373	371	6.3	6.3
500W	46	jacketed	head	TC128-B	50		5.0	115.2	none	6	40.0		503	488	7.3	7.2
500W	47	jacket+shield	head	TC128-B	50		5.0	115.2	none	6	40.0		696	694	8.6	8.6
500W	48	shell only	broadside	HPS-100	185		5.0	115.2	none	6	40.0		1,197	1,185	11.3	11.3
500W	49	jacketed	broadside	HPS-100	185		5.0	115.2	none	6	40.0		1,305	1,246	11.8	11.5
500W	50	jacketed	head	HPS-100	185		5.0	115.2	none	6	40.0		1,009	970	10.4	10.2
500W	51	shell only	head	HPS-100	185		5.0	115.2	none	6	40.0		691	689	8.6	8.6
500W	54	jacket+shield	head	HPS-100	185		5.0	115.2	none	6	40.0		1,478	1,435	12.6	12.4
500W	55	jacket+shield	head	HPS-100 / TC128-B	185		5.0	115.2	none	6	40.0		917	915	9.9	9.9
500W	56	shell only	broadside	TC128-B	50		5.0	115.2	chlorine	6	40.0		354	325	6.2	5.9
500W	57	shield	head	TC128-B	50		5.0	115.2	none	6	40.0		733	729	8.9	8.8
500W	58	jacketed	broadside	TC128-B	50	0.1	5.0	100.0	water	6	15.1	286	1,151	1,122	11.0	10.8
500W	59	shield	head	HPS-100	185		5.0	115.2	none	6	40.0		1,595	1,564	13.1	12.9
500W	60	shell only	broadside	TC128-B	96	0.1	5.0	115.2	none	6	40.0		909	870	9.9	9.6
500W	61	shell only	broadside	TC128-B	96	0.2	5.0	115.2	none	6	40.0		991	953	10.3	10.1
500W	64	jacketed	broadside	TC128-B	50	0.1	5.0	100.0	chlorine	6	15.1	286	495	478	7.2	7.1
500W	65	jacketed	broadside	TC128-B	50	0.1	5.0	100.0	chlorine	6	40.0	286	397		6.4	
500W	67	jacketed	broadside	TC128-B	50	0.1	5.0	100.0	chlorine	6	15.1	286	477	437	7.1	6.8
500W	68	jacketed	broadside	TC128-B	106	0.1	5.0	100.0	chlorine	6	15.1	286	1,066	1,035	10.6	10.4
500W	69	jacketed	broadside	TC128-B	106	0.1	5.0	100.0	chlorine	6	40.0	286	767	1	9.1	0.4
600W	3	shell only	broadside	TC128-B	86		2.5	137.9	none	6	40.0		1,028	988	10.5	10.3
600W	5	jacketed	broadside	TC128-B	91		5.0	137.9	none	6	40.0		985	944	10.3	10.0
600W	6	shell only	broadside	TC128-B	50		5.0	137.9	none	6	40.0		573	562	7.8	7.8
600W	7	jacketed	broadside	TC128-B	50		5.0	137.9	none	6	40.0		637	612	8.3	8.1
600W	8	shell only	head	TC128-B	50		5.0	137.9	none	6	40.0		536	505	7.6	7.3
600W	10	jacketed	head	TC128-B	50		5.0	137.9	none	6	40.0		720	700	8.8	8.6
600W	11	jacket+shield	head	TC128-B	50		5.0	137.9	none	6	40.0		914	900	9.9	9.8
600W	12	shield	head	TC128-B	50		5.0	137.9	none	6	40.0		882	866	9.7	9.6
600W	13	shell only	broadside	HPS-100	185		5.0	137.9	none	6	40.0		1,394	1,366	12.2	12.1

Simulations resembling Next Generation Project Test #2 are marked yellow.